A modified oncolytic measles virus exhibits strong immunotherapeutic potential through RIG-I activation by defective viral genomes

Aleksandr Barinov[1,2], Heidy Vera-Peralta[1,2], Joëlle S Nader[3], Valérie Najburg[2], Chantal Combredet[2], Atousa Arbabian[1,2], Ségolène Gracias[1], Phanramphoei N Frantz[1,2], Roseline Vibert[2], Eddy Simard[2], Marie Coateval[1], Daniel Pouliquen[3], Tacien Petithomme[3], Matthieu Prot[4], Etienne Simon-Lorière[4], David Hardy[5], Sarra Loulizi[5], Bernadette Brzezicha[6], Jens Hoffmann[6], Véronique Riebbels[1], Jean-François Le Bigot[1], Marc Grégoire[3], Jean-François Fonteneau[3], Anastassia V. Komarova[2,7], Nicolas Boisgerault[3]*, Frédéric Tangy[1,2*¥]

[1]Oncovita, Paris, France

[2]Institut Pasteur, Université Paris Cité, Pasteur-Oncovita Joint Laboratory, Paris, France

[3]Nantes Université, Inserm UMR 1307, CNRS UMR 6075, Université d'Angers, CRCI2NA, F-44000 Nantes, France

[4]Institut Pasteur, Université Paris Cité CNRS UMR2000, Evolutionary genomics of RNA viruses Unit, Paris, France

[5]Institut Pasteur, Université Paris Cité, Histology platform, Paris, France

[6]EPO Experimental Pharmacology & Oncology Berlin-Buch GmbH, Berlin, Germany

[7]Institut Pasteur, Université Paris Cité, Interactomics, RNA and Immunity laboratory, Paris, France

*FT and NB contributed equally

[¥]Corresponding author (frederic.tangy@oncovita.fr)

ABSTRACT

Live-attenuated measles virus (MV) infects cancer cells through the CD46 receptor, commonly overexpressed in tumors, and replicates preferentially in cells with impaired type I interferon (IFN-I) response. To enhance immune stimulation, we engineered a C protein–deficient MV (MVdeltaC), thus eliminating a key viral antagonist of innate immunity. MVdeltaC exhibited potent oncolytic activity in a broad panel of human tumor cell lines, with a vast majority of them showing high sensitivity. This enhanced efficacy is dependent on RIG-I stimulation, mainly through the generation of defective viral genomes, which trigger apoptosis, robust IFN-I signaling and massive CXCL10 production. MVdeltaC infection induced immunogenic cell death, the release of danger signals, and the maturation of dendritic cells. *In vivo*, MVdeltaC significantly reduced tumor burden in xenografts and patient-derived xenograft (PDX) models. Intratumoral MVdeltaC administration in immunocompetent A/J mice grafted with syngeneic neuroblastoma led to complete tumor rejection in 90% of animals and long-term antitumor memory. Efficacy was dependent on CD8+ T and NK cells and was further enhanced by anti-CTLA-4 treatment or CD4+ T cell depletion. Prior measles immunization accelerated tumor clearance, indicating memory-boosted antitumor responses. These findings support the clinical potential of MVdeltaC as a strong RIG-I activator for next-generation large-spectrum anticancer therapy.

IMPACT Statement

This study presents a rationally engineered measles vaccine virus (MVdeltaC) lacking the nonstructural regulatory C protein that plays a central role in antagonizing the host innate immune response. This virus redirects viral replication toward immune activation through defective viral RNA generation triggering RIG-I–mediated innate sensing. MVdeltaC induces immunogenic tumor cell death, enhances antigen-presenting cell activation, and drives potent CD8+ T and NK cell–dependent antitumor responses *in vivo* resulting in potent tumor rejection. Its efficacy is further amplified by checkpoint blockade or preexisting measles immunity,

supporting its clinical potential as a next-generation broad-spectrum immuno-oncolytic therapy that synergizes with and builds upon existing immunotherapies.

52 **INTRODUCTION**

53 Immune checkpoint inhibition revolutionized cancer treatment with antibodies blocking PD-1,
54 PD-L1, or CTLA-4 to restore T cell activity against tumors. These therapies have shown
55 significant success in treating several malignancies, including melanoma, lung
56 adenocarcinoma, and renal cell carcinoma[1]. However, challenges such as the resistance of
57 non-infiltrated “cold” tumors[2] and immune-related side effects[3] limit the clinical efficacy of these
58 treatments. Strategies to turn "cold" tumors into immune-infiltrated "hot" tumors involve
59 enhancing tumor antigen presentation, increasing immune cell recruitment, activating T cells,
60 and boosting type I interferon (IFN-I) signaling to create an inflammatory microenvironment.
61 Immuno-oncolytic viruses (OVs) represent a promising approach, with the prime example of
62 the herpesvirus talimogene laherparepvec (T-VEC) approved for melanoma treatment[4]. More
63 recently, Daiichi Sankyo herpesvirus (G47Δ/teserpaturev (Delytact®) received conditional and
64 time-limited marketing approval in Japan as a regenerative medical treatment for malignant
65 glioma[5], and the non-replicative Ferring’s adenovirus-based gene therapy nadofaragene
66 firadenovec-vncg (Adstiladrin®) was approved for bladder cancer treatment[6]. Other OVs, such
67 as the CG Oncology’s adenovirus Cretostimogene grenadenorepvec or the Replimmune’s
68 herpesviruses Sturlimgene erparepvec and Imlygic talimogene laherparepvec, are being
69 evaluated in phase III clinical trials[7]. These trials focus on both direct tumor cytotoxicity and
70 immune response stimulation and may open the way to OVs combination with checkpoint
71 inhibitors.

72 Viruses can help establishing adaptive immune memory against the tumor by activating
73 various innate immunity sensors. Among them, retinoic acid-inducible gene I (RIG-I) and
74 melanoma differentiation-associated gene 5 (MDA5) are key cytoplasmic receptors (RIG-I-like
75 receptors, RLRs) that detect viral RNA in cells[8]. RIG-I primarily detects RNA viruses like
76 measles, influenza A virus, and hepatitis C virus[9-11]. These RLRs initiate antiviral responses
77 by triggering IFN-I and cytokine production, promoting immune cell recruitment, including
78 natural killer (NK) and T cells. Beyond their antiviral role, RIG-I and MDA5 serve as tumor
79 suppressors by recognizing abnormal RNA structures from cancer cells and triggering

80 apoptotic pathways and tumor cell death[12]. Their CARD domains interact with mitochondrial
81 antiviral signaling proteins (MAVS), initiating IFN-I release and activating the JAK/STAT
82 pathway, which induces the expression of IFN-stimulated genes (ISGs). Activation of RLR
83 pathways enhances anti-cancer immune responses, and RIG-I agonists are being explored as
84 new therapeutic agents in cancer[8]. MDA5 activation has also been shown to improve
85 checkpoint inhibitor efficacy[13,14].

86 Measles virus (MV) is an enveloped, negative sense single-stranded RNA paramyxovirus
87 responsible for measles (Fig. 1a). The attenuated Schwarz strain of MV is commonly used for
88 child vaccination. MV attenuated vaccine strains are also spontaneously oncolytic against
89 numerous types of cancers and have been evaluated in clinical trials for patients with ovarian,
90 glioblastoma, multiple myeloma, mesothelioma, head and neck, breast, and malignant
91 peripheral nerve sheath tumors[15]. MV natural tropism for tumor cells is associated with the
92 overexpression of its entry receptor CD46 on tumor cells, while efficient replication requires
93 defects in IFN-I response[16,17]. We previously observed that MV Schwarz displays spontaneous
94 oncolytic activity against numerous types of cancers, including melanoma[18], lung and colon
95 adenocarcinomas[19] and malignant pleural mesothelioma[16,17]. We and others also showed that
96 MV infection induces immunogenic death, thus leading to the maturation of both myeloid and
97 plasmacytoid dendritic cells and promoting tumor antigen cross-presentation[20-23].

98 To enhance the spontaneous oncolytic activity of attenuated MV and improve its
99 immunostimulatory capacity, we developed MVdeltaC, a C protein–deficient derivative of MV.
100 Measles C protein is a small, cytoplasmic, nonstructural protein produced from an alternative
101 open reading frame within the phosphoprotein (P) gene (Fig. 1a-b). Although lacking enzymatic
102 activity , this virulence factor is incorporated into viral ribonucleocapsids and plays important
103 roles in MV life cycle[24]. It antagonizes host innate immune responses by suppressing IFN-I
104 production[25-27]. It also modulates viral RNA synthesis by acting as a polymerase processivity
105 factor[28]. This latter function constrains the formation of defective viral genomes (DVGs),
106 particularly double-stranded RNA (dsRNA). We and others have previously demonstrated that
107 MVdeltaC produces markedly higher levels of DVGs compared to parental MV[9,29]. DVGs,

108 especially 5' copy-back defective-interfering (DI)-RNAs, are potent RIG-I agonists: their
109 double-stranded structure and 5′ triphosphate ends trigger IFN-I signaling, thereby amplifying
110 antiviral and immune responses[9,30]. In addition, the C protein promotes autophagy, delays
111 apoptosis and supports high-yield viral replication, while mitigating innate immune sensing via
112 mitophagy[31].

113 Taken together, these diverse roles make the C protein a strategic target to improve MV
114 immunogenic and oncolytic properties. We hypothesized that C protein deficiency would
115 enhance tumor cell killing by accelerating apoptosis, bypassing autophagy, and increasing
116 immunogenic visibility of the infection. To test this, we investigated the immuno-oncolytic
117 activity and mechanism of action of MVdeltaC both *in vitro* and *in vivo*. Our preclinical findings
118 demonstrate that MVdeltaC is a potent immuno-oncolytic virus against aggressive cancers.
119 With boosted RIG-I activation and IFN-I signaling, MVdeltaC represents a promising strategy
120 for improving the efficacy of immune checkpoint inhibitors and advancing cancer
121 immunotherapy.

122 **RESULTS**

123 **Generation and characterization of MVdeltaC**.

124 MVdeltaC was generated by introducing two mutations into the MV Schwarz genome
125 (GenBank accession no. AF266291.1)[32]: one disrupting the C start codon and another
126 introducing a premature stop codon (Fig. 1b), as previously described[9]. As expected,
127 MVdeltaC-infected cells did not express the C protein (Fig. 1c). Protein expression analysis at
128 early time points revealed that MVdeltaC initiated production of both the structural
129 nucleoprotein (N) and the non-structural V protein significantly earlier (8–10 h post-infection)
130 than parental MV (>21 h), indicating accelerated viral RNA accumulation (Fig. 1d). Although
131 replication in Vero cells was slightly attenuated, MVdeltaC still produced high viral titers (Fig.
132 1e, Fig S1). To evaluate the genetic stability of the introduced mutations, we performed next-
133 generation sequencing (NGS) of full-length viral genomic RNA after 5 and 10 passages on
134 Vero cells (Fig. S2). The knockout mutations remained intact, which confirmed the genetic
135 stability of MVdeltaC.

136

137 **MVdeltaC induces faster tumor cell death than parental MV.**

138 We compared the cytotoxic activity of MVdeltaC and the parental MV across a panel of human
139 cancer cell lines using the CellTiter-Glo luminescent viability assay, which measures ATP as
140 an indicator of metabolically active cells. In cervical (HeLa), lung (A549), and mesothelioma
141 (Meso 4, Meso 13 and Meso 163) cell lines, MVdeltaC induced significantly faster and more
142 extensive killing than parental MV (Fig. 2a). Extending this analysis to a panel of bladder,
143 ovarian and hepatocellular carcinoma cell lines showed that 80% of them were efficiently killed
144 by MVdeltaC (viability < 50%) (Fig. S3a-b).

145

146 **Improved MVdeltaC killing and immunogenicity depends on RIG-I signaling by DVGs.**

147 OVs exert their anti-tumor effects not only by direct killing of malignant cells, but also by
148 activating immune pathways in infected cancer cells. We and others have previously shown

149 that, while replicating, MVdeltaC generates high amounts of 5' copy-back DI dsRNA
150 genomes[9,11,28,29] that act as RIG-I agonists and strong activators of innate immunity[30,33,34].
151 To directly quantify DVG production and dissect their role in enhanced cell killing, we used
152 the human HAP1 cells. These near-haploid, myelogenous leukemia-derived cells possess a
153 functional IFN-I pathway and are available as isogenic knockouts for key innate immune
154 receptors including RIG-I, MDA5, and MAVS, making them suited to study RNA sensing
155 pathways. We first infected wild-type HAP1 cells with either MV or MVdeltaC and performed
156 NGS of total RNA collected from cell lysates 24 h post-infection. Analysis of DVGs was
157 performed using DI-tector, a validated bioinformatic tool for the unbiased detection of DVGs in
158 NGS data[35]. We confirmed that DVGs were produced in MVdeltaC- and not in MV Schwarz-
159 infected cells, consistent with the loss of C protein-mediated suppression of aberrant RNA
160 synthesis (Fig. 2b).
161 We next examined whether this enhanced DVG production translated into stronger innate
162 immune activation. Gene expression analysis in infected HAP1 cells showed that MVdeltaC
163 induced a markedly stronger innate response than parental MV, with ~250-fold higher *IFNB1*,
164 100-fold higher *TNF*, and ~10,000-fold higher *CXCL10* expression, while other genes such as
165 *MX1*, *CD274* (*PDL1*), *TNFRSF10B* (*TRAILR2*), *MICA*, and *ULBP2* were similarly regulated by
166 both viruses (Fig. 2c). In RIG-I KO cells, MVdeltaC failed to induce *IFNB1*, while *TNF* and
167 *CXCL10* were only modestly upregulated relative to MV. MDA5 KO cells displayed a wild-type-
168 like profile, whereas MAVS KO cells failed to upregulate any of the tested cytokines, except
169 for a modest 10-fold increase in *CXCL10*. In nonmalignant MRC5 fibroblasts, MVdeltaC also
170 triggered significantly stronger *IFNB1*, *TNF*, *CXCL10*, and *MX1* expression compared to
171 parental MV (Fig. S4).
172 Finally, we tested the functional consequence of this RIG-I signaling on cell killing. HAP1
173 cells were infected with MVdeltaC or parental MV at different multiplicity of infection (MOI), and
174 cell viability was assessed 24 hours post-infection. While parental MV killed wild-type and KO
175 HAP1 cells at comparable rates, MVdeltaC consistently killed wild-type and MDA5 KO cells
176 more efficiently (Fig. 2d). Importantly, this enhanced killing was abolished in RIG-I KO and

177 MAVS KO cells. Thus, the superior cytotoxic activity of MVdeltaC relies on functional RIG-I
178 and MAVS signaling, while MDA5 does not contribute to this effect.
179 Together, these results demonstrate that MVdeltaC infection of cancer cells produces
180 abundant RIG-I–stimulating DVGs, which activate MAVS-dependent signaling to drive robust
181 innate immune activation and enhanced cancer cell killing.
182
183 **MVdeltaC induces tumor rejection in immunocompetent mice.**
184 Because MV is naturally restricted to humans and non-human primates, evaluation of
185 MVdeltaC in immunocompetent mice first required the identification of murine tumor cells
186 permissive to infection. Previous studies showed that the neuroblastoma cell line NS20Y is
187 permissive to MV and, once persistently infected, fails to form tumors in immunocompetent A/J
188 mice[36]. To establish this model, we first confirmed the susceptibility of NS20Y cells to infection
189 using an MV expressing eGFP (MV-GFP). Flow cytometry analysis showed that NS20Y cells
190 were highly permissive to MV compared to MB49 mouse bladder carcinoma cells, used as a
191 non-permissive control (Fig. S5a). Fluorescence microscopy confirmed extensive infection of
192 NS20Y cells, similar to human cancer cells, whereas MB49 cells showed very low infection
193 (Fig. S5b). Infected NS20Y cells also formed large syncytia, indicating a strong fusogenic
194 activity. These results validated the use of the syngeneic NS20Y model in immunocompetent
195 A/J mice to evaluate therapeutic efficacy of MVdeltaC.
196 Following a preliminary NS20Y cells dose-range study (not shown), mice were
197 subcutaneously (s.c.) grafted with 5×10^6 cells that led to rapid tumor progression. By day 6,
198 all mice developed soft and vascularized tumors ranging from 100 to 250 mm^3 in volume. Three
199 intratumoral (i.t.) injections of MVdeltaC (2×10^6 $TCID_{50}$) were then performed on days 6, 9,
200 and 12 (Fig. 3a). By day 13, MVdeltaC-treated tumors showed significant volume reduction
201 compared to PBS controls, and immunofluorescence staining of tumor sections with anti-MV
202 N antibody confirmed intratumoral replication of MVdeltaC (Fig. 3b). Treated tumors started to
203 regress between the second and the third MVdeltaC administration and completely
204 disappeared by day 20, leading to survival in 73% of animals (Fig. 3c). To determine whether

205 MVdeltaC treatment elicited tumor-specific immune memory, cured mice were re-challenged
206 at day 65 with the same number of NS20Y cells injected into the contralateral flank (blue line
207 in Fig. 3c). None of the mice developed tumors within 40 days post re-challenge, demonstrating
208 the induction of durable, tumor-specific adaptive immune memory.

209 We next tested the impact of administration frequencies. Mice received one, three, or five
210 i.t. injections of MVdeltaC (Fig. 3d-e). Five i.t. injections resulted in complete tumor regression
211 in 90% of mice, indicating that increasing the frequency of injections significantly enhances the
212 efficacy. Finally, to directly compare MVdeltaC with the parental MV, we assessed tumor
213 control of both viruses by measuring tumor growth and tumor volumes over time. MVdeltaC
214 controlled tumors more rapidly and effectively than unmodified MV, confirming its superior
215 antitumor efficacy (Fig. 3f).

216 Altogether these results demonstrate that MVdeltaC exhibits a potent antitumor activity in
217 immunocompetent mice. Intratumoral administration led to virus replication and complete
218 tumor eradication in most treated animals and cured mice developed durable, tumor-specific
219 immune memory.

220

221 **Lymphocytes play a major role in the therapeutic activity of MVdeltaC.**

222 To assess the role of adaptive immune cells in MVdeltaC efficacy, we first examined tumor-
223 infiltrating lymphocytes (TILs) by immunohistochemistry of regressing NS20Y tumors collected
224 at day 13. Abundant infiltration of T cells was observed in MVdeltaC-treated tumors (Fig. 4a).
225 Both $CD4^+$ and $CD8^+$ T cells accumulated around the tumors and were homogeneously
226 distributed throughout the tumor tissue and accumulated around tumors, thus demonstrating
227 that MVdeltaC treatment converted the tumor microenvironment into an immunologically active
228 “hot” state.

229 We next investigated which immune cell subsets were involved in MVdeltaC immuno-
230 oncolytic activity by selectively depleting $CD4^+$, $CD8^+$ T cells, B cells, or NK cells in A/J mice
231 grafted with NS20Y neuroblastoma tumors. Flow cytometry confirmed efficient depletion of the
232 targeted immune cell subsets (Fig. S6). Depletion of $CD4^+$ T cells enhanced the therapeutic

233 efficacy of MVdeltaC (Fig 4b). All the mice in this group achieved complete tumor rejection,
234 compared to a 70% complete response rate in non-depleted controls. On day 12, at the third
235 MVdeltaC injection, tumor volumes in the $CD4^+$ T cell-depleted group were heterogeneous:
236 four mice exhibited very large tumors (mean volume = 887mm^3), whereas six mice had smaller
237 tumors (mean volume = 152mm^3, Fig. 4b). Mice with smaller tumors cleared them more rapidly
238 (by days 16-23), while mice with larger tumors achieved complete regression later (days 30–
239 49). These results demonstrate that even very large tumors can be eliminated by MVdeltaC in
240 the absence of $CD4^+$ T cells. All mice remained tumor-free up to 100 days. In contrast,
241 depletion of $CD8^+$ T cells and NK cells abrogated the therapeutic efficacy of MVdeltaC (Fig.
242 4b). Tumor growth kinetics in the absence of $CD8^+$ T cells was similar to that observed in PBS-
243 treated controls. NK cell depletion also largely eliminated therapeutic benefit. B cell depletion
244 also impaired the efficacy of MVdeltaC treatment, albeit to a lesser extent than $CD8^+$ T cell or
245 NK cell depletion. Only 40% of B cell-depleted mice exhibited complete tumor response,
246 indicating that while B cells contribute to the therapeutic outcome, they are not as crucial as
247 $CD8^+$ or NK cells.

248 Taken together, these findings indicate that $CD4^+$ and $CD8^+$ T cells play critical but
249 opposite roles in MVdeltaC therapy. Depletion of $CD4^+$ T cells enhances the therapeutic
250 efficacy of MVdeltaC, likely *via* Treg removal, whereas the absence of cytotoxic $CD8^+$ T cells
251 and NK cells completely abolishes the immuno-oncolytic efficacy of MVdeltaC, resulting in
252 progressive disease. Intratumoral administration of MVdeltaC thus promotes significant
253 infiltration of both $CD4^+$ and $CD8^+$ T cells into the tumor microenvironment, transforming it into
254 an immunologically "hot" state and supporting tumor rejection through the induction of adaptive
255 antitumor immunity.

256

257 **Preexisting measles immunity does not impair MVdeltaC efficacy.**

258 Since most humans are immunized against measles through vaccination or infection, we
259 assessed whether this preexisting immunity affects MVdeltaC therapy. We immunized mice
260 with the parental MV (MV-immunized group) or PBS (MV-naïve controls). Thirty-eight days

261 later, high MV-specific IgG antibody titers confirmed successful immunization (Fig. S7). Mice
262 were then grafted s.c. with NS20Y tumors and treated with MVdeltaC starting on day 6. Tumor
263 responses were comparable: complete response rates were 77.7% in MV-naïve and 71.4% in
264 MV-immunized mice (Fig. 5a), with no significant survival differences (Fig. 5b). Notably, tumor
265 clearance was faster in immunized mice (median 21 vs. 33 days), though not statistically
266 significant (Fig. 5c). These results suggest that preexisting measles immunity does not
267 diminish, and may even accelerate, MVdeltaC-mediated tumor clearance.
268
269 **Synergistic activity of MVdeltaC with anti-CTLA4 immune checkpoint inhibitor and**
270 **abscopal effect.**
271 Considering the immunotherapeutic potential of MVdeltaC, we next tested MVdeltaC in
272 combination with immune checkpoint blockade targeting CTLA-4 (Fig. 5d). In NS20Y-bearing
273 mice, MVdeltaC monotherapy resulted in a complete response in 60% of treated mice, anti-
274 CTLA-4 monotherapy led to complete tumor clearance in 82% of animals, whereas
275 combination therapy of MVdeltaC and anti-CTLA-4 resulted in complete tumor regression in
276 100% of mice, demonstrating the additive or synergistic effects of both therapies. This finding
277 highlights the translational potential of MVdeltaC as a promising component for combination
278 immunotherapy regimens.
279 Finally, we assessed whether MVdeltaC could elicit systemic antitumor responses against
280 untreated contralateral tumors in a double-tumor model. Although the NS20Y model in A/J
281 mice is very aggressive – tumors grow very fast compared to the establishment of the adaptive
282 CD8 responses – a notable antitumor response was observed after treatment with MVdeltaC.
283 Specifically, 10 out of 12 mice treated with MVdeltaC showed a decrease in tumor volume in
284 the injected tumors. Among these, 4 mice (40%) achieved complete regression of both injected
285 and non-injected tumors (Fig. 5e). This abscopal activity indicates that MVdeltaC can generate
286 systemic antitumor immunity capable of controlling distant lesions.
287

288 **Translating the immuno-oncolytic activity of MVdeltaC in patient-derived cancer cells.**
289 With the aim to translate the development of MVdeltaC to human cancers, we analyzed its
290 oncolytic capacity against a collection of human pleural mesothelioma (PM) cells. We
291 previously studied the varying susceptibility of human PM cells to MV replication[16]. Here, using
292 fluorescent microscopy, we analyzed the infection of twelve PM cell lines by MVdeltaC-eGFP
293 (Fig. 6a-b and S8 + S9). As expected, healthy mesothelial cells (MES-F and LP-9) (Fig. 6a-b),
294 as well as fibroblasts and endothelial cells (Fig. S8a) were resistant to both MV and MVdeltaC,
295 confirming the tumor selectivity of oncolytic MV. Meso 4 cells known to be resistant to parental
296 MV at low MOI were also resistant to MVdeltaC replication, whereas most PM cell lines were
297 permissive (Fig. 6 a-b, S8b, S9b). GFP expression intensity was lower in MVdeltaC-infected
298 cells compared to parental MV (Fig. 6a + S9), which confirmed lower viral replication, even if
299 the proportions of infected cells were similar between both viruses (Fig. 6b).
300 To examine cell death induction, we analyzed caspase-3/7 activation over time by
301 fluorescence microscopy (Fig. 6c, S10d) and a luminescence bioassay (Fig. 6d, S10a-c).
302 MVdeltaC triggered apoptosis earlier than parental MV, with robust caspase-3/7 activation
303 observed as early as 48 h post-infection in sensitive lines, compared to 96 h for MV (Fig. 6c).
304 Quantification of caspase-3/7 activation in twelve human MPM cell lines over 6 days confirmed
305 that MVdeltaC elicited enhanced apoptosis in several models (Fig. 6d, S10a-d). Meso 11,
306 Meso 13, Meso 76 and Meso 225 showed enhanced oncolytic activity of MVdeltaC over MV,
307 whereas Meso 34, Meso 47 and Meso 163 showed similar activation of caspase-3/7 between
308 MV and MVdeltaC (Fig. 6d, S10a-b). Interestingly, two cell lines, Meso 35 and Meso 56,
309 appeared to be resistant to MVdeltaC but not to MV (Fig. S10b). The three cell lines resistant
310 to MV (Meso 4, Meso 150, Meso 173) were also resistant to MVdeltaC (Fig. S10c-d). Notably,
311 while at standard MOI of 1 Meso 4 was resistant to replication and killing, this cell line was
312 nevertheless killed when using higher MOIs of 5 and 10 (Fig. 2a).
313 Together, these results demonstrate that MVdeltaC efficiently infects and kills a large
314 majority of patient-derived PM cell lines by inducing faster apoptotic death than the parental
315 MV, while retaining selectivity for malignant over normal mesothelial and stromal cells.

316

317 **MVdeltaC accumulates viral dsRNA, triggers the release of danger signals and activates**
318 **dendritic cells.**

319 We next determined whether MVdeltaC infection resulted in the accumulation of viral dsRNA
320 in the cytoplasm of infected human PM cells. Indeed, confocal microscopy revealed that
321 dsRNAs were present in MVdeltaC-infected cells but absent in parental MV-infected or
322 uninfected cells (Fig. 7a).

323 Immunogenic cell death (ICD) is characterized by the release of molecules of danger-
324 associated molecular patterns (DAMPs), such as ATP, calreticulin, or HMGB1, which act as
325 signals to activate DCs and prime adaptive immune responses. Both MV and MVdeltaC
326 infection induced HMGB1 release during tumor cell death, with higher amounts being released
327 from MVdeltaC-infected tumor cells (Fig. 7b-c). We then tested the functional immunogenicity
328 of MVdeltaC-induced cell death by evaluating its ability to promote the maturation of human
329 monocyte-derived immature dendritic cells (iDCs) from six healthy donors, either directly or
330 after infection of PM cells (Fig. 7d-e). As expected, direct exposure of iDCs to MV or MVdeltaC
331 induced the expression of the CD83 maturation marker on their surface. This effect was
332 completely abrogated when both viruses were previously UV-inactivated, indicating that viral
333 replication is necessary to induce DC maturation. We previously showed that infection of Meso
334 13 cells by parental MV Schwarz promoted iDC maturation[20]. Infection of Meso13 cells with
335 MVdeltaC at the same MOI further enhanced this activation, thereby showing superior activity
336 of MVdeltaC at inducing ICD and activating antigen-presenting cells (Fig.7e). Control Meso 13
337 cells left untreated or induced into apoptosis by ultraviolet radiation did not trigger DC
338 maturation.

339 Altogether, these results demonstrate that MVdeltaC infection of patient-derived tumor
340 cells leads to dsRNA accumulation, danger signal release, and efficient induction of DC
341 maturation — hallmarks of ICD that support initiation of antitumor immune responses.

342

343 **MVdeltaC controls human cancers in orthotopic and PDX models.**

344 To assess MVdeltaC oncolytic activity *in vivo* against patient-derived tumor cells, we first
345 performed orthotopic xenograft experiments in NOD/SCID mice. These animals lack functional
346 T and B lymphocytes, have very low NK cell activity and an absence of hemolytic complement,
347 while macrophages and DCs are present but functionally impaired. Of the seven MVdeltaC-
348 sensitive human PM cell lines tested, only Meso 34 and Meso 163 successfully established
349 tumors in the peritoneal cavity. Three weeks post-grafting for Meso 163 and two months for
350 Meso 34, mice received a single low-dose i.p. injection of MVdeltaC (2×10^5 $TCID_{50}$) or control
351 PBS. Two weeks later, tumor burden was significantly reduced in the MVdeltaC-treated group
352 for both cell lines compared to control animals (Fig. 8a). MVdeltaC treatment efficiently reduced
353 the number and the size of tumors in the peritoneum (Fig. 8b). Histology analysis revealed that
354 tumor density was strongly decreased in animals treated with MVdeltaC compared to control
355 mice (Fig. 8c).

356 To evaluate whether the oncolytic effect of MVdeltaC extends beyond PM, we next tested
357 human melanoma and triple-negative breast cancer (TNBC) xenografts. In NOD/SCID mice
358 bearing subcutaneous M6 human melanoma xenografts, i.t. administration of MVdeltaC
359 significantly reduced tumor growth compared to PBS-treated controls (Fig. 8d). Similarly, in
360 NMRI nu/nu mice (deficient in T lymphocytes but retaining NK cells, DCs, macrophages, and
361 an intact complement activity) s.c. xenografts of the human TNBC cell line MDA-MB-231 were
362 efficiently controlled by weekly i.t. injections of MVdeltaC (Fig. 8e). As these mice lack T cell
363 memory, repeated virus administration was required throughout the study.

364 Tumor models based on established tumor cell lines have the disadvantage of low
365 heterogeneity[37]. Therefore, we next evaluated MVdeltaC in patient-derived mesothelioma
366 xenografts (PDX) serially passaged in NMRI nu/nu mice. Four PDX models established from
367 patients with pleural or peritoneal mesothelioma were selected: Meso7212, Meso12962,
368 Meso13852B and Meso14275[38,39]. When tumors reached ~100 to 250 mm^3, mice received
369 weekly i.t. injections of MVdeltaC. Two doses of MVdeltaC were tested: 1×10^5 and 1×10^6
370 $TCID_{50}$ per injection. MVdeltaC treatment significantly inhibited tumor growth across all four
371 PDX models at both doses (Fig. 8e and Fig.S11). According to the modified RECIST criteria[40],

372 treatment responses in Meso7212 and Meso12962 tumors were stable disease, whereas
373 treatment with the higher dose induced partial response (Fig 8f). Therapy was well tolerated
374 without side effects nor body weight loss (not shown).

375 Together, these findings establish MVdeltaC as a broad-spectrum oncolytic virus with
376 potent activity across mesothelioma, melanoma, and TNBC models, highlighting its
377 translational potential for clinical development in multiple solid tumor indications.

378

379 **DISCUSSION**

380 In this study, we investigated the immuno-oncolytic potential of MVdeltaC, a modified measles
381 vaccine virus in which the nonstructural regulatory protein C, which plays a central role in
382 antagonizing the host innate immune response, was deleted. We observed that MVdeltaC
383 virus kills more rapidly and more effectively tumor cells than the parental virus *in vitro* and *in*
384 *vivo*. We then demonstrated that this enhanced anticancer activity depends on RIG-I activation
385 by DVGs generated by the modified virus, leading to rapid and strong expression of pro-
386 inflammatory cytokines and chemokines. In consequence, both the virus and the infected
387 tumor cells become more visible to the host immune system. Such activity promotes strong
388 DC maturation and the recruitment of immune cell (CD8+ T cells, NK cells) into the tumor that
389 participate to the killing of tumor cells.

390 MVdeltaC demonstrated potent anti-cancer effects *in vitro*, inducing rapid tumor cell death
391 in over 40 human cancer cell lines, including mesothelioma, lung adenocarcinoma, bladder
392 cancer, ovarian cancer, hepatocarcinoma, and cervical cancer. MVdeltaC killed cells more
393 rapidly and more extensively than parental MV and remained unable to spread in non-
394 malignant cells, as deletion of the C protein further attenuated the virus. Tumor cell death was
395 associated with the release of large quantities of danger signals, including cellular (HMGB1)
396 and viral (dsRNA) components. Extremely high levels of *IFNB1*, *TNF* and *CXCL10* were
397 induced in dying cancer cells, with as much as 10,000 times more *CXCL10* expression than
398 after infection by standard MV. Notably, the strong induction of *CXCL10* suggests a
399 mechanism by which MVdeltaC could promote the recruitment of immune cells into the tumor
400 microenvironment.

401 *In vivo*, MVdeltaC effectively inhibited tumor growth in immunodeficient mouse models. In
402 NOD/SCID mice grafted orthotopically with human mesothelioma cells, a single, low-dose
403 intraperitoneal injection significantly reduced tumor mass within two weeks. Similar efficacy
404 was confirmed in mice bearing TNBC and human melanoma cells, as well as against
405 mesothelioma PDX. In immunocompetent A/J mice grafted with syngeneic neuroblastoma
406 cells, three i.t. injections of MVdeltaC led to complete tumor rejection in 70% of animals, and

407 five injections in 90% of them. Treatment also generated immune memory, as surviving
408 animals rejected tumor re-challenge. Regressing tumors exhibited massive infiltration of CD8+
409 and CD4+ T cells, and depletion studies revealed that MVdeltaC efficacy was dependent on
410 CD8+ T lymphocytes and NK cells, while depletion of CD4+ T cells or a combination with anti-
411 CTLA-4 enhanced efficacy. Even though the NS20Y model is very aggressive and we had to
412 treat large tumors, an abscopal effect was also observed likely due to CD8+ T cell and NK cell
413 activity. While $CD8^+$ T cells are essential for long-term tumor control, their efficacy is
414 significantly diminished in the absence of NK cells. NK cells likely play a crucial role in the early
415 recognition and killing of MVdeltaC-infected tumor cells, which may be necessary to initiate an
416 effective $CD8^+$ T cell response. Without this early innate activation, $CD8^+$ T cells may receive
417 insufficient priming and fail to control rapidly growing tumors. Importantly, prior measles
418 immunity did not hinder efficacy but rather accelerated anti-tumor responses. This is a major
419 finding considering that a vast majority of the population is immune to MV and that the actual
420 clinical impact of both cellular and humoral immune responses directed against OVs is still
421 debated.

422 This work demonstrates that by introducing two point mutations into the 15,894
423 nucleotides of the measles vaccine virus genome, we generated a highly immuno-oncolytic
424 virus with a greater capacity to kill cancer cells and to elicit strong immunostimulatory
425 responses prone to attract and activate immune cells into the tumor microenvironment.
426 Unmodified MV live-attenuated strains are naturally oncolytic against many malignancies[15] and
427 are currently evaluated clinically for patients with different types of cancers[41]. Modifications of
428 oncolytic MV were first mainly focused on increasing its safety, for example by inserting the
429 *IFNB1* gene into the MV genome or by retargeting the virus toward alternative tumor-specific
430 receptors. Considering the advances in cancer immunotherapy, most of the modification of
431 OVs now focus on increasing their immuno-activating properties. Particularly with MV, a
432 number of modifications have been proposed, such as inserting GM-CSF, IL12, or anti-PD1
433 and anti-CTLA4 single chain antibodies sequences into the virus genome[42-45].

434 The enhanced tumor cell killing activity and immunogenicity of MVdeltaC relies on a
435 functional RLR pathway. RIG-I and MDA5 are critical in the body's antiviral defense, but their
436 roles extend into cancer biology as potential tumor suppressors and immunotherapy targets
437 [8,46-50]. Their pathways may be exploited to enhance anti-cancer immune responses. RIG-I and
438 MDA5 can both function as tumor suppressors by detecting viral infections and abnormal RNA
439 structures produced by cancer cells, particularly when RNA splicing and editing are disrupted
440 or when endogenous retroviruses are expressed in the form of dsRNA[51]. They trigger an
441 immune response that may inhibit tumor growth or even promote the destruction of cancer
442 cells. MDA5 was originally identified in melanoma, and its activation has shown anti-tumor
443 activity in this type of cancer. Activation of the RLR pathway leads to the production of IFN-I
444 and pro-inflammatory cytokines, thereby promoting an anti-tumor immune response by
445 recruiting immune cells like NK cells and T cells to attack cancer cells[47-50]. Mutations in cancer
446 cells can inhibit RIG-I or MDA5 signaling, allowing tumors to evade immune detection. For
447 instance, some cancers may suppress the expression of IFN-I or downstream signaling
448 proteins to escape immune surveillance, thereby aiding cancer progression [52,53]. RIG-I
449 agonists are currently being explored as therapeutic agents in cancer[54]. These agonists can
450 mimic viral RNA to stimulate an immune response that targets tumors, making RIG-I a focus
451 for cancer immunotherapy. Similarly, activating MDA5 has been shown to enhance checkpoint
452 inhibitor therapies (like anti-PD-1/PD-L1 antibodies), potentially improving the efficacy of
453 immunotherapies in treating various cancers such as melanoma[47].
454 In conclusion, we reframed oncolytic MV into an immunotherapeutic virus by genetically
455 disarming it to favor immune stimulation over viral dissemination, a major safety advantage.
456 The unique immunogenic features of MVdeltaC make it a potential candidate for combination
457 with other immunotherapies. Our findings suggest that the anticancer efficacy of MVdeltaC is
458 driven by both direct oncolysis and its capacity to convert the tumor into an immunogenic niche,
459 offering a promising platform for combination with immune checkpoint blockade or cancer
460 vaccines. Indeed, i.t. injections of oncolytic viruses, TLR agonists, or STING agonists are being
461 developed to trigger immune responses by turning “cold” tumors into “hot,” immune-infiltrated

462 ones[55]. MVdeltaC, which is based on a human vaccine with a long-standing an unmatched
463 safety profile, demonstrated by its use for decades for vaccination against measles, is a
464 promising candidate for combined anti-tumor immunotherapeutic strategies. It has now
465 entered GMP manufacturing and is expected to begin Phase I clinical trials soon.

466 **MATERIALS & METHODS**

467

468 **Generation of MVdeltaC virus.** For MVdeltaC virus cloning, we used the plasmid vector pTM-
469 MVSchw, which contains an infectious MV cDNA corresponding to the anti-genome of the
470 Schwarz MV vaccine strain (GenBank accession no. AF266291.1) and has been described
471 elsewhere [32]. MVdeltaC construct was generated by site-directed mutagenesis on a cassette
472 vector covering the P gene sequence. The second translation initiation codon present in the
473 N-terminal P ORF in the "1 frame was mutated (U -> C), and then a substitution (G -> A) was
474 generated at nucleotide position 1845 of the MV genome to introduce a stop codon within the
475 C ORF. Both mutations do not disturb the P and V ORFs (Fig. 1d). Rescue of MVdeltaC virus
476 was performed using a helper-cell-based system [32]. Briefly, helper HEK293-T7-NP cells were
477 transfected with 5 µg of pTM-MVdeltaC and 0.02 µg of pEMC-La expressing the MV
478 polymerase L gene. After overnight incubation at 37 °C, the transfection medium was replaced
479 by fresh medium, and a heat shock was applied for 3 h at 42 °C and then returned to 37 °C.
480 After two days of incubation at 37 °C, transfected cells were transferred to 100-mm dishes with
481 monolayers of Vero cells (ATCC, CCL-81). Syncytia that appeared after 2–3 days of co-culture
482 were singly picked and transferred onto Vero cells seeded in six-well plates. Infected cells were
483 trypsinized and expanded in 75-cm^2 and then 150-cm^2 flasks, in DMEM with 5% Fetal Bovine
484 Serum (FBS, Gibco). To collect viruses, cells were scraped into a small volume of OptiMEM
485 (Thermo Fisher), lysed by a single freeze-thaw cycle and cell lysates clarified by low-speed
486 centrifugation. The infectious supernatant was then collected and stored at −80 °C. Titer of
487 MVdeltaC was determined on Vero cells seeded in 96-well plates infected with serial ten-fold
488 dilutions of virus in DMEM with 5% FBS. After incubation for 7 days, cells were stained with
489 crystal violet, and TCID50 values were calculated using the Karber method [56]. MV-eGFP,
490 MVdeltaC-eGFP, MV-mCherry and MVdeltaC-mCherry were cloned, produced, purified and
491 titrated as previously described[32].

492

493 **Virus growth curves**. Monolayers of Vero, HEK293, A549 and HeLa cells in 24-mm-diameter
494 dishes (6-well plates) were infected with MVdeltaC or MV-Schwarz at an MOI of 1. At various
495 times post infection, cells were scraped into culture medium. After freeze-thawing of cells in
496 their medium and clarification of cell debris, virus titers were determined as described above.
497
498 **Virus Sequencing.** RNA was extracted from the clarified cell supernatants using the QIAamp
499 Viral RNA Kit (Qiagen) following the manufacturer's instructions. MV genome was reverse
500 transcribed into cDNA and amplified by PCR using previously described primers[32]. Libraries
501 were prepared using a Nextera XT kit (Illumina), before sequencing on an Illumina NextSeq500
502 (2 × 75 cycles). Raw sequence data were deposited in the Sequence Read Archive
503 (https://www.ncbi.nlm.nih.gov/sra) under BioProject ID PRJNA1309675. For bioinformatic
504 analysis, adaptors and low-quality sequences of raw reads were removed using Trimmomatic
505 v.0.39[57]. We assembled the trimmed reads using megahit v.1.2.9[58] with default parameters.
506 Raw reads were then mapped on the viral scaffold. The mapping data were visually checked
507 to confirm the accuracy of the genomes using Geneious Prime 2025. Consensus, coverage
508 statistics and intrasample single-nucleotide variants (iSNVs) estimates were obtained using
509 iVar[59].
510
511 **Western blot analysis**. Vero cells in six-well plates were infected with MVdeltaC or MV at an
512 MOI of 0.1. At 36–48 h post-infection, infected cells were lysed in RIPA lysis buffer (Thermo
513 Fisher). Samples were briefly centrifuged and subjected to 4–12% gradient on a NUPAGE-
514 PAGE gel (Invitrogen). After transfer to a nitrocellulose membrane (GE Healthcare), the
515 membrane was subsequently probed with a rabbit polyclonal anti-MV C antibody (Pr Takeuchi,
516 Tsukuba University, Japan, 1:2000 dilution) followed by a horseradish peroxidase (HRP)-
517 conjugated swine anti-rabbit IgG antibody (P0399, Dako, 1:3000 dilution). Bands were
518 visualized using SuperSignal West Pico Plus chemiluminescent HRP substrate (Thermo
519 Fisher). For loading controls, membranes were stripped with 5% NaOH for 5 min and re-probed

520 with a mouse monoclonal anti-MV-N antibody (ab9397, Abcam, 1:20,000 dilution) followed by
521 an HRP-conjugated anti-mouse IgG (NA931V, GE Healthcare, 1:10,000 dilution).
522
523 **Cell culture.** Human mesothelioma cell lines (Meso 4, Meso 11, Meso 13, Meso 34, Meso 35,
524 Meso 47, Meso 56, Meso 76, Meso 150, Meso 163, Meso 173 and Meso 225) were established
525 from pleural effusions and genetically characterized (Biocollection DC-2011–1399, CHU
526 Nantes, France) [60]. The human melanoma cell line M6 was a kind gift from Nathalie Labarrière
527 (INCIT, biocollection PC-U892-NL, CHU Nantes, France). The cell lines were cultured at 37°C
528 and 5% CO_2 in Roswell Park Memorial Institute Medium (RPMI)-1640 supplemented with 2
529 mM L-Glutamine, 100 IU/mL Penicillin, 100 µg/mL Streptomycin (all from Gibco), and 10%
530 heat-inactivated FBS (Corning). Normal peritoneal mesothelial cells MES-F and LP-9 were
531 purchased from Tebu-bio and the Coriell Institute, respectively, and cultured in their specific
532 medium according to the manufacturers' recommendations. Mouse neuroblastoma cell line
533 NS20Y (DSMZ# ACC 94), A549 cells human adenocarcinoma alveolar basal epithelial cells,
534 and HeLa cervical cancer cells were cultured in Dulbecco's modified Eagle's medium (DMEM)
535 supplemented with 10% of heat-inactivated FBS, and 100 U/ml penicillin, 100 U/ml
536 streptomycin (Thermo Fisher) in a 5% CO_2 atmosphere. Cells were routinely checked for
537 Mycoplasma contamination (PlasmoTest, InvivoGen).
538
539 **Virus infection of mesothelioma cells.** MV and MVdeltaC infections were analyzed by time-
540 lapse fluorescence microscopy. One day before infection, healthy cells and mesothelioma cell
541 lines were seeded in 24-well plates at a density of 1.5×10^5 cells per well. Cells were infected
542 with MV-eGFP or MVdeltaC-eGFP (MOI 1) and images were acquired every 10 minutes for 3
543 to 4 days with a Leica DMI6000B microscope using a 10X objective and the MetaMorph®
544 Microscopy Automation & Image Analysis Software (version 7.8) at the MicroPICell core facility
545 (Nantes, France). Subsequent analyses were performed with the Fiji software [61].
546

547 **Cell viability and cell death analyses.** Cell viability was assessed using the CellTiter-Glo
548 Luminescent Cell Viability Assay (Promega, Cat# G7571), according to the manufacturer's
549 instructions. Briefly, cells were seeded at a density of 4×10^4 cells per well in 50 µL of culture
550 medium in white, flat-bottom 96-well plates (Corning). Virus stocks were diluted to achieve
551 MOIs of 1, 5, or 10, and 50 µL of the viral dilution was added to each well immediately after
552 seeding. Infections were performed in triplicate. Plates were incubated at 37 °C with 5% CO_2
553 for 3–6 h to allow viral entry, followed by medium replacement to remove residual inoculum. At
554 24 to 96 h post-infection, 100 µL of culture supernatant was removed, and 100 µL of CellTiter-
555 Glo reagent was added directly to the wells. Luminescence was recorded using an EnSpire
556 Multimode Plate Reader (PerkinElmer).
557 Caspases-3/7 activation was measured in infected cells by either luminescence assay or
558 fluorescence microscopy. For the luminescence assay, mesothelioma cells were seeded in a
559 96-well plate at a density of 15,000 cells per well and cultured for 24h. Cells were then infected
560 with either MV or MVdeltaC as described above. Caspases-3/7 activity was quantified daily
561 from day 2 to day 6 using the Caspase-Glo® 3/7 assay kit (Promega). Briefly, 100 µl of
562 Caspase-Glo® reagent was added onto the cells and incubated at room temperature for 1h.
563 The luminescent signal of each sample was then measured for 1 second using a Mithras LB
564 940 luminometer (Berthold Technologies).
565 For the microscopy experiments, cells were seeded in a 96-well plate at a density of 50,000
566 cells per well. After 24h, cells were infected with either MV-mCherry or MVdeltaC-cherry as
567 described above. Viral inoculum was replaced by fresh culture medium mixed with NucView®
568 405 caspase-3 substrate (Ozyme) at a final concentration of 1µM. Images were acquired every
569 day for 4 days with an Axio Observer Z1 microscope and the ZEN software (Carl Zeiss).
570 Images were further analyzed with the Fiji Software.
571 Quantities of HMGB1 protein released from dying cells were measured by ELISA (IBL
572 International) according to the manufacturer's instructions 72h after infection of 0.5×10^6
573 mesothelial or mesothelioma cells with MV or MVdeltaC (MOI 1) in 6-well plates.
574

575 **dsRNA immunofluorescence staining.** One day before infection, PM cells were seeded in
576 µ-Slides 8-well plates (ibidi) at a density of 40,000 cells per well. Cells were infected with either
577 MV-eGFP or MVdelta-eGFP (MOI 1). dsRNA staining was performed at 48h post-infection.
578 Briefly, cells were fixed with PBS containing 4% paraformaldehyde (PFA, Electron Microscopy
579 Sciences) for 5 min, followed by PBS washes. Cells were then permeabilized with PBS
580 containing 0.1% Triton X-100 (Sigma-Aldrich) for 10 min. Plates were incubated with an anti-
581 dsRNA antibody (clone J2, English & Scientific Consulting) diluted in PBS containing 0.1%
582 Triton X-100 for 1h at room temperature, followed by 2 PBS washes. Cells were then incubated
583 with an Alexa Fluor 647-coupled anti-mouse secondary antibody (Molecular Probes, Thermo
584 Fisher Scientific) for 20 min at room temperature. The slides were then washed twice with
585 PBS. Nuclei were stained with Hoechst (Thermo Fisher Scientific) for 5 min. Finally, cells were
586 fixed for 20 min in PBS 4% PFA and then stored in PBS 0.5% PFA until analysis with a Nikon
587 A1RS fluorescence confocal microscope (MicroPICell core facility).
588
589 **RNA extraction and quantitative real-time PCR in HAP cells.** HAP, HAP RIG-I KO, HAP
590 MDA5 KO, and HAP MAVS KO cells were infected at an MOI of 1 with MV Schwarz, MVdeltaC,
591 or left uninfected (mock), and incubated at 37°C in a humidified atmosphere containing 5%
592 CO_2. Total RNA was extracted 24 hours post-infection using the RNeasy Mini Kit (QIAGEN)
593 according to the manufacturer's instructions. RNA concentration and purity were assessed
594 using a NanoDrop spectrophotometer (Thermo Fisher Scientific). Expression levels of selected
595 genes were quantified using one-step real-time PCR with the TaqMan RNA-to-Ct 1-Step Kit
596 (Thermo Fisher), following the manufacturer's protocol. One hundred nanograms of total RNA
597 were used per reaction with 20X TaqMan Gene Expression Assays (*CXCL10*:
598 Hs00171042_m1; *TNF*: Hs00174128_m1; *MX1*: Hs00895608_m1; *CD274*: Hs00204257_m1;
599 *TNFRSF10B*: Hs00366278_m1; *MICA*: Hs00792195_m1; *ULBP2*: Hs00607609_m1; *GAPDH*:
600 Hs02786624_g1; *IFNB1*: Hs01077958_s1) (Life Technologies). All reactions were performed
601 in triplicate on the QuantStudio™ 6 Flex Real-Time PCR System (Applied Biosystems). Target

602 gene expression levels were normalized to the endogenous control GAPDH, and relative
603 expression was calculated using the comparative Ct method (ΔΔCt).
604
605 **Virus Sequencing from infected HAP cells.** HAP cells were infected at an MOI of 1 with MV
606 Schwarz, MVdeltaC, MV 2N (MV Schwarz virus expressing two copies of the N protein; used
607 as a positive control) or left uninfected (mock). Cells were incubated at 37 °C in a humidified
608 atmosphere containing 5% CO_2. Total RNA was extracted 24 hours post-infection using the
609 RNeasy Mini Kit (QIAGEN) according to the manufacturer's instructions. RNA quality and
610 integrity were assessed using the Agilent RNA 6000 Nano Kit (Agilent Technologies) on the
611 Agilent 2100 Bioanalyzer system. The RNA Integrity Number (RIN) was used as a quality
612 control metric for downstream applications. Libraries were prepared from 150 ng of RNA using
613 the Illumina Stranded Total RNA Prep with Ribo-Zero Plus kit (Illumina), according to the
614 manufacturer's protocol, with 13 PCR cycles. Unbound adaptors and primers were removed
615 by two successive purifications using AMPure beads (Beckman Coulter) at a 0.8:1 bead-to-
616 sample ratio. The resulting libraries contained fragments ranging from 200 to 1000 bp, with a
617 peak around 450 bp, as determined on a 5300 Fragment Analyzer (Agilent Technologies).
618 Then, libraries were pooled, diluted to 0.75 nM, and sequenced on a NextSeq 2000 system
619 (Illumina) with a P1 100-cycle kit to generate 58-base paired-end reads (40–50 million reads
620 per sample).
621
622 **Defective interfering RNA genomes (DI RNA) bioinformatic analysis.** To identify potential
623 DI RNA, merged FASTQ files were analyzed using the Python script, DI-tector (http://www.di-
624 tector.cyame.eu/)[35], with the minimum segment length set to 25. Reads that aligned perfectly
625 to the viral reference genome (GenBank accession number no. FJ211590) were excluded.
626 Reads aligning to two separate parts of the viral genome on either side of a junction, indicative
627 of a breakpoint and reinitiation site, were then extracted and classified as DVGs.
628

629 **Co-culture of infected tumor cells with human monocyte-derived dendritic cells.** Human
630 PBMCs were obtained from platelet apheresis residues of healthy donors after informed
631 consent (Etablissement Français du Sang, Nantes, France) under the agreement NTS-2014–
632 06. After Ficoll density gradient centrifugation (Eurobio-AbCys), monocytes were purified from
633 PBMCs by counterflow centrifugation elutriation using a Beckman Avanti J20 centrifuge
634 equipped with a JE5.0 rotor and a 7 mL elutriation chamber (DTC core facility, CIC-BT-0503,
635 Nantes, France). Monocyte purity (> 85%) was assessed by flow cytometry. Monocytes were
636 differentiated into DCs in 6-well plates at 2×10^6 cells/mL in RPMI-1640 supplemented with
637 2 mM L-glutamine, 100 U/mL penicillin, 100 µg/mL streptomycin and 2% (v/v) human albumin
638 (Laboratoire Français de Fractionnement et de Biotechnologies), 1,000 U/mL recombinant
639 human GM-CSF and 200 U/mL recombinant human IL-4 (both from CellGenix). Immature DCs
640 (iDC) were harvested at day 6 and cultured for 24h at 1×10^6 cells/mL in 24-well under different
641 treatment conditions. After 24h, DC maturation was assessed by flow cytometry (FACS Canto
642 II, CytoCell core facility, Nantes, France) after double staining with a PE-conjugated anti-HLA-
643 DR antibody (clone AC122, Miltenyi Biotec) and a BV421-conjugated anti-CD83 antibody
644 (clone HB15e, BD Biosciences). The percentage of matured DCs was determined as $CD83^+$
645 cells among all $HLA\text{-}DR^+$ cells. All flow cytometry analyses were performed using the FlowJo
646 software (version 7.6.5, FlowJo LLC).
647
648 **NOD SCID mice studies.** Six-week-old female NOD SCID mice were obtained from Charles
649 River Laboratories. Mesothelioma xenograft models were established by challenging the mice
650 intraperitoneally with 5×10^6 Meso 34 or Meso 163 cells. Three weeks or two months post-
651 challenge for Meso 163 and Meso 34, respectively, mice were randomized into three groups
652 and injected intraperitoneally with 100 µL of control saline (PBS), MV-eGFP (2×10^5 $TCID_{50}$)
653 or MVdeltaC-eGFP (2×10^5 $TCID_{50}$). Fifteen days after treatment, animals were sacrificed, and
654 metastatic nodules or residual tumor tissues were collected and fixed in 4% paraformaldehyde
655 (Electron Microscopy Sciences) for weighing. The M6 melanoma xenograft model was
656 established by challenging the mice subcutaneously with 1×10^6 cells. Mice were injected

657 intratumorally twice at days 10 and 17 post-challenge with control saline (PBS), MV or
658 MVdeltaC. Tumor growth was measured every 4-5 days with a digital caliper and tumor
659 volumes were calculated according to V = (length × (width)^2/2. For histological examination,
660 the paraformaldehyde fixed, paraffin-embedded sections of tumors and surrounding invaded
661 tissues, when present, were cut with a Bond Max automaton (Menarini) and stained with
662 hematoxylin-phloxine-saffron (HPS). Slides were scanned with a Nanozoomer 2.0 HT
663 (Hamamatsu Photonics). These protocols were approved by the local ethical committee (CEEA
664 PdL n°6) and the French Ministry of Research (#01257.03).

665

666 **PDX studies.** The primary human mesothelioma PDX models were derived from patients with
667 pleural or peritoneal mesothelioma and used as xenotransplantation model in immunodeficient
668 female NMRI:nu/nu mice. The models were established by the EPO Berlin-Buch GmbH [2].
669 The tumors were propagated *in vivo* and tumor tissue from one *in vivo* passage were used for
670 s.c. implantation in the inguinal region of female nude mice. After an acclimatization time of 4
671 days, tumor fragments (2x2mm / mouse) from an *in vivo* passage were transplanted s.c. into
672 13 female nude mice (day 0). For tumor transplantation the animals were anesthetized by a
673 single intravenous injection (0.10 mL / mouse) with Propofol-® Lipuro (0.5 mg / mouse). The
674 skin of the mice was disinfected with isopropanol (70 % v/v). A superficial vertical incision in
675 the skin of 5-6 mm on the left flank was performed. The tip of a surgical scissor was inserted
676 into the incision and was used to form a pocket in the subcutaneous space. One tumor
677 fragment per mouse was implanted into the pocket using surgical tweezers. Finally, the incision
678 was closed with a metal clip. Studies were performed under Biosafety level S2. After the
679 xenotransplantation, the engraftment and the propagation of the tumor in the mice were
680 controlled at least twice weekly by palpation. When the tumor was palpable, the measurements
681 of tumor diameters were performed with a digital caliper twice weekly. Prior starting the
682 treatment, animals were randomly assigned into treatment and control groups (n=3). During
683 randomization, the animals were individually labeled by earmarks. Animals were treated i.t.

684 with MVdeltaC at doses 1 × 10^5 and 1 × 10^6 TCID50 per animal once weekly for up to 10
685 weeks. Virus was injected i.t. with three injections of 30-35µl at different sites in the tumor.
686 Animals from the control group received the vehicle also i.t. Tumor diameters were measured
687 three times weekly with a caliper. Tumor volumes were calculated according to V = (length ×
688 $(\text{width})^2$)/2. For calculation of the relative tumor volume (RTV) the volumes at each
689 measurement day are related to the day of first treatment. These RTV values were used for
690 the evaluation according to the modified RECIST criteria, with RTV values > 1.3 as Progression
691 (P), RTV between 0.7 and 1.3 as Stable Disease (SD), RTV < 0.7 as Partial Regression (PR)
692 and RTV = 0 as complete Regression (CR). At each measurement day, the median and mean
693 tumor volumes per group and the treated to control (T/C) values in percent were calculated.
694 The experiment was terminated when tumor volumes reached a weight of >10% of the animal's
695 normal body weight (typically a mean s.c. flank diameter of 17 mm or a tumor volume >1.5cm³
696 in a 25 g mouse). Body weight was determined 3 times weekly and all animals were checked
697 daily for treatment-related toxicity. The decrease in body weight provided a measure of
698 treatment-related toxicity.
699
700 **Syngeneic A/J mouse model.** Six- to 8-week-old female A/J mice were purchased from
701 Envigo (Inotiv). Animals were housed in the Institut Pasteur BIME A3 animal facility on a 12 h
702 light/dark cycle at 18–24°C and humidity of 40-60%. All the experiments were performed in
703 class III safety cabinets in the Institut Pasteur animal facilities accredited by the French Ministry
704 of Agriculture for performing experiments on live rodents. Animal experiments were validated
705 by Institut Pasteur ethics committee with the approval numbers: APAFIS #35041-
706 2022013107218823 v5, dap210133 and CHSCT 16-013. All animals were handled in strict
707 accordance with good animal practice.
708 *Tumor transplantations*. A total of 5 × 10^6 NS20Y cells in 100µL of PBS were injected
709 subcutaneously in the right shaved flank of the mice. Tumor sizes were monitored with a digital
710 caliper (Fisherbrand) every 2 to 3 days and tumor volume was calculated using formula V = L
711 x W^2 x 0.5, where V is the tumor volume, L is the tumor length, and W is the tumor width. Health

712 monitoring and humane endpoints were implemented using Institut Pasteur ethics committee
713 validated health evaluation scoring grid. Animals were killed when tumor volume exceeded
714 ≥1500mm^3, if the tumors developed hemorrhagic ulcers, if a body weight loss ≥20% occurred,
715 if mice showed bad general condition scores, or the purpose of the experiment has been
716 reached.
717 *Tumor immunotherapy treatment*. Treatments started on day 6 after tumor cell injection when
718 tumors reached 100-250mm^3 (7 to 10mm in largest diameter). Intratumoral injections of
719 MVdeltaC in 100µl volume were performed on days 6, 9 and 12 after NS20Y cells injection.
720 The 100µL dose of PBS or MVdeltaC was injected in one shot during the first treatment and
721 using the "radial technique" during next treatments. In "radial technique" a single-entry point in
722 the punctured tumor was performed to minimize discharge and bleeding. The needle was then
723 gently moved within the tumor mass to reach and inject different tumor parts. The immune
724 checkpoint-targeted antibody anti-CTLA-4 (clone 9H10, BioXCell) was injected systemically
725 via the intraperitoneal route at the concentration of 200µg in 100µl of PBS, four times on days
726 6, 9, 12, and 15 after NS20Y cells injection.
727 *CD4/CD8 T and NK cell depletions*. Anti-CD4 (rat IgG2b; clone GK1.5), anti-CD8a (rat IgG2b;
728 clone 2.43), and anti-CD20 (rat IgG2c; clone MB20-11) depleting mAbs were purchased from
729 BioXCell. NK cells depleting anti-asialo GM1 antibody (polyclonal rabbit anti-mouse IgG) was
730 purchased from Thermo Fisher. Depleting antibodies were injected intraperitoneally 1 day
731 before starting the intratumoral MVdeltaC therapy. To deplete T cells, anti-CD4 or anti-CD8
732 mAbs (200 µg in 100 µL of PBS) were injected intraperitoneally on days 5, 6 and 7 after NS20Y
733 cells injection. Targeted depletion of NK or B cell was performed on days 5 and 7 following
734 NS20Y tumor cell inoculation using 50µg of anti-asialo GM1 or 200µg of anti-CD20 antibodies,
735 respectively. Sustained immune cell depletion was achieved by weekly antibody
736 administrations starting from day 7 until day 49. Depletion efficacy was evaluated in blood
737 samples of selected mice by flow cytometry. *Flow cytometry.* Immune cell depletion efficacy
738 was evaluated in the blood from three mice of each group. Blood was collected in Microvette
739 500 EDTA K3E tubes (Sarstedt) by submandibular vein puncture. Cells in the blood samples

740 (200 µL) were sedimented by centrifugation, supernatant was discarded and red blood cells
741 were lysed using RBC lysis buffer (Sigma-Aldrich). Cells were washed with PBS 2% FBS buffer
742 and surface-stained with eBioscience CD3e (clone 145-2C11), CD4 (clone RM4- 5), CD8a
743 (clone 53-6.7), CD335 (NKp46, clone 29A1.4), and Biolegend CD19 (clone 6D5) specific
744 monoclonal antibodies. The stained cells were acquired on an Attune™ NxT Flow Cytometer
745 (Thermo Fischer).
746 *Ethics.* All animal experiments were performed according to French legislation in compliance
747 with the European Communities Council Directives (2010/63/UE, French Law 2013–118, 6
748 February 2013) and according to the regulations of Institut Pasteur Animal Care Committees.
749 The Animal Experimentation Ethics Committee (CETEA 89) of the Institut Pasteur approved
750 this study (dap210133) before experiments were initiated.
751 *Immunohistochemistry*. On day 13, tumors were harvested and fixed in 10% formol for 48h.
752 Tumors were photographed and embedded in the Optimal Cutting Temperature compound
753 (Tissue-Tek Sakura). Immunohistochemical analysis of spleen and tumor 8µm-thick cryostat
754 sections was performed on Leica Bond RX using rabbit anti-mouse CD4 (Cell signaling,
755 D7D2Z) or CD8a (Cell signaling, D4W2Z) monoclonal antibodies, followed by biotinylated goat
756 anti-rabbit secondary antibody (Dako) and streptavidin-HRP, provided in the Leica Bond RX
757 kit. Slides were scanned using an Axioscan Z1 Zeiss slide scanner and the images were
758 analyzed using Zen 3.8 software.
759
760 **Statistical analysis**
761 Analyses were performed with the GraphPad Prism software (versions 6 to 10, GraphPad
762 Software Inc., La Jolla, CA, USA). Unpaired, non-parametric, Mann-Whitney was used to
763 compare two independent groups. Unpaired, non-parametric, Kruskal-Wallis was used to
764 compare three or more independent groups. Differences were considered significant when *p
765 < 0.05, **$p < 0.01$ or ***$p < 0.001$. All data are from at least three independent experiments
766 and are presented as mean ± standard deviation (SD).

767 **DATA AVAILABILITY**

768 The authors declare that the data supporting the findings of this study are available within this
769 article and its supplementary information files or available from the corresponding author upon
770 reasonable request. The source data files are provided with this paper.

771

772 **ACKNOWLEDGMENTS**

773 This work was funded by Oncovita and by grants from the Agence Nationale de la Recherche
774 (ANR-16-CE18-0016), the Fondation pour la Recherche Médicale (Labellisation
775 DEQ20140329511) and La Ligue Contre le Cancer Grand Ouest. We thank the staff of the
776 animal facility of the Pasteur Institute for mouse care, and the Cytocell - Flow Cytometry and
777 FACS core facility (SFR Bonamy, BioCore, Inserm UMS 016, CNRS UAR 3556, Nantes,
778 France) for its technical expertise and help, member of the Scientific Interest Group (GIS)
779 Biogenouest and the Labex IGO program supported by the French National Research Agency
780 (n°ANR-11-LABX-0016-01). We acknowledge Philippe Hulin, Steven Nedellec and Stéphanie
781 Blandin from the MicroPICell core facility (SFR Bonamy, BioCore, Inserm UMS 016, CNRS
782 UAR 3556, Nantes, France), member of the Scientific Interest Group (GIS) Biogenouest,
783 IBISA, and the national infrastructure France-Bioimaging supported by the French National
784 Research Agency (ANR-24-INBS-0005 FBI BIOGEN). We acknowledge Elodie Turc and Laure
785 Lemée, Biomics Platform, C2RT, Institut Pasteur, Paris, France, supported by France
786 Génomique (ANR-10-INBS-09) and IBISA. We extend special thanks to Delphine Coulais and
787 Sylvia Lambot for their assistance regarding monocyte purification and animal experiments,
788 respectively.

789

790 **COMPETING INTEREST**.

791 AB, FT, HVP, VR are employees of Oncovita. FT and MG are cofounders of Oncovita. JFLB
792 is chairman of Oncovita. FT, MG, JFF, CC are inventors of the US patent N° 10,314,905 B2
793 and the EU patent N° EP2 948 157B1 (USE OF A GENETICALLY MODIFIED INFECTIOUS

794 MEASLES VIRUS WITH ENHANCED PRO-APOPTOTIC PROPERTIES (MV-DELTAC
795 VIRUS) IN CANCER THERAPY) granted for the treatment of aggressive solid tumors.
796

797 **FIGURE LEGENDS.**

798

799 **Figure 1. Characterization of MVdeltaC virus.** (a) Schematic of the measles viral particle,
800 genome and proteins: nucleoprotein (N), phosphoprotein (P), matrix (M), fusion (F),
801 hemagglutinin (H) and polymerase (L). ORFs for P, V, and C are enlarged. (b) Nucleotide
802 sequence of the P and C ORFs with the mutations (underlined) introduced in MVdeltaC to
803 disrupt C protein expression. (c) Expression of N and C proteins in lysates of Vero cells infected
804 by MV Schwarz or MVdeltaC, analysed by western blot. (d) Kinetics of N and V proteins
805 expression in Vero cell lysates after infection with MV Schwarz or MVdeltaC at MOI 1. (e)
806 Comparative growth kinetics of MV Schwarz (blue) and MVdeltaC (red) in different cell lines
807 infected at MOI 1 and cultured at 37°C. Viruses were harvested from cell lysates at the
808 indicated time points.

809

810 **Figure 2. MVdeltaC induces accelerated RIG-I-dependent innate immune activation and**
811 **killing of cancer cells.** (a) Viability of human cancer cell lines infected with MV (blue) or
812 MVdeltaC (red) at increasing MOIs, measured by CellTiter-Glo assay; data normalized to non-
813 infected cells; mean ± SD, n = 3. (b) NGS quantification of DVGs in HAP1 cells infected with
814 MV or MVdeltaC. Bars show total viral reads aligned to MV genome and DVG read counts as
815 detected by DI-tector; mean ± SD, n=3. (c) Innate immunity gene expression profiles in wild-
816 type and knockout HAP1 cells 24 h after infection with MV, MVdeltaC, or PBS (Mock). Heatmap
817 shows $\log_{10}$ fold changes of differentially expressed genes; experiment in triplicate, a gradient
818 of colors from green to red represent lowest to highest values, respectively, under all
819 conditions. (d) Viability of wild-type, RIG-I KO, MDA5 KO, and MAVS KO HAP1 cells 24 h after
820 infection with MV or MVdeltaC at MOI 1; means ± SD of three independent experiments; two-
821 way ANOVA test with Šídák's multiple comparisons test.

822

823 **Figure 3. MVdeltaC induces potent NS20Y neuroblastoma tumor rejection in**
824 **immunocompetent A/J mice.** (a) Schematic of the syngeneic NS20Y/AJ model and

825 MVdeltaC treatment schedule. (b) Left, representative tumors excised from the mice on day
826 13; right, immunofluorescence of tumor cryosections stained for measles nucleoprotein (MV-
827 N, red) and DNA (DAPI, blue). (c) Tumor growth kinetics (black lines, individual mice) and
828 survival after three i.t. injections of MVdeltaC (2×10^6 $TCID_{50}$) or PBS. Blue dotted line indicates
829 the day of tumor re-challenge; n = 10-11 mice per group; MVdeltaC group was compared to
830 PBS-treated group; unpaired one-tailed t test comparing the mean tumor sizes of each group;
831 log-rank test for survival. (d) Tumor growth kinetics after one (1x MVdeltaC, day 6), three (days
832 6, 9 and 12) or five (days 6, 9, 12, 15 and 19) i.t. injections of MVdeltaC; n = 10 mice per group;
833 each group was compared to PBS-treated group; unpaired one-tailed t test. (e) Kaplan–Meier
834 survival curves for the same groups; log-rank test. (f) Comparison of tumor control by
835 MVdeltaC (red) and parental MV (blue). Left, tumor growth calculated as the change in tumor
836 volume between treatment initiation (day 6) and study days 12, 16, or 19; unpaired two-tailed
837 t-test. Right, mean tumor volume ± SEM, n = 10 mice per group.
838
839 **Figure 4. MVdeltaC induces massive T cells infiltration into tumors, and rejection**
840 **efficacy relies on a functional immune system.** (a) Immunohistochemistry of NS20Y tumors
841 24 h after the third i.t. injection of MVdeltaC, stained for $CD4^+$ and $CD8^+$ T cells. (b) Tumor
842 growth and survival in mice depleted of $CD4^+$, $CD8^+$, B cells or NK cells during MVdeltaC
843 therapy. Depletion was maintained by weekly antibody administration until day 49. Tumor
844 therapy with MVdeltaC was performed on days 6, 9 and 12; *n* = 10 mice per group; each group
845 was compared to PBS-treated group; unpaired one-tailed t test; ns, not significant.
846
847 **Figure 5. MVdeltaC therapy is not affected by preexisting measles immunity, is**
848 **enhanced by anti-CTLA-4 therapy and exhibits abscopal effect.** (a) NS20Y tumor growth
849 in MV-naïve or measles pre-vaccinated mice treated i.t. with MVdeltaC or PBS on days 6, 9,
850 12 and 19 after tumor cells seeding. (b) Survival rates, and (c) percentage of tumor-free
851 animals in naïve or pre-vaccinated mice; *n* = 6-9 mice per group; each group was compared
852 to MV-naïve PBS-treated group, unpaired one-tailed t test; log-rank test for survival. (d) Tumor

853 growth in mice treated with three i.t. injections of MVdeltaC and/or four i.p. injections of anti-
854 CTLA-4 (αCTLA-4) antibody on days 6, 9, 12 and 15; n = 10-12 mice per group; each group
855 was compared to PBS group (unpaired one-tailed t test). (e) Growth of injected and
856 contralateral uninjected (distant) tumors in mice treated with MVdeltaC in single tumor; n = 12
857 mice per group; MVdeltaC-injected and distant tumors were compared to their corresponding
858 PBS controls; unpaired one-tailed t test.
859
860 **Figure 6. Oncolytic activity of MVdeltaC in human mesothelioma cells.** (a) Time-lapse
861 microscopy of healthy mesothelial (MES-F) and mesothelioma (Meso 4, Meso 11, Meso 13)
862 cells infected with MV-eGFP or MVdeltaC-eGFP at MOI 1. (b) Quantification of virus
863 propagation in normal mesothelial (LP-9) and mesothelioma (Meso 11, Meso 13) cells infected
864 with either MV-mCherry or MVdeltaC-mCherry. (c) Caspase-3/7 activation (NucView probe,
865 cyan) detected by fluorescent microscopy in mesothelioma cells infected with either MV-
866 mCherry or MVdeltaC-mCherry (red). (d) Caspase-3/7 activity measured by luminescence
867 (Caspase-3/7-Glo). Data are mean ± SD of at least three independent experiments.
868
869 **Figure 7. MVdeltaC induces danger signal production by tumor cells and promotes**
870 **dendritic cell maturation. (**a) Confocal microscopy of dsRNA (purple) in mesothelioma cells
871 infected for 48h with either MV-eGFP or MVdeltaC-eGFP (MOI = 1, green). DNA is labeled
872 with Hoechst (blue). (b) HMGB1 release in supernatants of healthy mesothelial MES-F cells
873 and mesothelioma cells measured by ELISA 72 h after infection with MV Schwarz or
874 MVdeltaC (MOI=1). Data represent means ± SD of three independent experiments. (c)
875 Comparison of HMGB1 release between the MV and MVdeltaC conditions for MV-sensitive
876 cell lines presented in (b); two-tailed Mann-Whitney test. (d-e) Immature human dendritic cells
877 (iDCs) cultured for 20h in presence of LPS (1µg/mL), MV Schwarz or MVdeltaC (2×10^5)
878 previously UV-inactivated or not, or Meso13 mesothelioma cells previously exposed to UV-B
879 (10J/cm²) or infected for 72h with MV Schwarz or MVdeltaC. HLA-DR$^+$ DCs were then

880 analyzed by flow cytometry for CD83 surface expression as shown for one experiment (d) or
881 for 6 independent experiments (e); Kruskal-Wallis test.
882
883 **Figure 8. MVdeltaC controls human tumor growth in immunodeficient mouse models.**
884 (a) Meso 163 (upper panel) and Meso 34 (lower panel) tumor weights in NOD/SCID mice two
885 weeks after single i.p. injection of MVdeltaC; means ± SD, n=7 - 10 mice per group; unpaired
886 two-tailed t test. (b) Representative images of Meso 34 tumor nodules from treated and control
887 animals. (c) Hematoxylin-phloxine-saffron staining of the peritoneum with detailed view of the
888 tumor area (right). (d) Human M6 melanoma tumor growth in NOD:SCID mice treated with two
889 i.t. injections of MVdeltaC on days 10 and 17; means ± SEM, n = 4 mice per group; one-tailed
890 t test. (e) Triple-negative breast cancer MDA-MB-231 tumor growth in NMRI nu/nu mice after
891 weekly i.t. injections of MVdeltaC. Therapy started on day 38, for a total of eight bi-weekly
892 injections; means ± SEM, n=6 mice per group; unpaired one-tailed t test. (f) mesothelioma
893 PDX tumor growth in NMRI nu/nu mice after weekly MVdeltaC therapy at two doses; means ±
894 SEM, n = 3 mice per group; each group was compared to PBS group (unpaired one-tailed t
895 test).
896
897 **Figure S1. Growth kinetics of MV and MVdeltaC on Vero cells.** Cells were infected at MOI
898 0.01 and incubated at 32°C. The data show reciprocal endpoint dilution titers of cell-associated
899 (left) and cell-free (right) viruses.
900
901 **Figure S2. Sequencing analysis of MVdeltaC passages.** Reads coverage and proportion of
902 intrasample single nucleotide variants (iSNVs) obtained from next-generation sequencing of
903 MVdeltaC at passages 5 (P5) and 10 (P10). A schematic of the measles virus genome is
904 shown below using the same scale, with the two engineered mutations preventing C protein
905 expression highlighted. No sequence changes were detected at either of these positions in P5
906 or P10 samples.

907

908 **Figure S3. Infection and killing of human cancer cells by MVdeltaC.** (a) Cell survival of
909 three human bladder cancer cell lines after infection with MV (blue) or MVdeltaC (red) at MOI
910 5, measured by CellTiter-Glo assay; means ± SD; measurements are in triplicate; data
911 normalized to non-infected cells. (b) MVdeltaC killing of a series of human cancer cells of
912 bladder, ovarian or hepatocellular origin as determined by CellTiterGlo assay (cancer cells
913 survival after 72 hours of infection at MOI 5).

914

915 **Figure S4. Gene expression analysis in infected MRC5 cells.** Heatmap of differentially
916 expressed genes in MRC5 cells after 24h incubation with MV, MVdeltaC (MOI 1) or PBS
917 (Mock); experiment in triplicate, a gradient of colors from green to red represent log_{10} fold
918 change values from lowest to highest, respectively.

919

920 **Figure S5. NS20Y cells are permissive to measles infection.** Mouse neuroblastoma NS20Y
921 cells and bladder carcinoma MB49 cells were infected with MV-eGFP at the indicated MOI and
922 analyzed by (a) flow cytometry 24 hours post-infection, and (b) immunofluorescence
923 microscopy 72 h hours post-infection.

924

925 **Figure S6. Flow cytometry analysis of immune cell populations in the blood of A/J mice**
926 **depleted for $CD4^+$, $CD8^+$, B or NK cells.** (a) Representative dot plots show the flow cytometry
927 gating strategy to identify $CD4^+$ ($CD3^+$ $CD4^+$ $CD8^-$), $CD8^+$ ($CD3^+$ $CD8^+$ $CD4^-$) or (b) NK ($CD3^-$
928 $NKp46^+$ $CD19^-$) and B ($CD3^-$ $CD19^+$) cell populations in the blood of treated mice. Mice were
929 grafted with $5x10^6$ NS20Y murine tumor cells on day 0. T cell depletion was achieved by i.p.
930 injection of anti-CD4 or anti-CD8 mAbs (200 µg in 100 µL of PBS) on days 5, 6 and 7 after
931 NS20Y cells injection. NK or B cell depletion was performed on days 5 and 7 using 50µg of

932 anti-asialo GM1 or 200µg of anti-CD20 antibodies, respectively. Sustained immune cell
933 depletion was achieved by weekly antibody administrations on days 14 and 21. Tumor therapy
934 with MVdeltaC at $2x10^6 TCID_{50}$ was performed on days 6, 9 and 12. Immune cell populations
935 in the groups of A/J mice were analyzed on day 27. (c) Bar graphs show flow cytometry data
936 for the three animals from each group, means ± SD.

937

938 **Figure S7. MV-specific IgG antibody responses in A/J mice following MV Schwarz**
939 **vaccination.** Mice were immunized i.p. with MV Schwarz (1×10^5 $TCID_{50}$) on day 0. Sera were
940 collected at day 38 post-immunization and assessed for IgG antibody responses to MV
941 antigens by ELISA. The data show the reciprocal endpoint dilution titers of MV-specific IgG
942 antibodies in preimmune (day 0) and day 38 sera; each point represents an individual mouse;
943 means ± SD, n= 7-9 per group; unpaired two-tailed t test; ns, not significant.

944

945 **Figure S8. Infection of healthy and cancer human cells by MV or MVdeltaC.** (a)
946 Quantification of virus propagation in healthy lung fibroblasts (CCD19-Lu) or endothelial cells
947 (HUVECs) infected with either MV-mCherry or MVdeltaC-mCherry. (b) Time-lapse microscopy
948 analysis of mesothelioma cell lines infected with MV-eGFP or MVdeltaC-eGFP (MOI = 1).

949

950 **Figure S9. Infection of Meso 13 mesothelioma cells by MV or MVdeltaC.**

951 Time-lapse microscopy analysis of mesothelioma cell lines infected with MV-eGFP (a) or
952 MVdeltaC-eGFP (b) (MOI = 1).

953

954 **Figure S10. Activation of Caspases-3/7 in mesothelioma cells infected by MVdeltaC.** (a-
955 c) Luminescence-based quantification of caspase-3/7 activity in human mesothelioma cell
956 lines. (a) MV-permissive, (b) MVdeltaC-resistant, and (c) MV-resistant cells. (d) Fluorescence

957 microscopy of Meso 4 cells showing caspase-3/7 activation (cyan) after infection with MV-
958 mCherry or MVdeltaC-mCherry (red).

959

960 **Figure S11. MVdeltaC inhibits human PDX growth in immunodeficient mice**. Growth of
961 mesothelioma PDX tumors in NMRI nu/nu mice after weekly MVdeltaC therapy at two doses;
962 means ± SEM, n = 3 mice per group; each group was compared to PBS group (unpaired one-
963 tailed t test).

964

965

REFERENCES

1 Alsaab, H. O. *et al.* PD-1 and PD-L1 Checkpoint Signaling Inhibition for Cancer Immunotherapy: Mechanism, Combinations, and Clinical Outcome. *Front Pharmacol* **8**, 561 (2017). https://doi.org:10.3389/fphar.2017.00561

2 Wu, B., Zhang, B., Li, B., Wu, H. & Jiang, M. Cold and hot tumors: from molecular mechanisms to targeted therapy. *Signal Transduct Target Ther* **9**, 274 (2024). https://doi.org:10.1038/s41392-024-01979-x

3 Yin, Q. *et al.* Immune-related adverse events of immune checkpoint inhibitors: a review. *Front Immunol* **14**, 1167975 (2023). https://doi.org:10.3389/fimmu.2023.1167975

4 Pol, J., Kroemer, G. & Galluzzi, L. First oncolytic virus approved for melanoma immunotherapy. *Oncoimmunology* **5**, e1115641 (2016). https://doi.org:10.1080/2162402X.2015.1115641

5 Todo, T. *et al.* Intratumoral oncolytic herpes virus G47Δ for residual or recurrent glioblastoma: a phase 2 trial. *Nat Med* **28**, 1630-1639 (2022). https://doi.org:10.1038/s41591-022-01897-x

6 Colbert, L. *et al.* FDA Approval Summary: Nadofaragene Firadenovec-vncg for Bacillus Calmette-Guerin-Unresponsive Non-Muscle-Invasive Bladder Cancer. *Clin Cancer Res* **31**, 1182-1185 (2025). https://doi.org:10.1158/1078-0432.CCR-24-2812

7 Mullard, A. Oncolytic virus drought continues, as Replimune fails to secure FDA cancer approval. *Nat Rev Drug Discov* **24**, 654 (2025). https://doi.org:10.1038/d41573-025-00132-9

8 Chen, M. *et al.* Targeting nuclear acid-mediated immunity in cancer immune checkpoint inhibitor therapies. *Signal Transduct Target Ther* **5**, 270 (2020). https://doi.org:10.1038/s41392-020-00347-9

9 Mura, M. *et al.* Nonencapsidated 5' Copy-Back Defective Interfering Genomes Produced by Recombinant Measles Viruses Are Recognized by RIG-I and LGP2 but Not MDA5. *J Virol* **91** (2017). https://doi.org:10.1128/JVI.00643-17

10 Yoneyama, M., Kato, H. & Fujita, T. Physiological functions of RIG-I-like receptors. *Immunity* **57**, 731-751 (2024). https://doi.org:10.1016/j.immuni.2024.03.003

11 Sanchez David, R. Y. *et al.* Comparative analysis of viral RNA signatures on different RIG-I-like receptors. *Elife* **5**, e11275 (2016). https://doi.org:10.7554/eLife.11275

12 Jin, R., Cao, X., Lu, M., Gao, Q. & Ma, T. The intersection molecule MDA5 in Cancer and COVID-19. *Front Immunol* **13**, 963051 (2022). https://doi.org:10.3389/fimmu.2022.963051

13 Shekarian, T. *et al.* Repurposing rotavirus vaccines for intratumoral immunotherapy can overcome resistance to immune checkpoint blockade. *Sci Transl Med* **11** (2019). https://doi.org:10.1126/scitranslmed.aat5025

14 Jiang, Y. *et al.* Exploiting RIG-I-like receptor pathway for cancer immunotherapy. *J Hematol Oncol* **16**, 8 (2023). https://doi.org:10.1186/s13045-023-01405-9

15 Msaouel, P. *et al.* Clinical Trials with Oncolytic Measles Virus: Current Status and Future Prospects. *Curr Cancer Drug Targets* **18**, 177-187 (2018). https://doi.org:10.2174/1568009617666170222125035

16 Achard, C. *et al.* Sensitivity of human pleural mesothelioma to oncolytic measles virus depends on defects of the type I interferon response. *Oncotarget* **6**, 44892-44904 (2015). https://doi.org:10.18632/oncotarget.6285

17 Delaunay, T. *et al.* Frequent Homozygous Deletions of Type I Interferon Genes in Pleural Mesothelioma Confer Sensitivity to Oncolytic Measles Virus. *J Thorac Oncol* **15**, 827-842 (2020). https://doi.org:10.1016/j.jtho.2019.12.128

18 Allagui, F. *et al.* Modulation of the Type I Interferon Response Defines the Sensitivity of Human Melanoma Cells to Oncolytic Measles Virus. *Curr Gene Ther* **16**, 419-428 (2017). https://doi.org:10.2174/1566523217666170102110502

1014 19 Boisgerault, N. *et al.* Natural oncolytic activity of live-attenuated measles virus against human
1015 lung and colorectal adenocarcinomas. *Biomed Res Int* **2013**, 387362 (2013).
1016 https://doi.org:10.1155/2013/387362
1017 20 Gauvrit, A. *et al.* Measles virus induces oncolysis of mesothelioma cells and allows dendritic
1018 cells to cross-prime tumor-specific CD8 response. *Cancer Res* **68**, 4882-4892 (2008).
1019 https://doi.org:10.1158/0008-5472.CAN-07-6265
1020 21 Donnelly, O. G. *et al.* Measles virus causes immunogenic cell death in human melanoma. *Gene*
1021 *Ther* **20**, 7-15 (2013). https://doi.org:10.1038/gt.2011.205
1022 22 Guillerme, J. B. *et al.* Measles virus vaccine-infected tumor cells induce tumor antigen cross-
1023 presentation by human plasmacytoid dendritic cells. *Clin Cancer Res* **19**, 1147-1158 (2013).
1024 https://doi.org:10.1158/1078-0432.CCR-12-2733
1025 23 Achard, C. *et al.* Oncolytic measles virus induces tumor necrosis factor-related apoptosis-
1026 inducing ligand (TRAIL)-mediated cytotoxicity by human myeloid and plasmacytoid dendritic
1027 cells. *Oncoimmunology* **6**, e1261240 (2017). https://doi.org:10.1080/2162402X.2016.1261240
1028 24 Pfaller, C. K. *et al.* The C Protein Is Recruited to Measles Virus Ribonucleocapsids by the
1029 Phosphoprotein. *J Virol* **94** (2020). https://doi.org:10.1128/JVI.01733-19
1030 25 McAllister, C. S. *et al.* Mechanisms of protein kinase PKR-mediated amplification of beta
1031 interferon induction by C protein-deficient measles virus. *J Virol* **84**, 380-386 (2010).
1032 https://doi.org:10.1128/JVI.02630-08
1033 26 Sparrer, K. M., Pfaller, C. K. & Conzelmann, K. K. Measles virus C protein interferes with Beta
1034 interferon transcription in the nucleus. *J Virol* **86**, 796-805 (2012).
1035 https://doi.org:10.1128/JVI.05899-11
1036 27 Shaffer, J. A., Bellini, W. J. & Rota, P. A. The C protein of measles virus inhibits the type I
1037 interferon response. *Virology* **315**, 389-397 (2003). https://doi.org:10.1016/s0042-
1038 6822(03)00537-3
1039 28 Pfaller, C. K. *et al.* Measles Virus Defective Interfering RNAs Are Generated Frequently and
1040 Early in the Absence of C Protein and Can Be Destabilized by Adenosine Deaminase Acting on
1041 RNA-1-Like Hypermutations. *J Virol* **89**, 7735-7747 (2015). https://doi.org:10.1128/JVI.01017-
1042 15
1043 29 Pfaller, C. K., Radeke, M. J., Cattaneo, R. & Samuel, C. E. Measles virus C protein impairs
1044 production of defective copyback double-stranded viral RNA and activation of protein kinase
1045 R. *J Virol* **88**, 456-468 (2014). https://doi.org:10.1128/JVI.02572-13
1046 30 Vignuzzi, M. & Lopez, C. B. Defective viral genomes are key drivers of the virus-host interaction.
1047 *Nat Microbiol* **4**, 1075-1087 (2019). https://doi.org:10.1038/s41564-019-0465-y
1048 31 Richetta, C. *et al.* Sustained autophagy contributes to measles virus infectivity. *PLoS Pathog* **9**,
1049 e1003599 (2013). https://doi.org:10.1371/journal.ppat.1003599
1050 32 Combredet, C. *et al.* A molecularly cloned Schwarz strain of measles virus vaccine induces
1051 strong immune responses in macaques and transgenic mice. *J Virol* **77**, 11546-11554 (2003).
1052 https://doi.org:10.1128/jvi.77.21.11546-11554.2003
1053 33 Amurri, L., Reynard, O., Gerlier, D., Horvat, B. & Iampietro, M. Measles Virus-Induced Host
1054 Immunity and Mechanisms of Viral Evasion. *Viruses* **14** (2022).
1055 https://doi.org:10.3390/v14122641
1056 34 Brennan, J. W. & Sun, Y. Defective viral genomes: advances in understanding their generation,
1057 function, and impact on infection outcomes. *mBio* **15**, e0069224 (2024).
1058 https://doi.org:10.1128/mbio.00692-24
1059 35 Beauclair, G. *et al.* DI-tector: defective interfering viral genomes' detector for next-generation
1060 sequencing data. *RNA* **24**, 1285-1296 (2018). https://doi.org:10.1261/rna.066910.118
1061 36 Schattner, A., Rager-Zisman, B. & Bloom, B. R. Persistent viral infection affects tumorigenicity
1062 of a neuroblastoma cell line. *Cell Immunol* **90**, 103-114 (1985). https://doi.org:10.1016/0008-
1063 8749(85)90173-x

37 Tentler, J. J. *et al.* Patient-derived tumour xenografts as models for oncology drug development. *Nat Rev Clin Oncol* **9**, 338-350 (2012). https://doi.org:10.1038/nrclinonc.2012.61
38 Becker, M. *et al.* Preclinical models from rare aggressive tumors: Establishment, drug sensitivity and genomic analyses of mesothelioma PDX as models for oncology drug development. *Mol Cancer Ther* **18** (2019). https://doi.org:10.1158/1535-7163.Targ-19-A006
39 Golfier, S. *et al.* Anetumab ravtansine: a novel mesothelin-targeting antibody-drug conjugate cures tumors with heterogeneous target expression favored by bystander effect. *Mol Cancer Ther* **13**, 1537-1548 (2014). https://doi.org:10.1158/1535-7163.MCT-13-0926
40 Eisenhauer, E. A. *et al.* New response evaluation criteria in solid tumours: revised RECIST guideline (version 1.1). *Eur J Cancer* **45**, 228-247 (2009). https://doi.org:10.1016/j.ejca.2008.10.026
41 Fonteneau, J.-F., Boisgerault, N. & Tangy, F. L'immuno-virothérapie antitumorale par les souches atténuées du virus de la rougeole. *Virologie* **29**, 271-291 (2025). https://doi.org:10.1684/vir.2025.1101
42 Engeland, C. E. *et al.* CTLA-4 and PD-L1 checkpoint blockade enhances oncolytic measles virus therapy. *Mol Ther* **22**, 1949-1959 (2014). https://doi.org:10.1038/mt.2014.160
43 Grossardt, C. *et al.* Granulocyte-macrophage colony-stimulating factor-armed oncolytic measles virus is an effective therapeutic cancer vaccine. *Hum Gene Ther* **24**, 644-654 (2013). https://doi.org:10.1089/hum.2012.205
44 Jing, Y., Zaias, J., Duncan, R., Russell, S. J. & Merchan, J. R. In vivo safety, biodistribution and antitumor effects of uPAR retargeted oncolytic measles virus in syngeneic cancer models. *Gene Ther* **21**, 289-297 (2014). https://doi.org:10.1038/gt.2013.84
45 Veinalde, R. *et al.* Oncolytic measles virus encoding interleukin-12 mediates potent antitumor effects through T cell activation. *Oncoimmunology* **6**, e1285992 (2017). https://doi.org:10.1080/2162402X.2017.1285992
46 Besch, R. *et al.* Proapoptotic signaling induced by RIG-I and MDA-5 results in type I interferon-independent apoptosis in human melanoma cells. *J Clin Invest* **119**, 2399-2411 (2009). https://doi.org:10.1172/JCI37155
47 Such, L. *et al.* Targeting the innate immunoreceptor RIG-I overcomes melanoma-intrinsic resistance to T cell immunotherapy. *J Clin Invest* **130**, 4266-4281 (2020). https://doi.org:10.1172/JCI131572
48 Heidegger, S. *et al.* RIG-I activation is critical for responsiveness to checkpoint blockade. *Sci Immunol* **4** (2019). https://doi.org:10.1126/sciimmunol.aau8943
49 Das, M., Shen, L., Liu, Q., Goodwin, T. J. & Huang, L. Nanoparticle Delivery of RIG-I Agonist Enables Effective and Safe Adjuvant Therapy in Pancreatic Cancer. *Mol Ther* **27**, 507-517 (2019). https://doi.org:10.1016/j.ymthe.2018.11.012
50 Wu, Y., Wu, X., Wu, L., Wang, X. & Liu, Z. The anticancer functions of RIG-I-like receptors, RIG-I and MDA5, and their applications in cancer therapy. *Transl Res* **190**, 51-60 (2017). https://doi.org:10.1016/j.trsl.2017.08.004
51 Canadas, I. *et al.* Tumor innate immunity primed by specific interferon-stimulated endogenous retroviruses. *Nat Med* **24**, 1143-1150 (2018). https://doi.org:10.1038/s41591-018-0116-5
52 Ye, Z. *et al.* Prevalent Homozygous Deletions of Type I Interferon and Defensin Genes in Human Cancers Associate with Immunotherapy Resistance. *Clin Cancer Res* **24**, 3299-3308 (2018). https://doi.org:10.1158/1078-0432.CCR-17-3008
53 Barriga, F. M. *et al.* MACHETE identifies interferon-encompassing chromosome 9p21.3 deletions as mediators of immune evasion and metastasis. *Nat Cancer* **3**, 1367-1385 (2022). https://doi.org:10.1038/s43018-022-00443-5
54 Iurescia, S., Fioretti, D. & Rinaldi, M. Targeting Cytosolic Nucleic Acid-Sensing Pathways for Cancer Immunotherapies. *Front Immunol* **9**, 711 (2018). https://doi.org:10.3389/fimmu.2018.00711

55 Marabelle, A., Tselikas, L., de Baere, T. & Houot, R. Intratumoral immunotherapy: using the tumor as the remedy. *Ann Oncol* **28**, xii33-xii43 (2017). https://doi.org:10.1093/annonc/mdx683

56 Kärber, G. Beitrag zur kollektiven Behandlung pharmakologischer Reihenversuche. *Naunyn-Schmiedebergs Archiv für experimentelle Pathologie und Pharmakologie* **162**, 480-483 (1931). https://doi.org:10.1007/BF01863914

57 Bolger, A. M., Lohse, M. & Usadel, B. Trimmomatic: a flexible trimmer for Illumina sequence data. *Bioinformatics* **30**, 2114-2120 (2014). https://doi.org:10.1093/bioinformatics/btu170

58 Li, D. *et al.* MEGAHIT v1.0: A fast and scalable metagenome assembler driven by advanced methodologies and community practices. *Methods* **102**, 3-11 (2016). https://doi.org:10.1016/j.ymeth.2016.02.020

59 Grubaugh, N. D. *et al.* An amplicon-based sequencing framework for accurately measuring intrahost virus diversity using PrimalSeq and iVar. *Genome Biol* **20**, 8 (2019). https://doi.org:10.1186/s13059-018-1618-7

60 Gueugnon, F. *et al.* Identification of novel markers for the diagnosis of malignant pleural mesothelioma. *Am J Pathol* **178**, 1033-1042 (2011). https://doi.org:10.1016/j.ajpath.2010.12.014

61 Schindelin, J. *et al.* Fiji: an open-source platform for biological-image analysis. *Nat Methods* **9**, 676-682 (2012). https://doi.org:10.1038/nmeth.2019

FIGURE 1

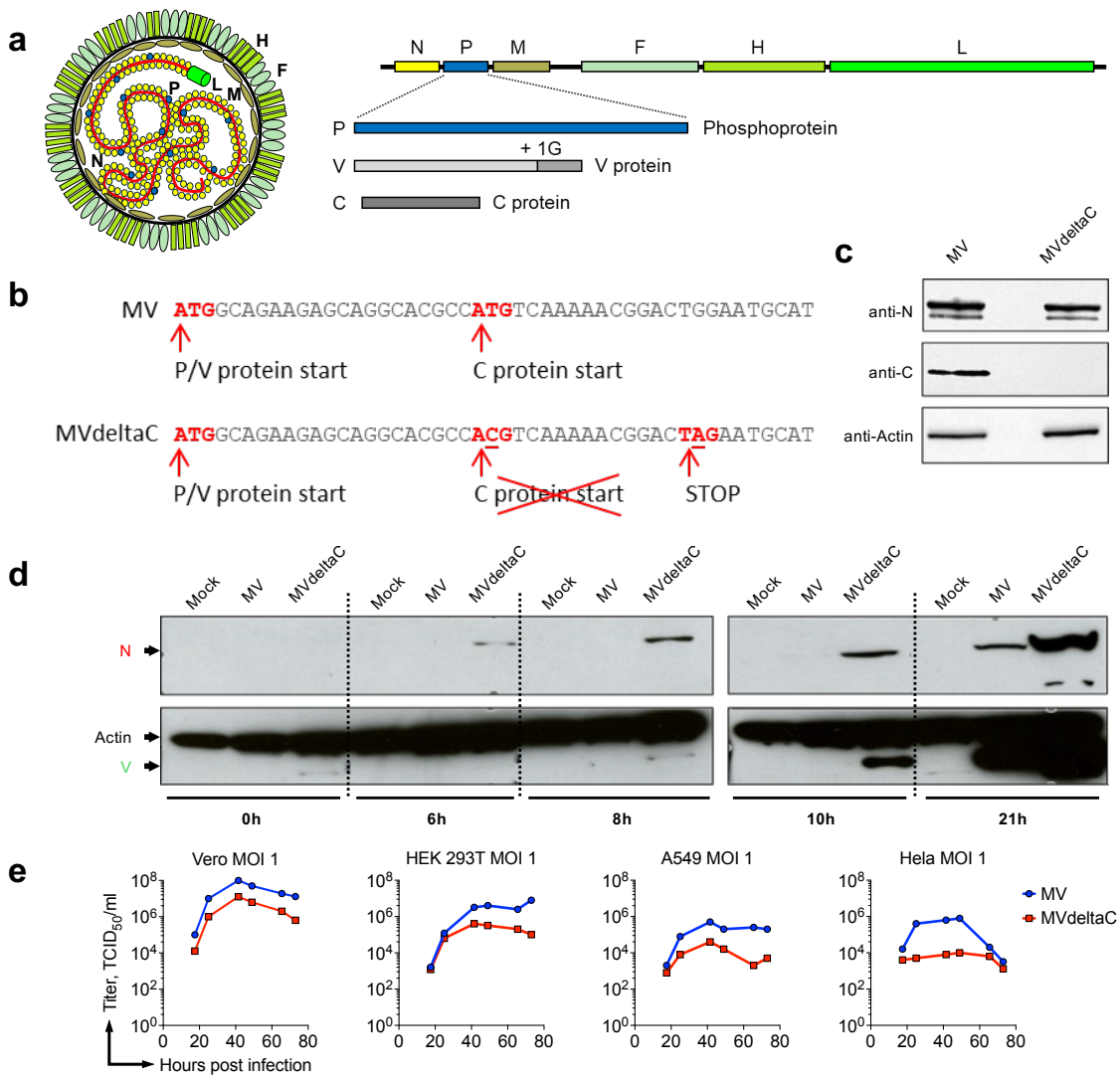

Figure 1. Characterization of MVdeltaC virus. (a) Schematic of the measles viral particle, genome and proteins: nucleoprotein (N), phosphoprotein (P), matrix (M), fusion (F), hemagglutinin (H) and polymerase (L). ORFs for P, V, and C are enlarged. (b) Nucleotide sequence of the P and C ORFs with the mutations (underlined) introduced in MVdeltaC to disrupt C protein expression. (c) Expression of N and C proteins in lysates of Vero cells infected by MV Schwarz or MVdeltaC, analysed by western blot. (d) Kinetics of N and V proteins expression in Vero cell lysates after infection with MV Schwarz or MVdeltaC at MOI 1. (e) Comparative growth kinetics of MV Schwarz (blue) and MVdeltaC (red) in different cell lines infected at MOI 1 and cultured at 37° C. Viruses were harvested from cell lysates at the indicated time points.

FIGURE 2

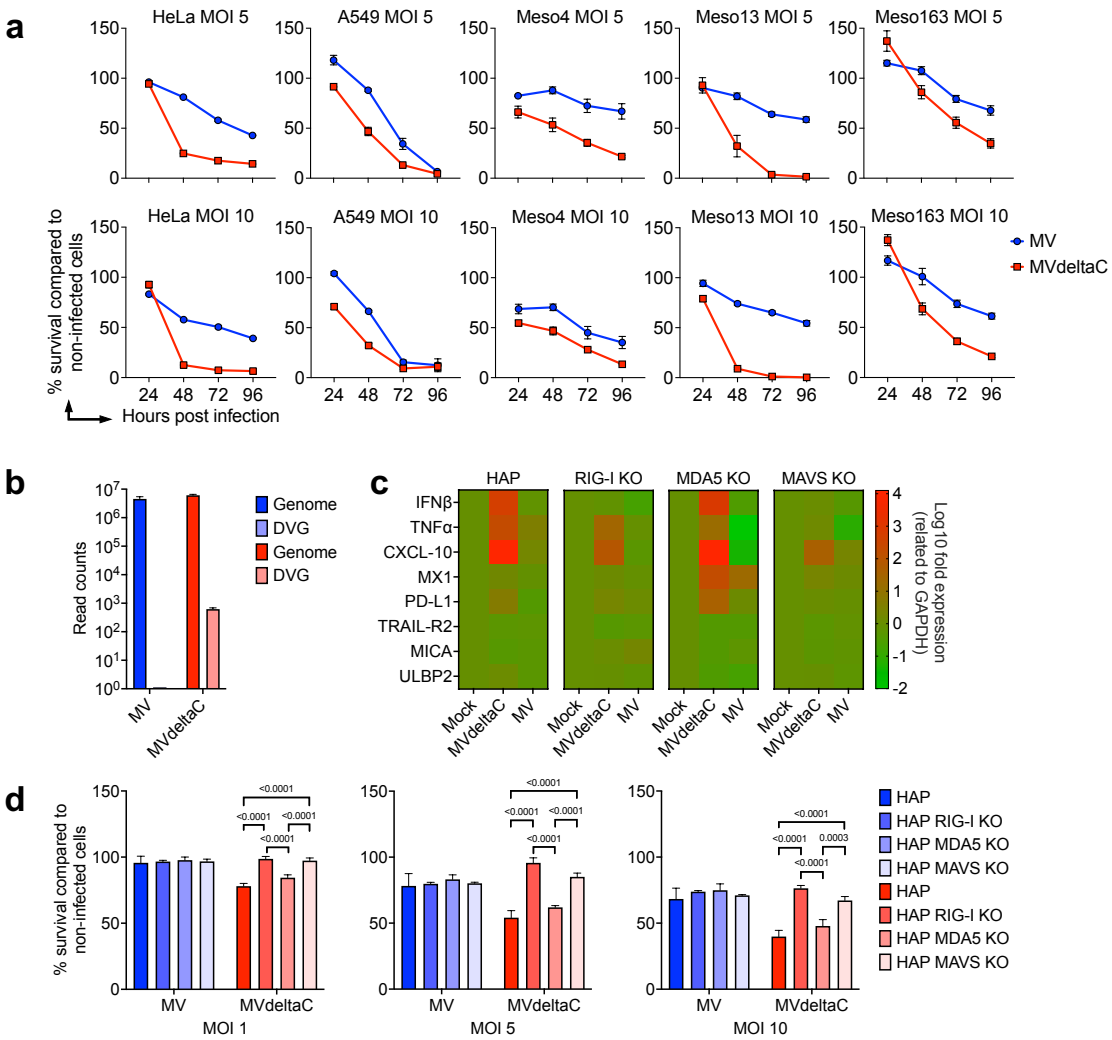

Figure 2. MVdeltaC induces accelerated RIG-I-dependent innate immune activation and killing of cancer cells. (a) Viability of human cancer cell lines infected with MV (blue) or MVdeltaC (red) at increasing MOIs, measured by CellTiter-Glo assay; data normalized to non-infected cells; mean ± SD, n = 3. (b) NGS quantification of DVGs in HAP1 cells infected with MV or MVdeltaC. Bars show total viral reads aligned to MV genome and DVG read counts as detected by DI-tector; mean ± SD, n=3. (c) Innate immunity gene expression profiles in wild-type and knockout HAP1 cells 24 h after infection with MV, MVdeltaC, or PBS (Mock). Heatmap shows $\log_{10}$ fold changes of differentially expressed genes; experiment in triplicate, a gradient of colors from green to red represent lowest to highest values, respectively, under all conditions. (d) Viability of wild-type, RIG-I KO, MDA5 KO, and MAVS KO HAP1 cells 24 h after infection with MV or MVdeltaC at MOI 1; means ± SD of three independent experiments; two-way ANOVA test with Šídák's multiple comparisons test.

FIGURE 3

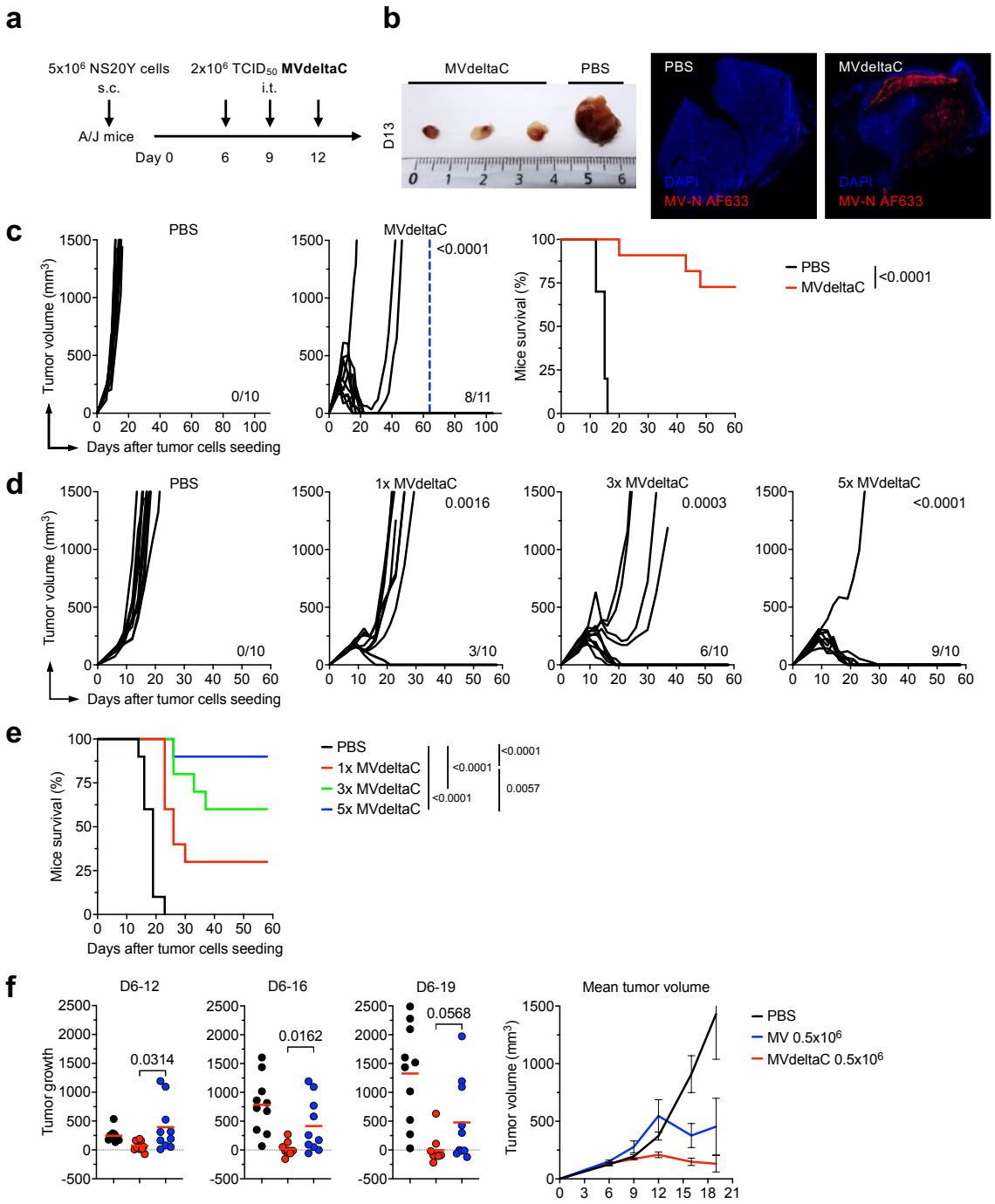

Figure 3. MVdeltaC induces potent NS20Y neuroblastoma tumor rejection in immunocompetent A/J mice. (a) Schematic of the syngeneic NS20Y/AJ model and MVdeltaC treatment schedule. (b) Left, representative tumors excised from the mice on day 13; right, immunofluorescence of tumor cryosections stained for measles nucleoprotein (MV-N, red) and DNA (DAPI, blue). (c) Tumor growth kinetics (black lines, individual mice) and survival after three i.t. injections of MVdeltaC (2×10^6 $TCID_{50}$) or PBS. Blue dotted line indicates the day of tumor re-challenge; n = 10-11 mice per group; MVdeltaC group was compared to PBS-treated group; unpaired one-tailed t test comparing the mean tumor sizes of each group; log-rank test for survival. (d) Tumor growth kinetics after one (1x MVdeltaC, day 6), three (days 6, 9 and 12) or five (days 6, 9, 12, 15 and 19) i.t. injections of MVdeltaC; n = 10 mice per group; each group was compared to PBS-treated group; unpaired one-tailed t test. (e) Kaplan–Meier survival curves for the same groups; log-rank test. (f) Comparison of tumor control by MVdeltaC (red) and parental MV (blue). Left, tumor growth calculated as the change in tumor volume between treatment initiation (day 6) and study days 12, 16, or 19; unpaired two-tailed t-test. Right, mean tumor volume ± SEM, n = 10 mice per group.

FIGURE 4

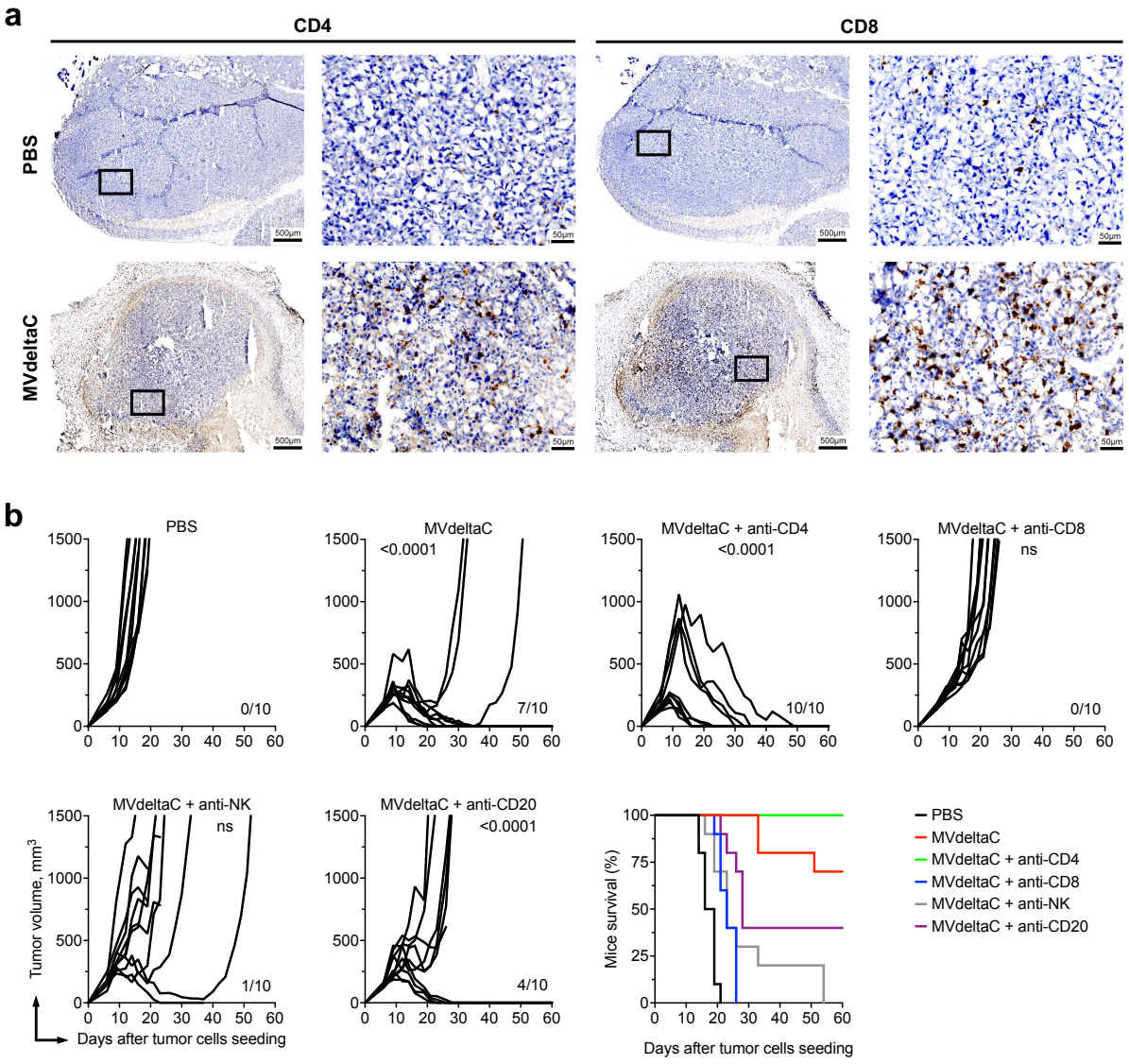

Figure 4. MVdeltaC induces massive T cells infiltration into tumors, and rejection efficacy relies on a functional immune system. (a) Immunohistochemistry of NS20Y tumors 24 h after the third i.t. injection of MVdeltaC, stained for $CD4^+$ and $CD8^+$ T cells. (b) Tumor growth and survival in mice depleted of $CD4^+$, $CD8^+$, B cells or NK cells during MVdeltaC therapy. Depletion was maintained by weekly antibody administration until day 49. Tumor therapy with MVdeltaC was performed on days 6, 9 and 12; n = 10 mice per group; each group was compared to PBS-treated group; unpaired one-tailed t test; ns, not significant.

FIGURE 5

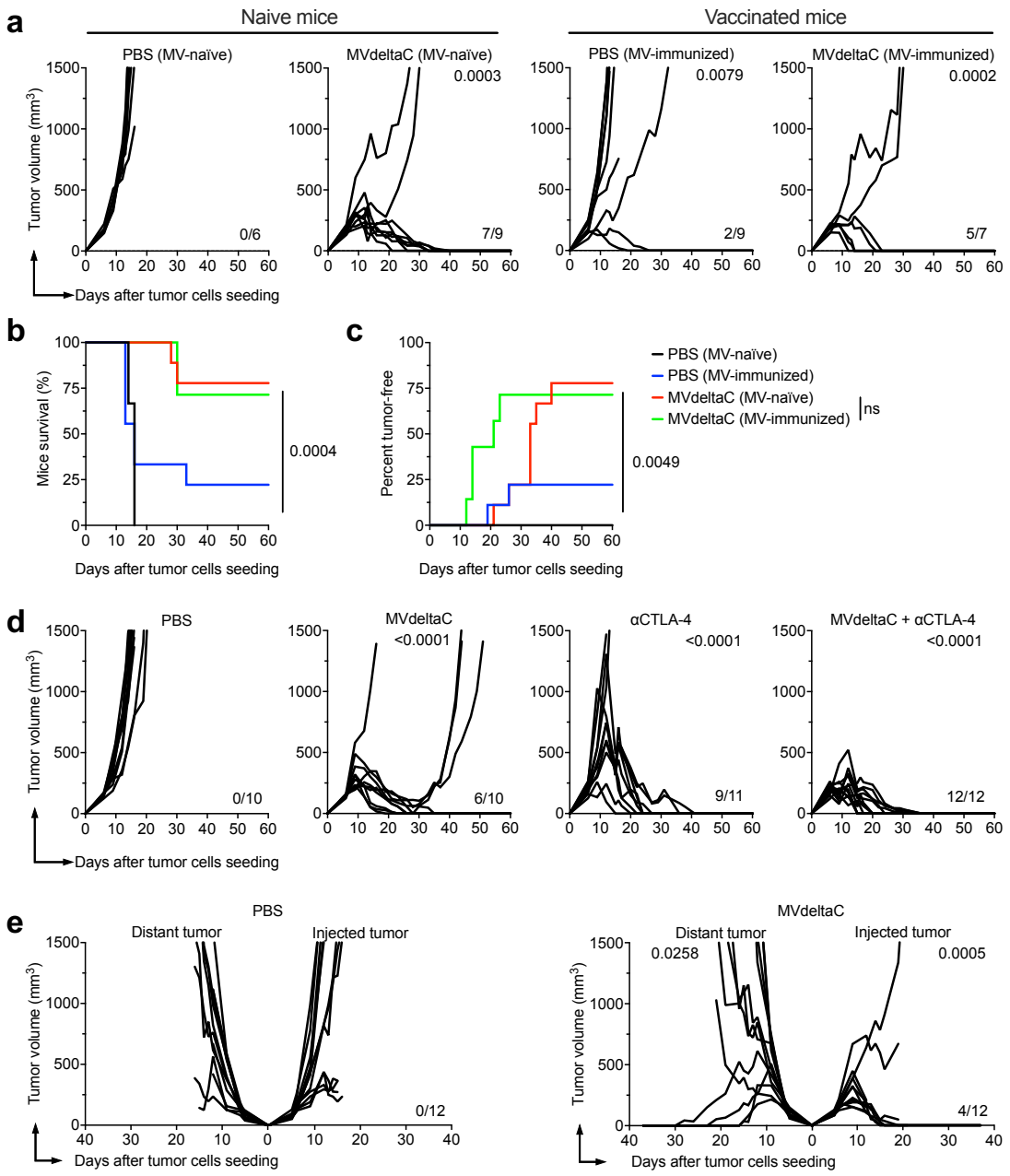

Figure 5. MVdeltaC therapy is not affected by preexisting measles immunity, is enhanced by anti-CTLA-4 therapy and exhibits abscopal effect. (a) NS20Y tumor growth in MV-naïve or measles pre-vaccinated mice treated i.t. with MVdeltaC or PBS on days 6, 9, 12 and 19 after tumor cells seeding. (b) Survival rates, and (c) percentage of tumor-free animals in naïve or pre-vaccinated mice; *n* = 6-9 mice per group; each group was compared to MV-naïve PBS-treated group, unpaired one-tailed t test; log-rank test for survival. (d) Tumor growth in mice treated with three i.t. injections of MVdeltaC and/or four i.p. injections of anti-CTLA-4 (αCTLA-4) antibody on days 6, 9, 12 and 15; n = 10-12 mice per group; each group was compared to PBS group (unpaired one-tailed t test). (e) Growth of injected and contralateral uninjected (distant) tumors in mice treated with MVdeltaC in single tumor; n = 12 mice per group; MVdeltaC-injected and distant tumors were compared to their corresponding PBS controls; unpaired one-tailed t test.

FIGURE 6

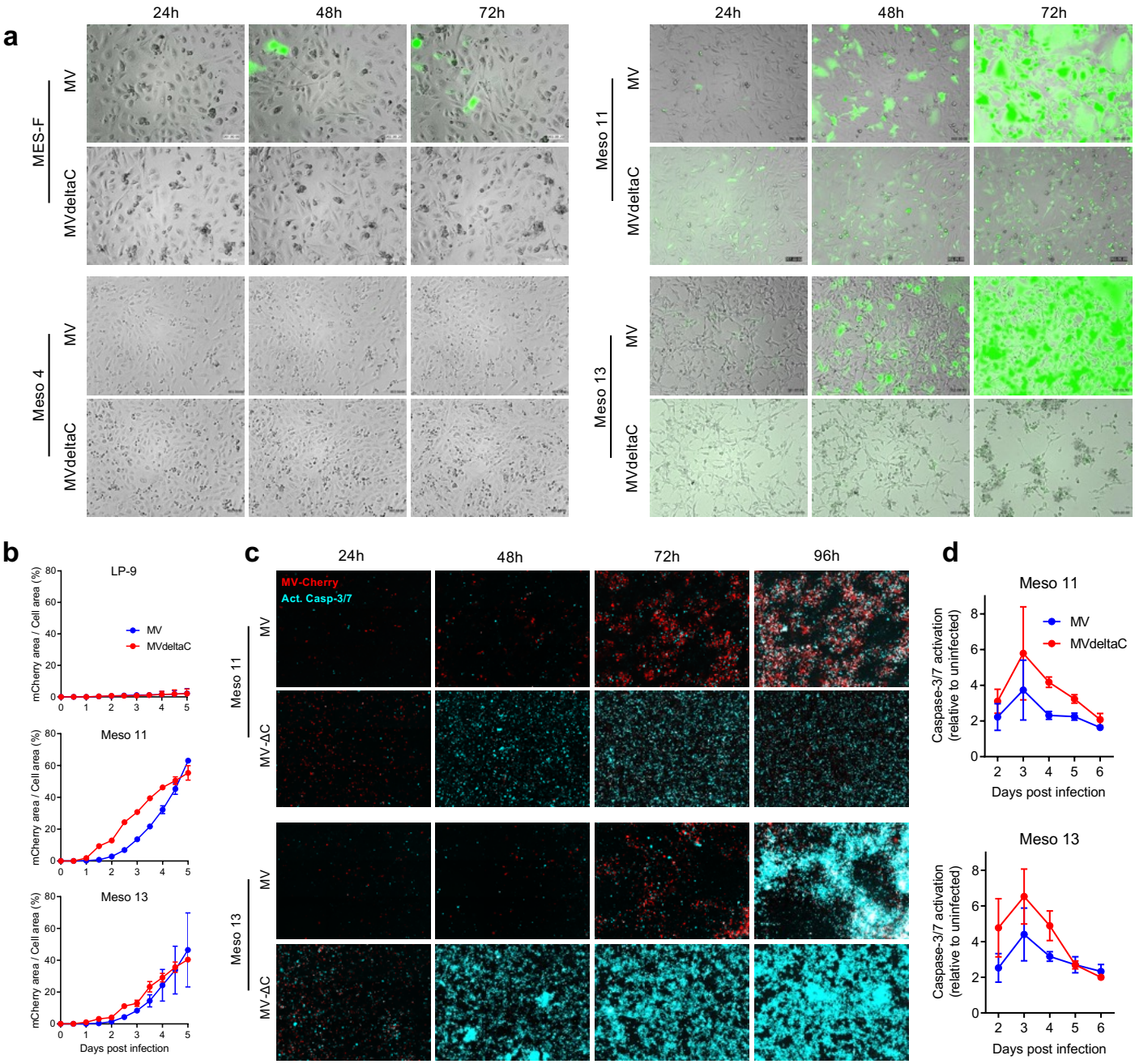

Figure 6. Oncolytic activity of MVdeltaC in human mesothelioma cells. (a) Time-lapse microscopy of healthy mesothelial (MES-F) and mesothelioma (Meso 4, Meso 11, Meso 13) cells infected with MV-eGFP or MVdeltaC-eGFP at MOI 1. (b) Quantification of virus propagation in normal mesothelial (LP-9) and mesothelioma (Meso 11, Meso 13) cells infected with either MV-mCherry or MVdeltaC-mCherry. (c) Caspase-3/7 activation (NucView probe, cyan) detected by fluorescent microscopy in mesothelioma cells infected with either MV-mCherry or MVdeltaC-mCherry (red). (d) Caspase-3/7 activity measured by luminescence (Caspase-3/7-Glo). Data are mean ± SD of at least three independent experiments.

FIGURE 7

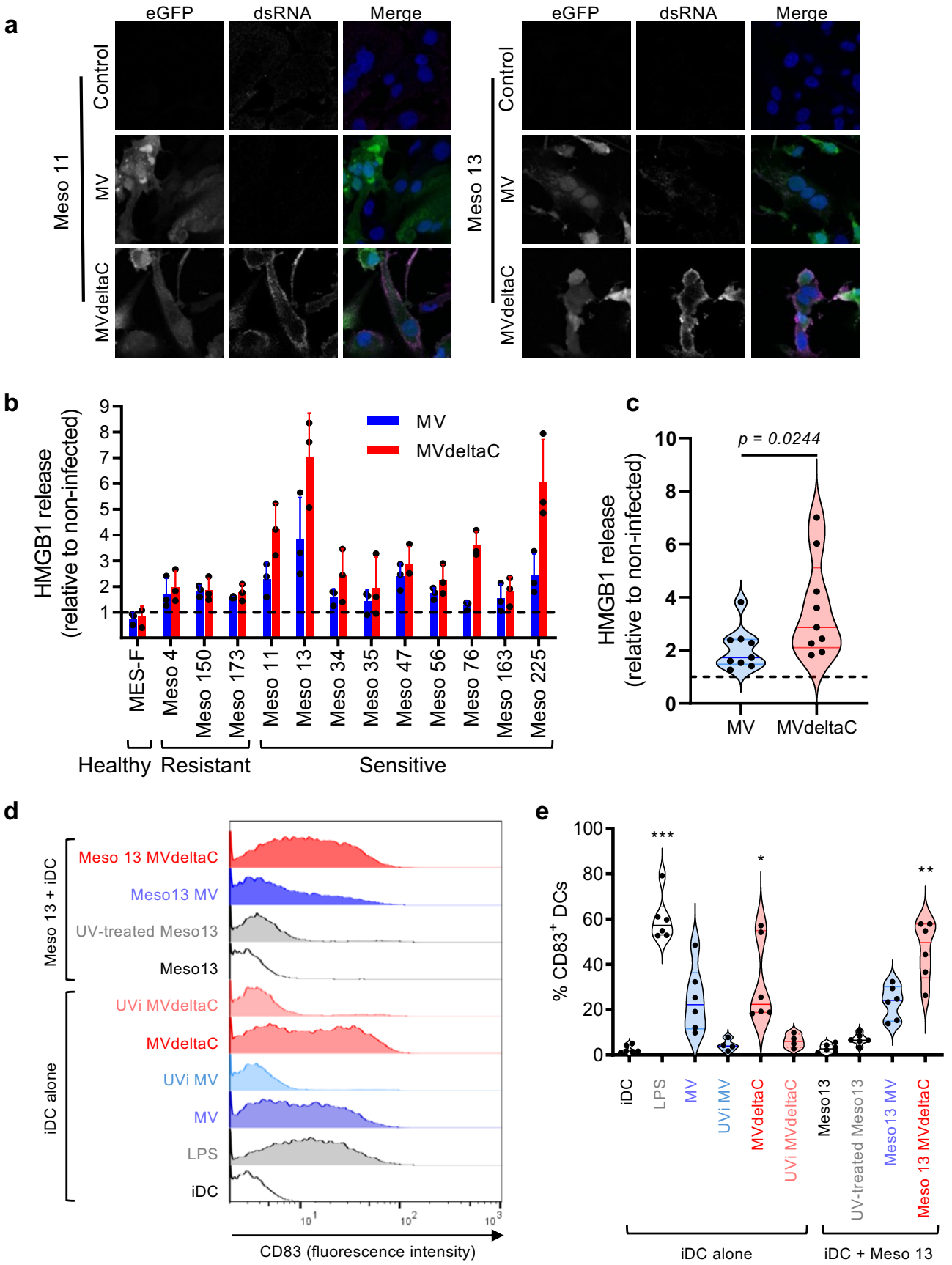

Figure 7. MVdeltaC induces danger signal production by tumor cells and promotes dendritic cell maturation. (a) Confocal microscopy of dsRNA (purple) in mesothelioma cells infected for 48h with either MV-eGFP or MVdeltaC-eGFP (MOI = 1, green). DNA is labeled with Hoechst (blue). (b) HMGB1 release in supernatants of healthy mesothelial MES-F cells and mesothelioma cells measured by ELISA 72 h after infection with MV Schwarz or MVdeltaC (MOI=1). Data represent means ± SD of three independent experiments. (c) Comparison of HMGB1 release between the MV and MVdeltaC conditions for MV-sensitive cell lines presented in (b); two-tailed Mann-Whitney test. (d-e) Immature human dendritic cells (iDCs) cultured for 20h in presence of LPS (1µg/mL), MV Schwarz or MVdeltaC (2×10^5) previously UV-inactivated or not, or Meso13 mesothelioma cells previously exposed to UV-B (10J/cm²) or infected for 72h with MV Schwarz or MVdeltaC. HLA-DR$^+$ DCs were then analyzed by flow cytometry for CD83 surface expression as shown for one experiment (d) or for 6 independent experiments (e); Kruskal-Wallis test.

FIGURE 8

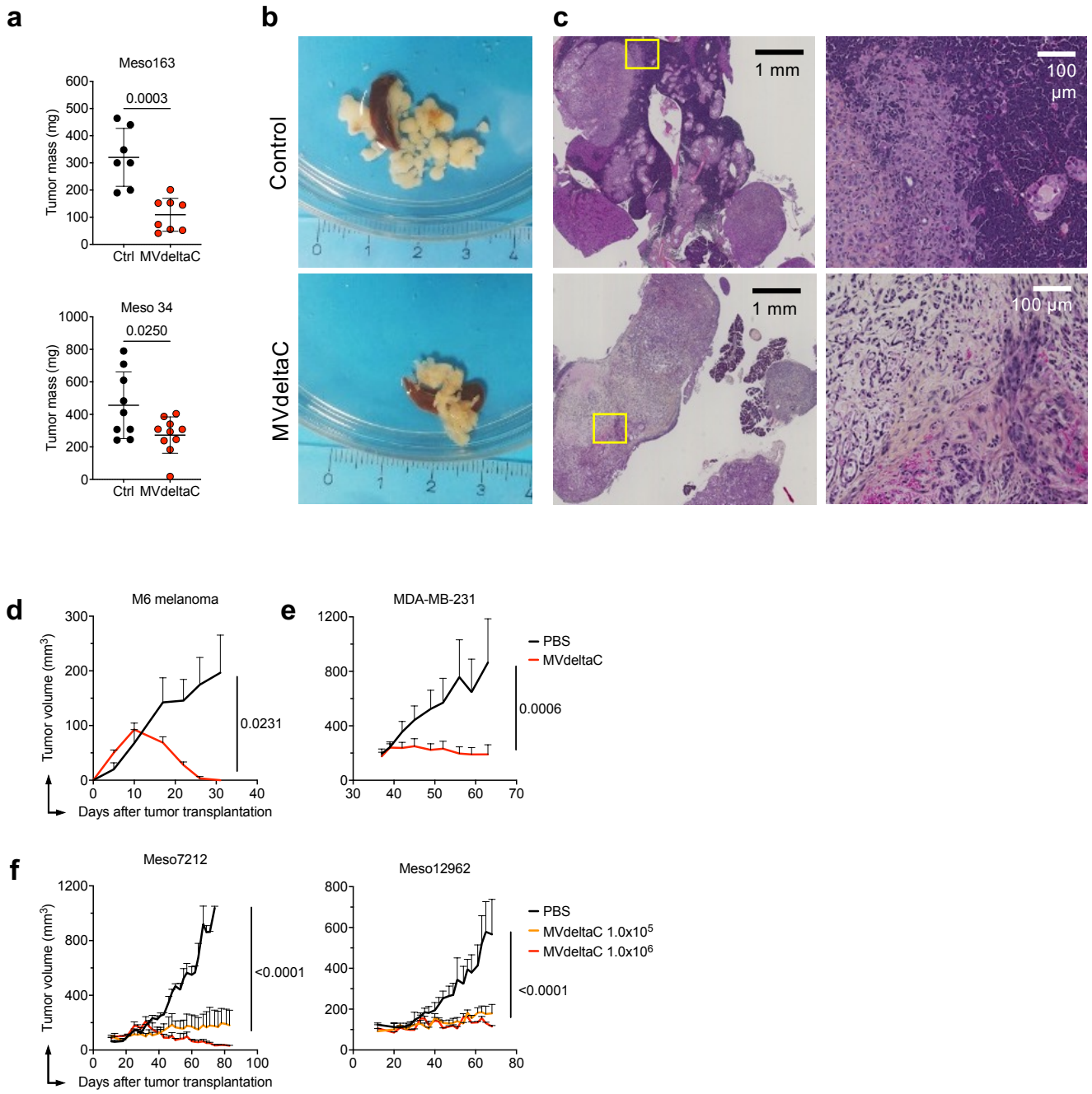

Figure 8. MVdeltaC controls human tumor growth in immunodeficient mouse models. (a) Meso 163 (upper panel) and Meso 34 (lower panel) tumor weights in NOD/SCID mice two weeks after single i.p. injection of MVdeltaC; means ± SD, n=7 - 10 mice per group; unpaired two-tailed t test. (b) Representative images of Meso 34 tumor nodules from treated and control animals. (c) Hematoxylin-phloxine-saffron staining of the peritoneum with detailed view of the tumor area (right). (d) Human M6 melanoma tumor growth in NOD:SCID mice treated with two i.t. injections of MVdeltaC on days 10 and 17; means ± SEM, n = 4 mice per group; one-tailed t test. (e) Triple-negative breast cancer MDA-MB-231 tumor growth in NMRI nu/nu mice after weekly i.t. injections of MVdeltaC. Therapy started on day 38, for a total of eight bi-weekly injections; means ± SEM, n=6 mice per group; unpaired one-tailed t test. (f) mesothelioma PDX tumor growth in NMRI nu/nu mice after weekly MVdeltaC therapy at two doses; means ± SEM, n = 3 mice per group; each group was compared to PBS group (unpaired one-tailed t test).

FIGURE S1

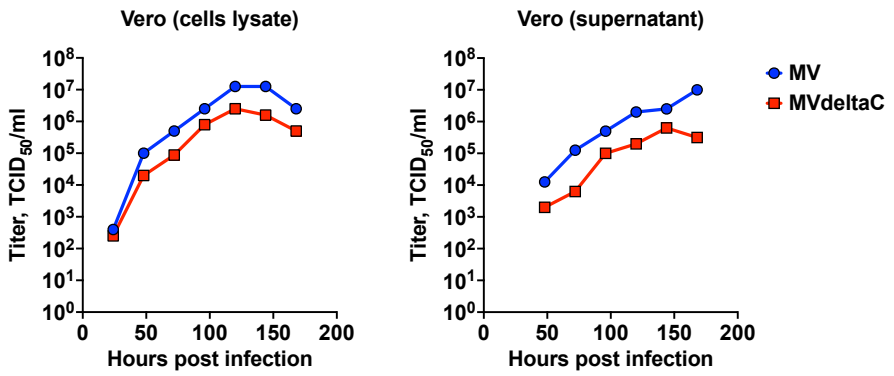

Figure S1. Growth kinetics of MV and MVdeltaC on Vero cells. Cells were infected at MOI 0.01 and incubated at 32°C. The data show reciprocal endpoint dilution titers of cell-associated (left) and cell-free (right) viruses.

FIGURE S2

Figure S2. Sequencing analysis of MVdeltaC passages. Reads coverage and proportion of intrasample single nucleotide variants (iSNVs) obtained from next-generation sequencing of MVdeltaC at passages 5 (P5) and 10 (P10). A schematic of the measles virus genome is shown below using the same scale, with the two engineered mutations preventing C protein expression highlighted. No sequence changes were detected at either of these positions in P5 or P10 samples.

FIGURE S3

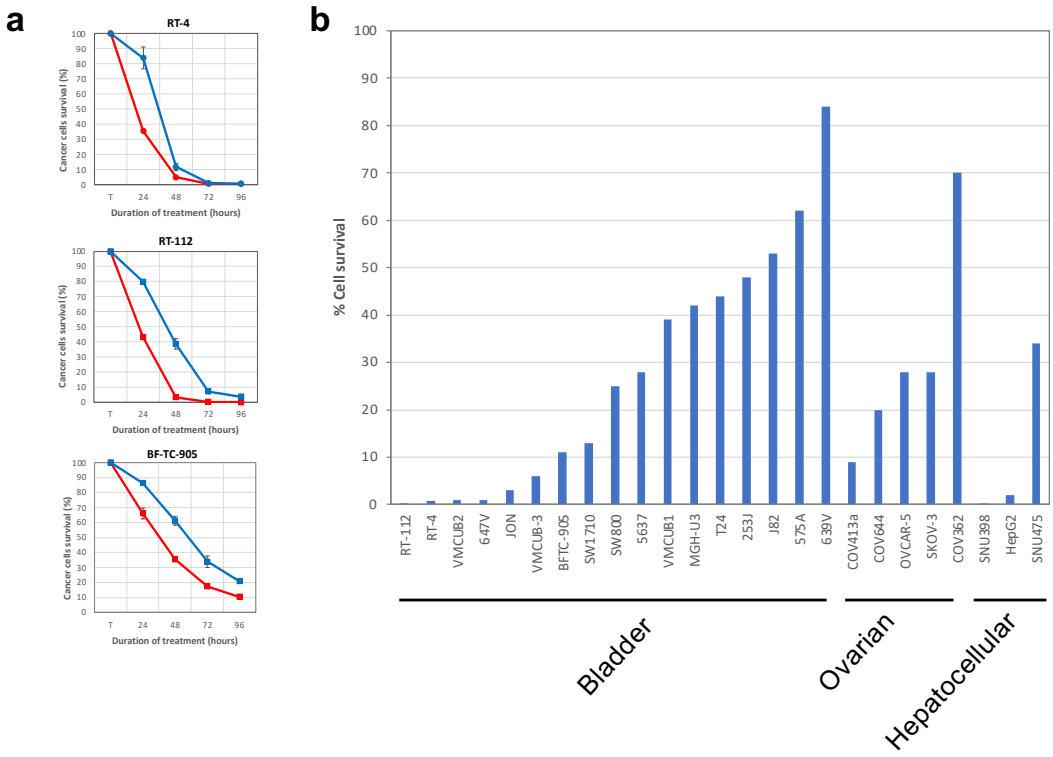

Figure S3. Infection and killing of human cancer cells by MVdeltaC. (a) Cell survival of three human bladder cancer cell lines after infection with MV (blue) or MVdeltaC (red) at MOI 5, measured by CellTiter-Glo assay; means ± SD; measurements are in triplicate; data normalized to non-infected cells. (b) MVdeltaC killing of a series of human cancer cells of bladder, ovarian or hepatocellular origin as determined by CellTiterGlo assay (cancer cells survival after 72 hours of infection at MOI 5).

FIGURE S4

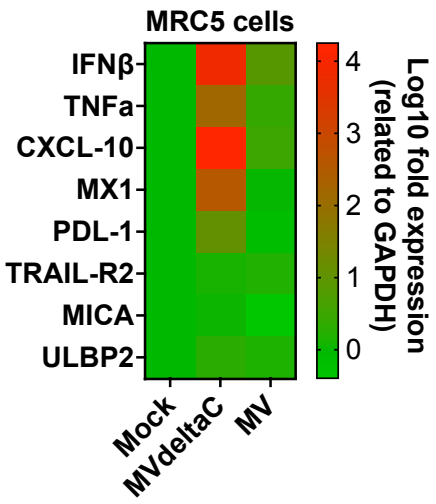

Figure S4. Gene expression analysis in infected MRC5 cells. Heatmap of differentially expressed genes in MRC5 cells after 24h incubation with MV, MVdeltaC (MOI 1) or PBS (Mock); experiment in triplicate, a gradient of colors from green to red represent log_{10} fold change values from lowest to highest, respectively.

FIGURE S5

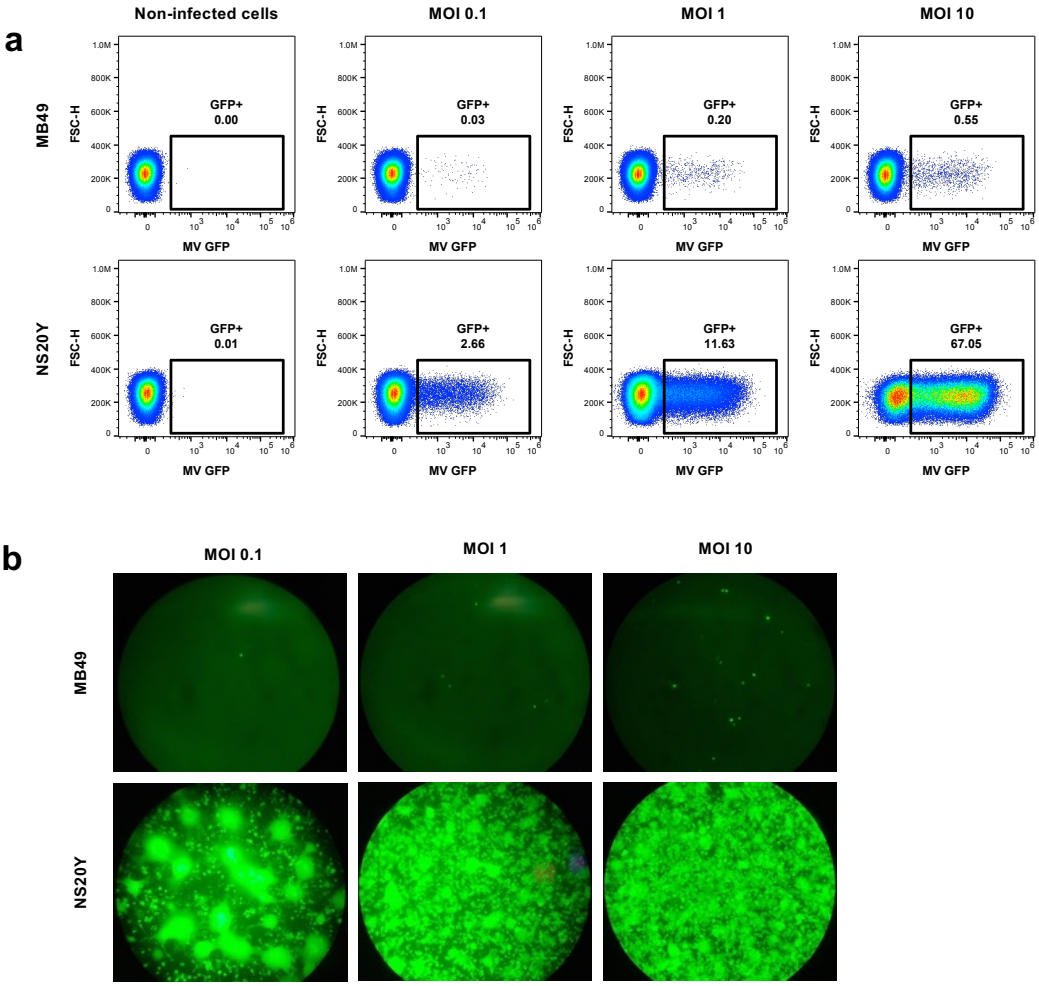

Figure S5. NS20Y cells are permissive to measles infection. Mouse neuroblastoma NS20Y cells and bladder carcinoma MB49 cells were infected with MV-eGFP at the indicated MOI and analyzed by (a) flow cytometry 24 hours post-infection, and (b) immunofluorescence microscopy 72 h hours post-infection.

FIGURE S6

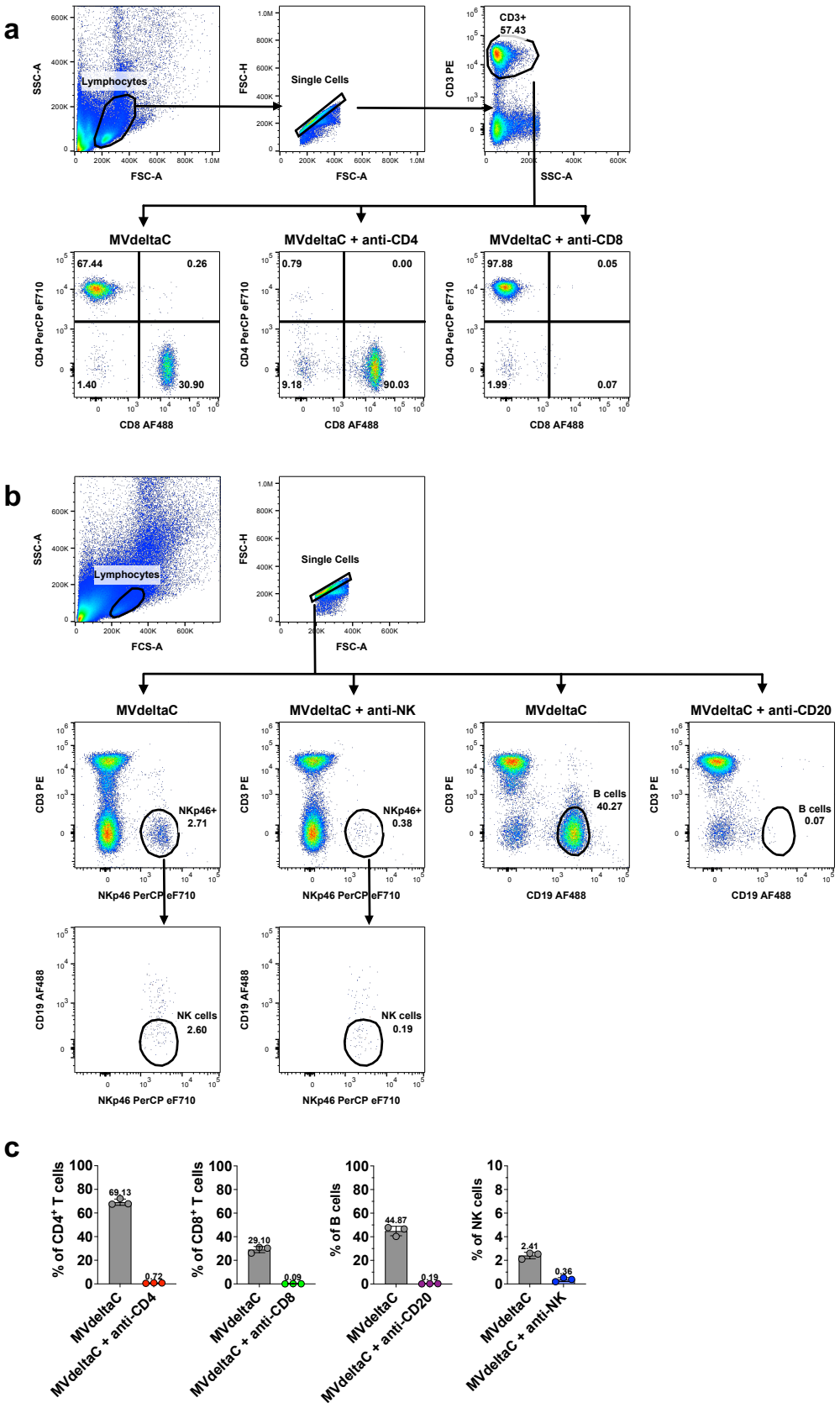

Figure S6. Flow cytometry analysis of immune cell populations in the blood of A/J mice depleted for CD4$^+$, CD8$^+$, B or NK cells. (a) Representative dot plots show the flow cytometry gating strategy to identify CD4$^+$ (CD3$^+$ CD4$^+$ CD8$^-$), CD8$^+$ (CD3$^+$ CD8$^+$ CD4$^-$) or (b) NK (CD3$^-$ NKp46$^+$ CD19$^-$) and B (CD3$^-$ CD19$^+$) cell populations in the blood of treated mice. Mice were grafted with 5x10^6 NS20Y murine tumor cells on day 0. T cell depletion was achieved by i.p. injection of anti-CD4 or anti-CD8 mAbs (200 µg in 100 µL of PBS) on days 5, 6 and 7 after NS20Y cells injection. NK or B cell depletion was performed on days 5 and 7 using 50µg of anti-asialo GM1 or 200µg of anti-CD20 antibodies, respectively. Sustained immune cell depletion was achieved by weekly antibody administrations on days 14 and 21. Tumor therapy with MVdeltaC at 2x10^{6}TCID$_{50}$ was performed on days 6, 9 and 12. Immune cell populations in the groups of A/J mice were analyzed on day 27. (c) Bar graphs show flow cytometry data for the three animals from each group, means ± SD.

FIGURE S7

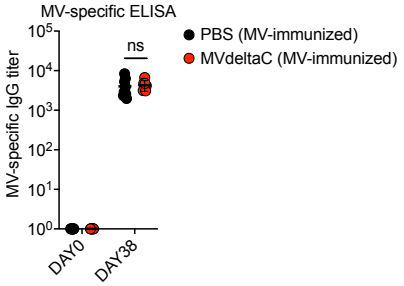

Figure S7. MV-specific IgG antibody responses in A/J mice following MV Schwarz vaccination. Mice were immunized i.p. with MV Schwarz (1×10^5 $TCID_{50}$) on day 0. Sera were collected at day 38 post-immunization and assessed for IgG antibody responses to MV antigens by ELISA. The data show the reciprocal endpoint dilution titers of MV-specific IgG antibodies in preimmune (day 0) and day 38 sera; each point represents an individual mouse; means ± SD, n= 7-9 per group; unpaired two-tailed t test; ns, not significant.

FIGURE S8

a

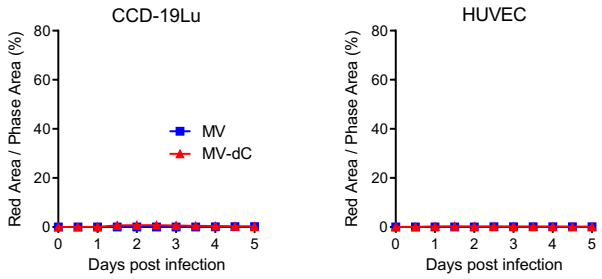

b

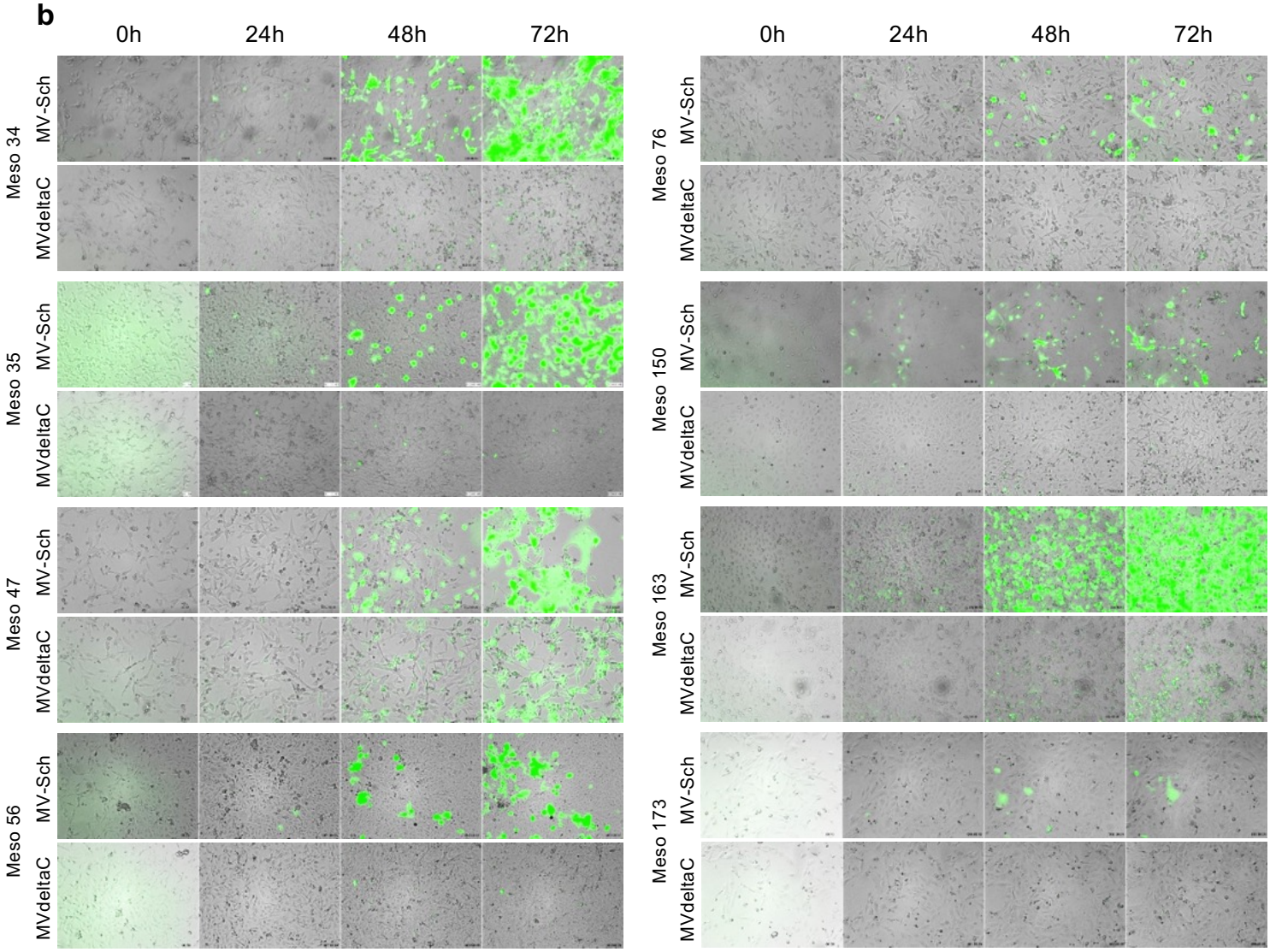

Figure S8. Infection of healthy and cancer human cells by MV or MVdeltaC. (a) Quantification of virus propagation in healthy lung fibroblasts (CCD19-Lu) or endothelial cells (HUVECs) infected with either MV-mCherry or MVdeltaC-mCherry. (b) Time-lapse microscopy analysis of mesothelioma cell lines infected with MV-eGFP or MVdeltaC-eGFP (MOI = 1).

FIGURE S9

VIDEOS MESO13

Figure S9. Infection of Meso 13 mesothelioma cells by MV or MVdeltaC.
Time-lapse microscopy analysis of mesothelioma cell lines infected with MV-eGFP (a) or MVdeltaC-eGFP (b) (MOI = 1).

FIGURE S10

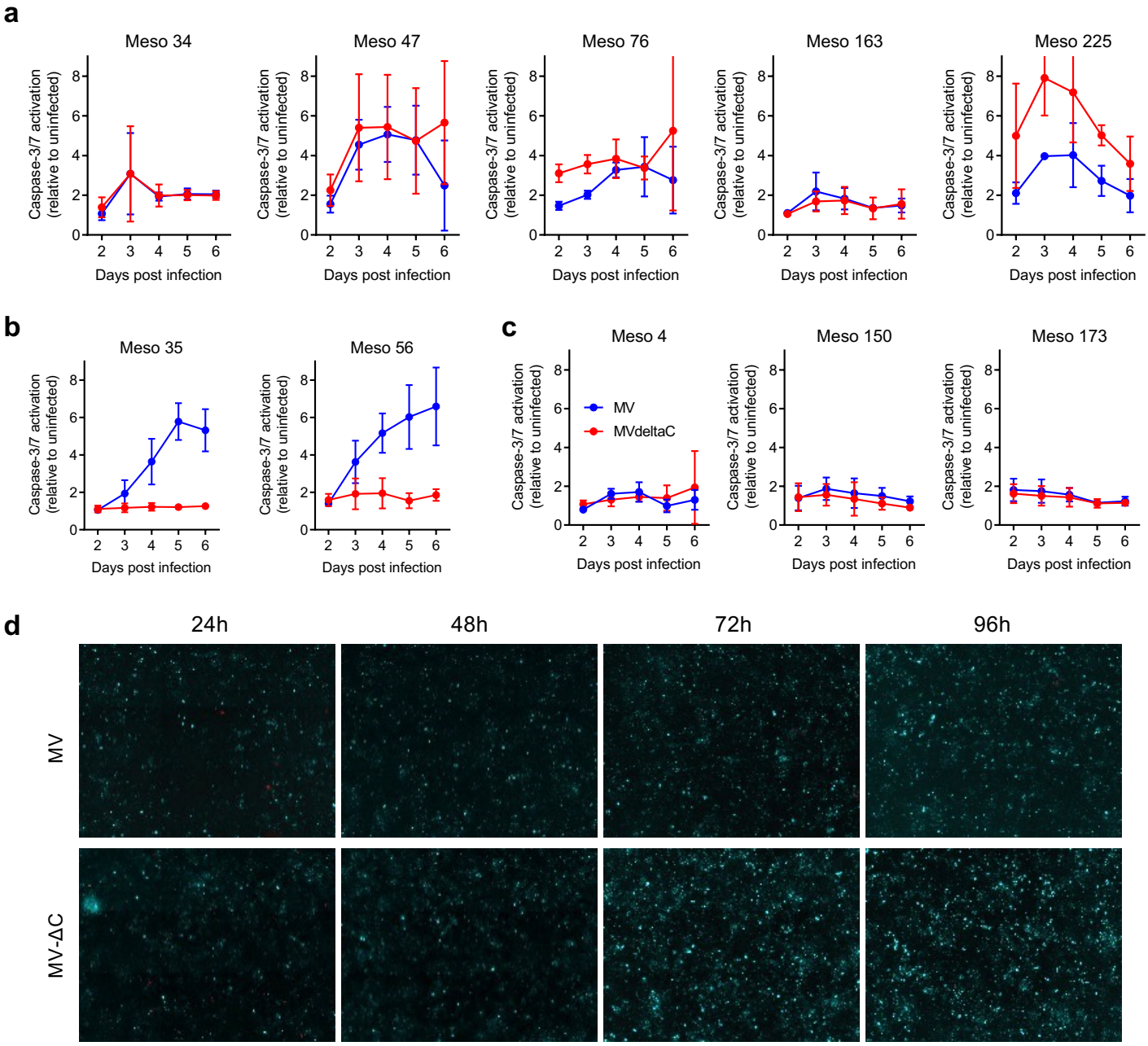

Figure S10. Activation of Caspases-3/7 in mesothelioma cells infected by MVdeltaC. (a-c) Luminescence-based quantification of caspase-3/7 activity in human mesothelioma cell lines. (a) MV-permissive, (b) MVdeltaC-resistant, and (c) MV-resistant cells. (d) Fluorescence microscopy of Meso 4 cells showing caspase-3/7 activation (cyan) after infection with MV-mCherry or MVdeltaC-mCherry (red).

FIGURE S11

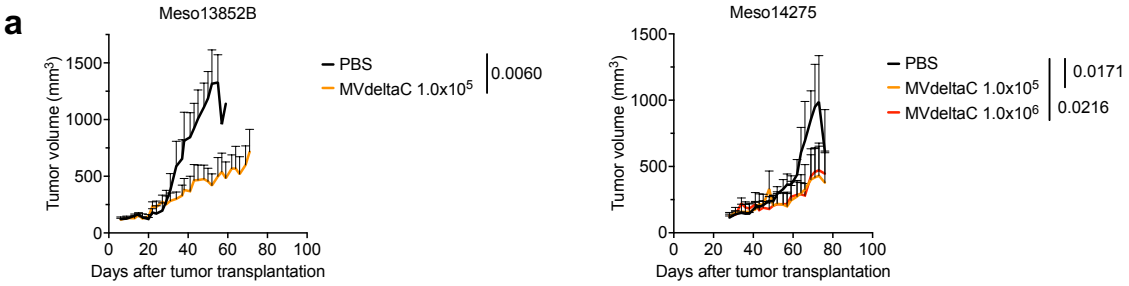

Figure S11. MVdeltaC inhibits human PDX growth in immunodeficient mice. Growth of mesothelioma PDX tumors in NMRI nu/nu mice after weekly MVdeltaC therapy at two doses; means ± SEM, n = 3 mice per group; each group was compared to PBS group (unpaired one-tailed t test).

FIGURE 1

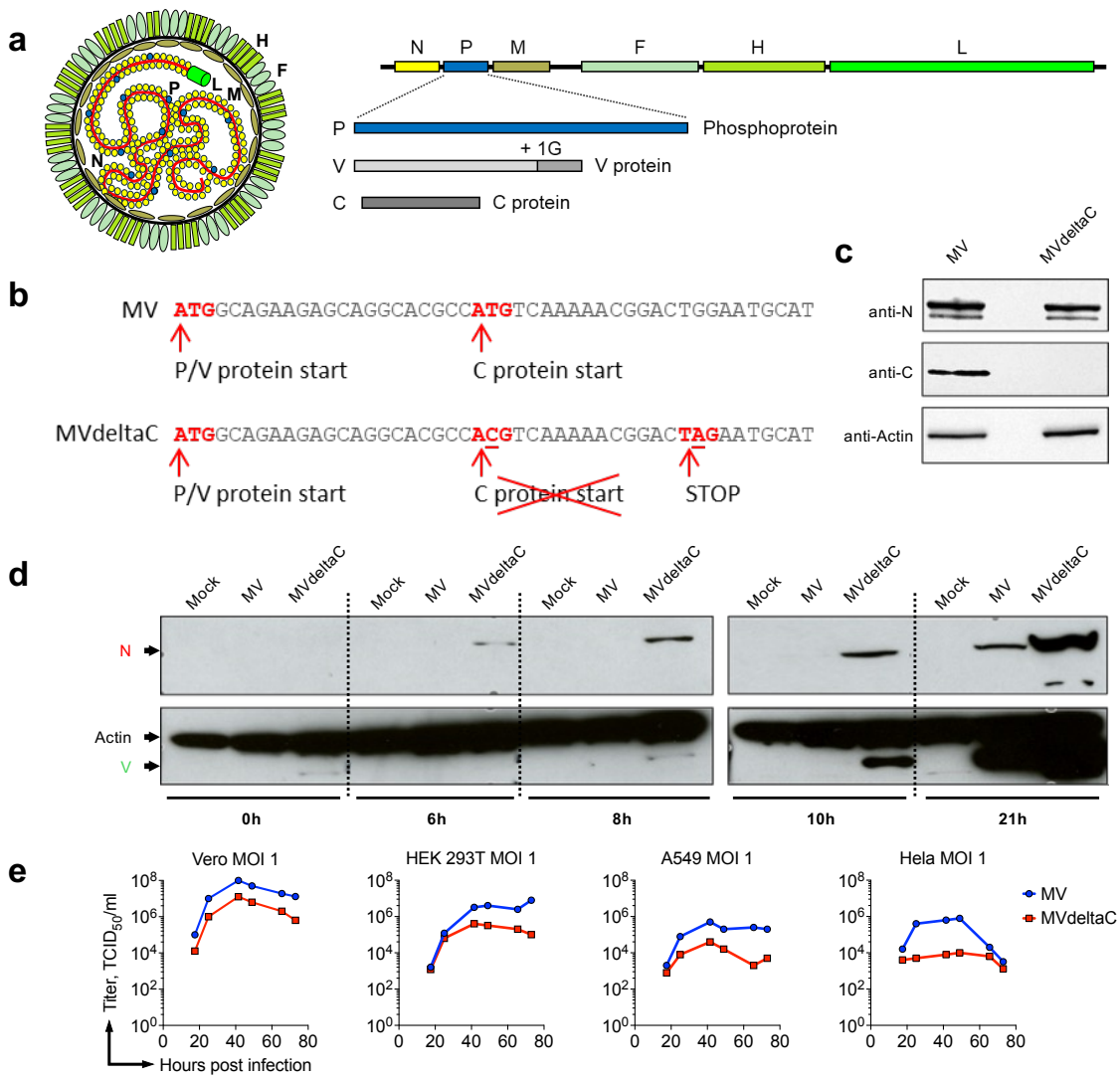

Figure 1. Characterization of MVdeltaC virus. (a) Schematic of the measles viral particle, genome and proteins: nucleoprotein (N), phosphoprotein (P), matrix (M), fusion (F), hemagglutinin (H) and polymerase (L). ORFs for P, V, and C are enlarged. (b) Nucleotide sequence of the P and C ORFs with the mutations (underlined) introduced in MVdeltaC to disrupt C protein expression. (c) Expression of N and C proteins in lysates of Vero cells infected by MV Schwarz or MVdeltaC, analysed by western blot. (d) Kinetics of N and V proteins expression in Vero cell lysates after infection with MV Schwarz or MVdeltaC at MOI 1. (e) Comparative growth kinetics of MV Schwarz (blue) and MVdeltaC (red) in different cell lines infected at MOI 1 and cultured at 37° C. Viruses were harvested from cell lysates at the indicated time points.

FIGURE 2

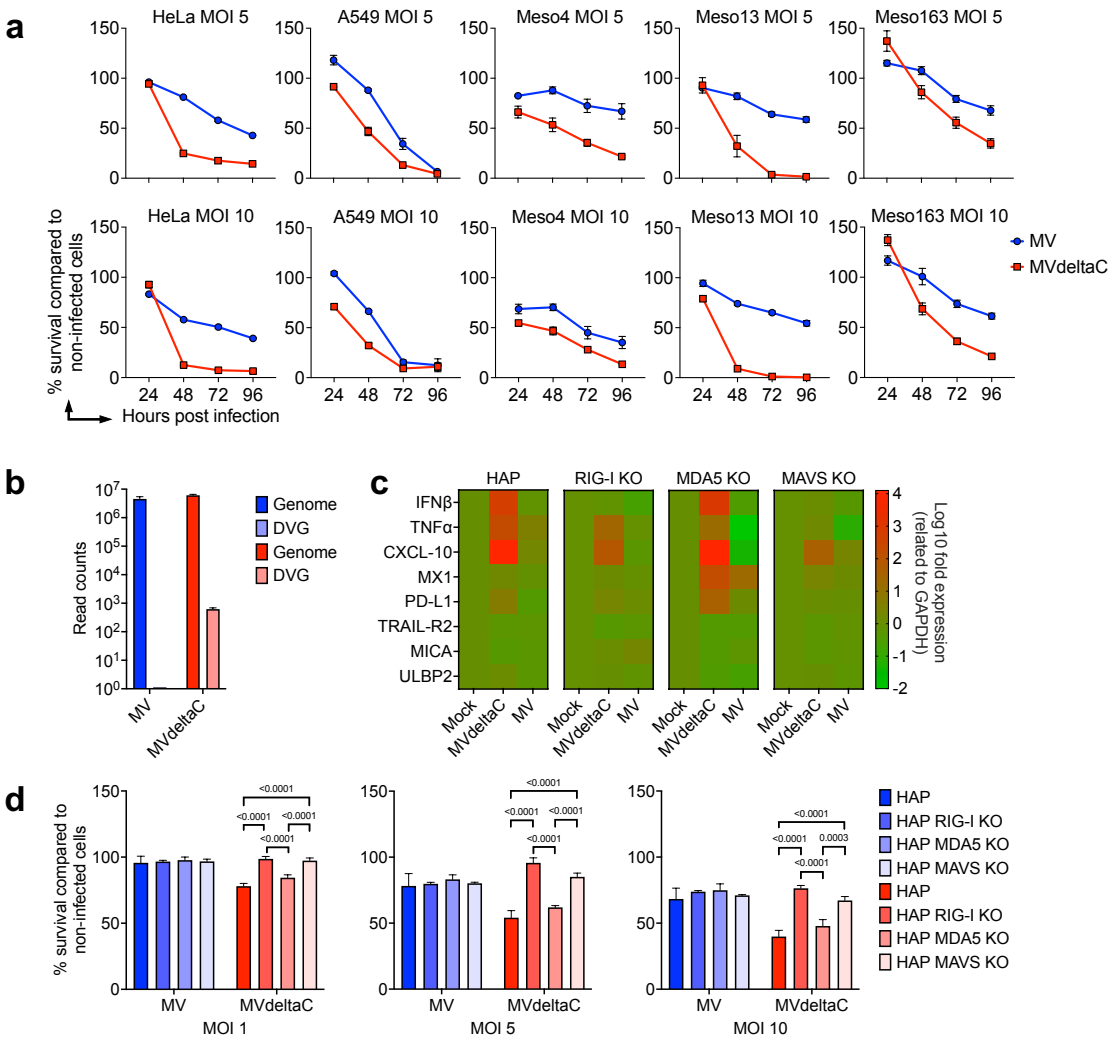

Figure 2. MVdeltaC induces accelerated RIG-I-dependent innate immune activation and killing of cancer cells. (a) Viability of human cancer cell lines infected with MV (blue) or MVdeltaC (red) at increasing MOIs, measured by CellTiter-Glo assay; data normalized to non-infected cells; mean ± SD, n = 3. (b) NGS quantification of DVGs in HAP1 cells infected with MV or MVdeltaC. Bars show total viral reads aligned to MV genome and DVG read counts as detected by DI-tector; mean ± SD, n=3. (c) Innate immunity gene expression profiles in wild-type and knockout HAP1 cells 24 h after infection with MV, MVdeltaC, or PBS (Mock). Heatmap shows $\log_{10}$ fold changes of differentially expressed genes; experiment in triplicate, a gradient of colors from green to red represent lowest to highest values, respectively, under all conditions. (d) Viability of wild-type, RIG-I KO, MDA5 KO, and MAVS KO HAP1 cells 24 h after infection with MV or MVdeltaC at MOI 1; means ± SD of three independent experiments; two-way ANOVA test with Šídák's multiple comparisons test.

FIGURE 3

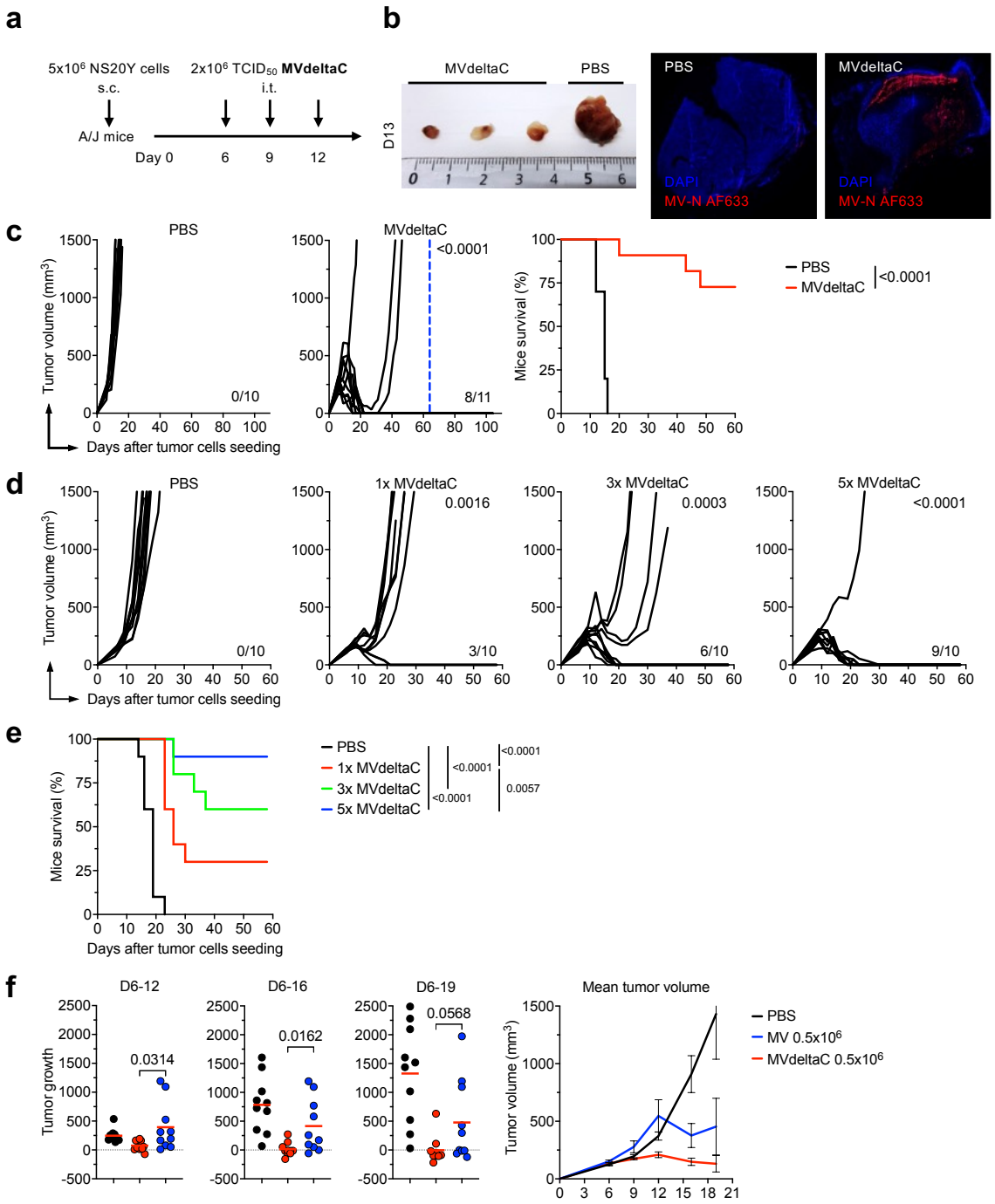

Figure 3. MVdeltaC induces potent NS20Y neuroblastoma tumor rejection in immunocompetent A/J mice. (a) Schematic of the syngeneic NS20Y/AJ model and MVdeltaC treatment schedule. (b) Left, representative tumors excised from the mice on day 13; right, immunofluorescence of tumor cryosections stained for measles nucleoprotein (MV-N, red) and DNA (DAPI, blue). (c) Tumor growth kinetics (black lines, individual mice) and survival after three i.t. injections of MVdeltaC (2×10^6 $TCID_{50}$) or PBS. Blue dotted line indicates the day of tumor re-challenge; n = 10-11 mice per group; MVdeltaC group was compared to PBS-treated group; unpaired one-tailed t test comparing the mean tumor sizes of each group; log-rank test for survival. (d) Tumor growth kinetics after one (1x MVdeltaC, day 6), three (days 6, 9 and 12) or five (days 6, 9, 12, 15 and 19) i.t. injections of MVdeltaC; n = 10 mice per group; each group was compared to PBS-treated group; unpaired one-tailed t test. (e) Kaplan–Meier survival curves for the same groups; log-rank test. (f) Comparison of tumor control by MVdeltaC (red) and parental MV (blue). Left, tumor growth calculated as the change in tumor volume between treatment initiation (day 6) and study days 12, 16, or 19; unpaired two-tailed t-test. Right, mean tumor volume ± SEM, n = 10 mice per group.

FIGURE 4

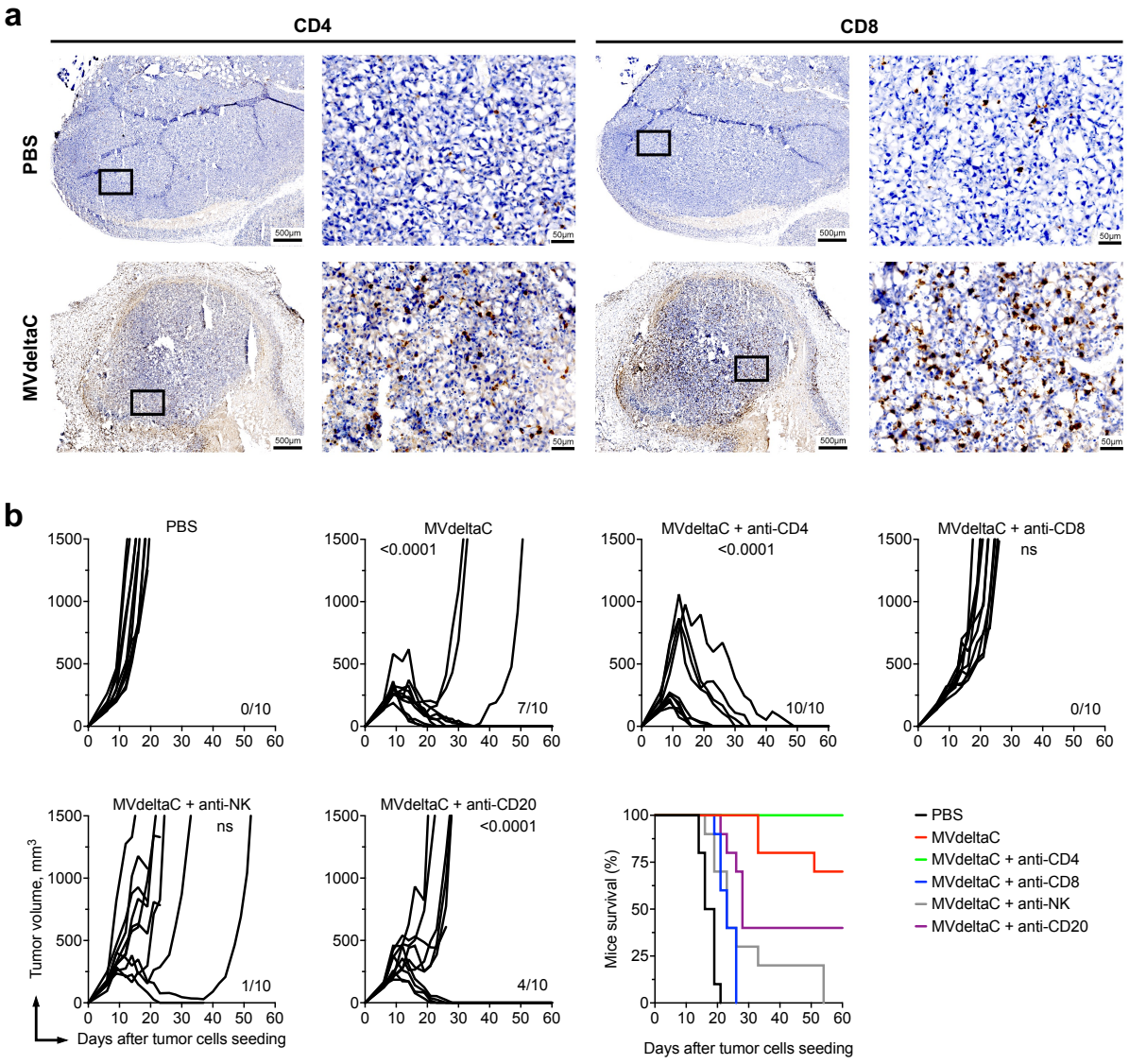

Figure 4. MVdeltaC induces massive T cells infiltration into tumors, and rejection efficacy relies on a functional immune system. (a) Immunohistochemistry of NS20Y tumors 24 h after the third i.t. injection of MVdeltaC, stained for $CD4^+$ and $CD8^+$ T cells. (b) Tumor growth and survival in mice depleted of $CD4^+$, $CD8^+$, B cells or NK cells during MVdeltaC therapy. Depletion was maintained by weekly antibody administration until day 49. Tumor therapy with MVdeltaC was performed on days 6, 9 and 12; n = 10 mice per group; each group was compared to PBS-treated group; unpaired one-tailed t test; ns, not significant.

FIGURE 5

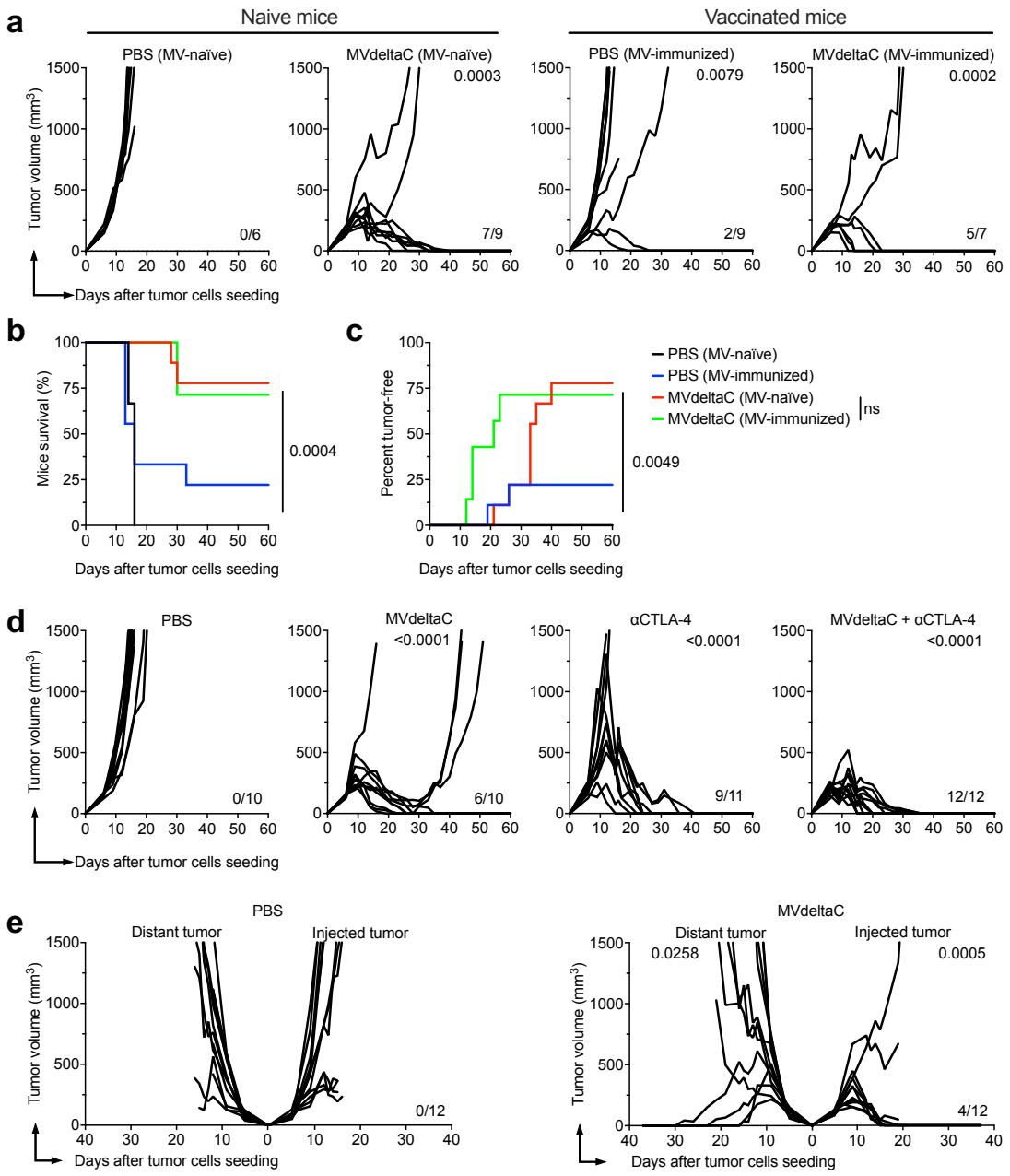

Figure 5. MVdeltaC therapy is not affected by preexisting measles immunity, is enhanced by anti-CTLA-4 therapy and exhibits abscopal effect. (a) NS20Y tumor growth in MV-naïve or measles pre-vaccinated mice treated i.t. with MVdeltaC or PBS on days 6, 9, 12 and 19 after tumor cells seeding. (b) Survival rates, and (c) percentage of tumor-free animals in naïve or pre-vaccinated mice; *n* = 6-9 mice per group; each group was compared to MV-naïve PBS-treated group, unpaired one-tailed t test; log-rank test for survival. (d) Tumor growth in mice treated with three i.t. injections of MVdeltaC and/or four i.p. injections of anti-CTLA-4 (αCTLA-4) antibody on days 6, 9, 12 and 15; n = 10-12 mice per group; each group was compared to PBS group (unpaired one-tailed t test). (e) Growth of injected and contralateral uninjected (distant) tumors in mice treated with MVdeltaC in single tumor; n = 12 mice per group; MVdeltaC-injected and distant tumors were compared to their corresponding PBS controls; unpaired one-tailed t test.

FIGURE 6

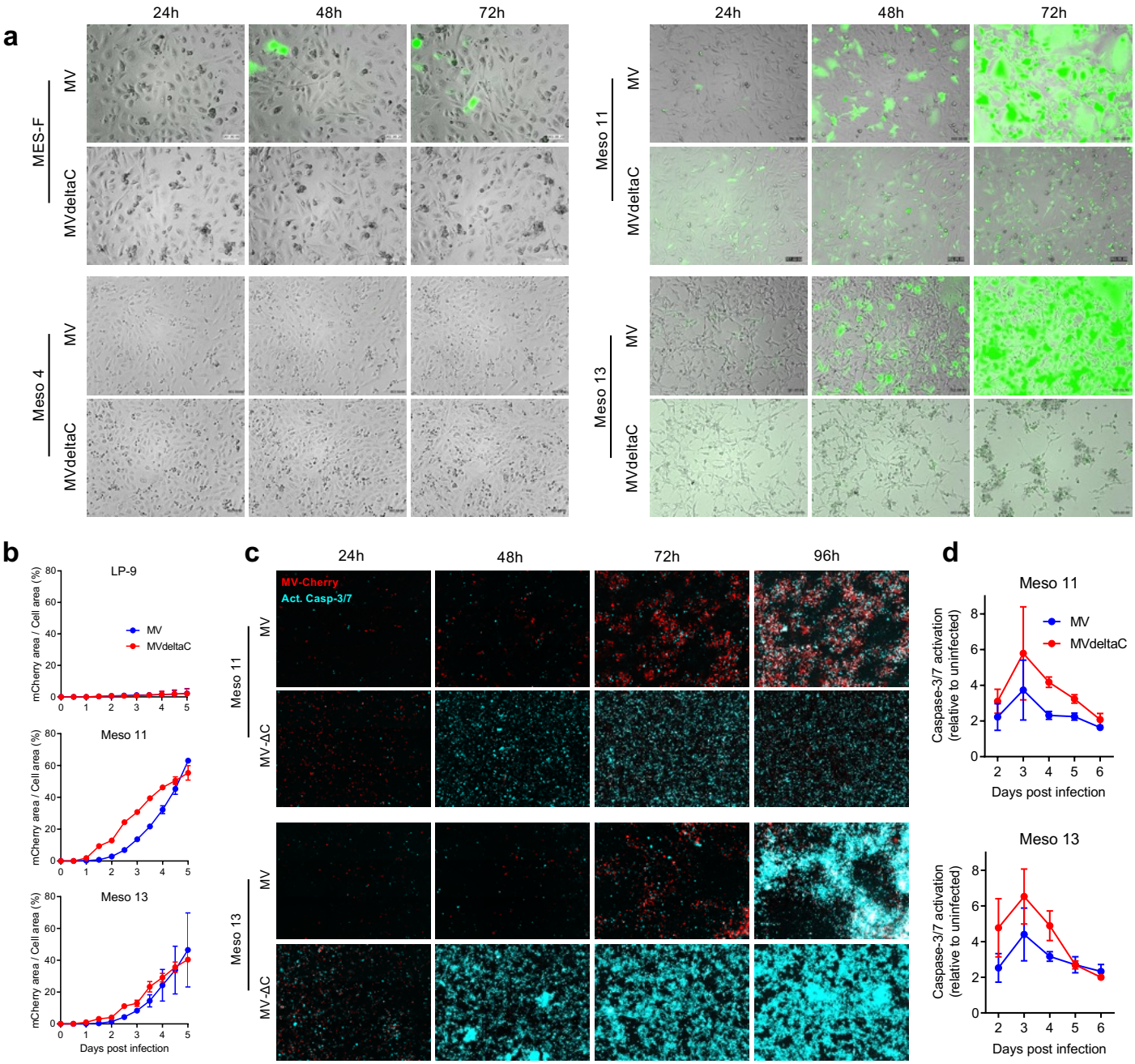

Figure 6. Oncolytic activity of MVdeltaC in human mesothelioma cells. (a) Time-lapse microscopy of healthy mesothelial (MES-F) and mesothelioma (Meso 4, Meso 11, Meso 13) cells infected with MV-eGFP or MVdeltaC-eGFP at MOI 1. (b) Quantification of virus propagation in normal mesothelial (LP-9) and mesothelioma (Meso 11, Meso 13) cells infected with either MV-mCherry or MVdeltaC-mCherry. (c) Caspase-3/7 activation (NucView probe, cyan) detected by fluorescent microscopy in mesothelioma cells infected with either MV-mCherry or MVdeltaC-mCherry (red). (d) Caspase-3/7 activity measured by luminescence (Caspase-3/7-Glo). Data are mean ± SD of at least three independent experiments.

FIGURE 7

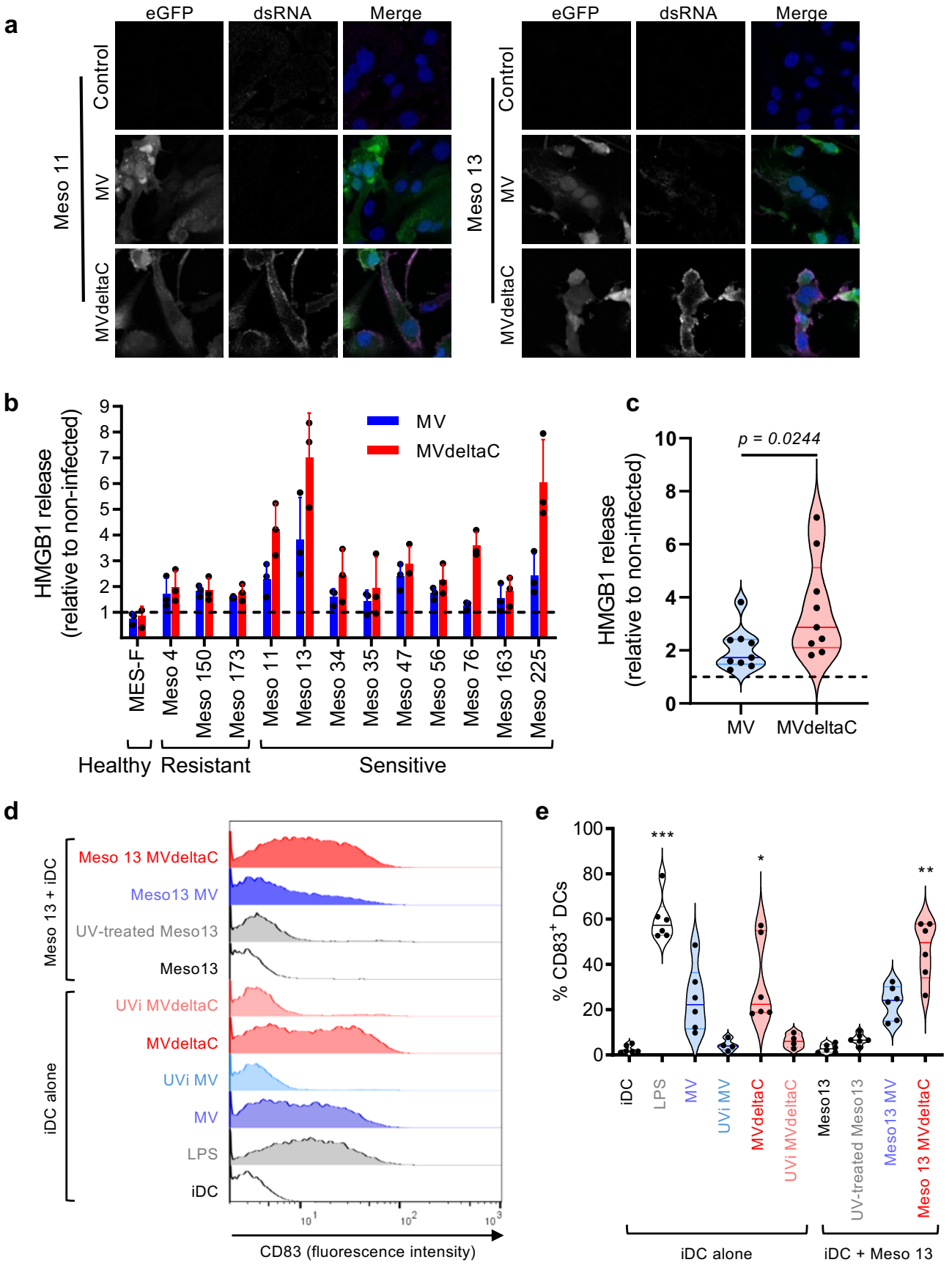

Figure 7. MVdeltaC induces danger signal production by tumor cells and promotes dendritic cell maturation. (a) Confocal microscopy of dsRNA (purple) in mesothelioma cells infected for 48h with either MV-eGFP or MVdeltaC-eGFP (MOI = 1, green). DNA is labeled with Hoechst (blue). (b) HMGB1 release in supernatants of healthy mesothelial MES-F cells and mesothelioma cells measured by ELISA 72 h after infection with MV Schwarz or MVdeltaC (MOI=1). Data represent means ± SD of three independent experiments. (c) Comparison of HMGB1 release between the MV and MVdeltaC conditions for MV-sensitive cell lines presented in (b); two-tailed Mann-Whitney test. (d-e) Immature human dendritic cells (iDCs) cultured for 20h in presence of LPS (1µg/mL), MV Schwarz or MVdeltaC (2×10^5) previously UV-inactivated or not, or Meso13 mesothelioma cells previously exposed to UV-B (10J/cm²) or infected for 72h with MV Schwarz or MVdeltaC. HLA-DR$^+$ DCs were then analyzed by flow cytometry for CD83 surface expression as shown for one experiment (d) or for 6 independent experiments (e); Kruskal-Wallis test.

FIGURE 8

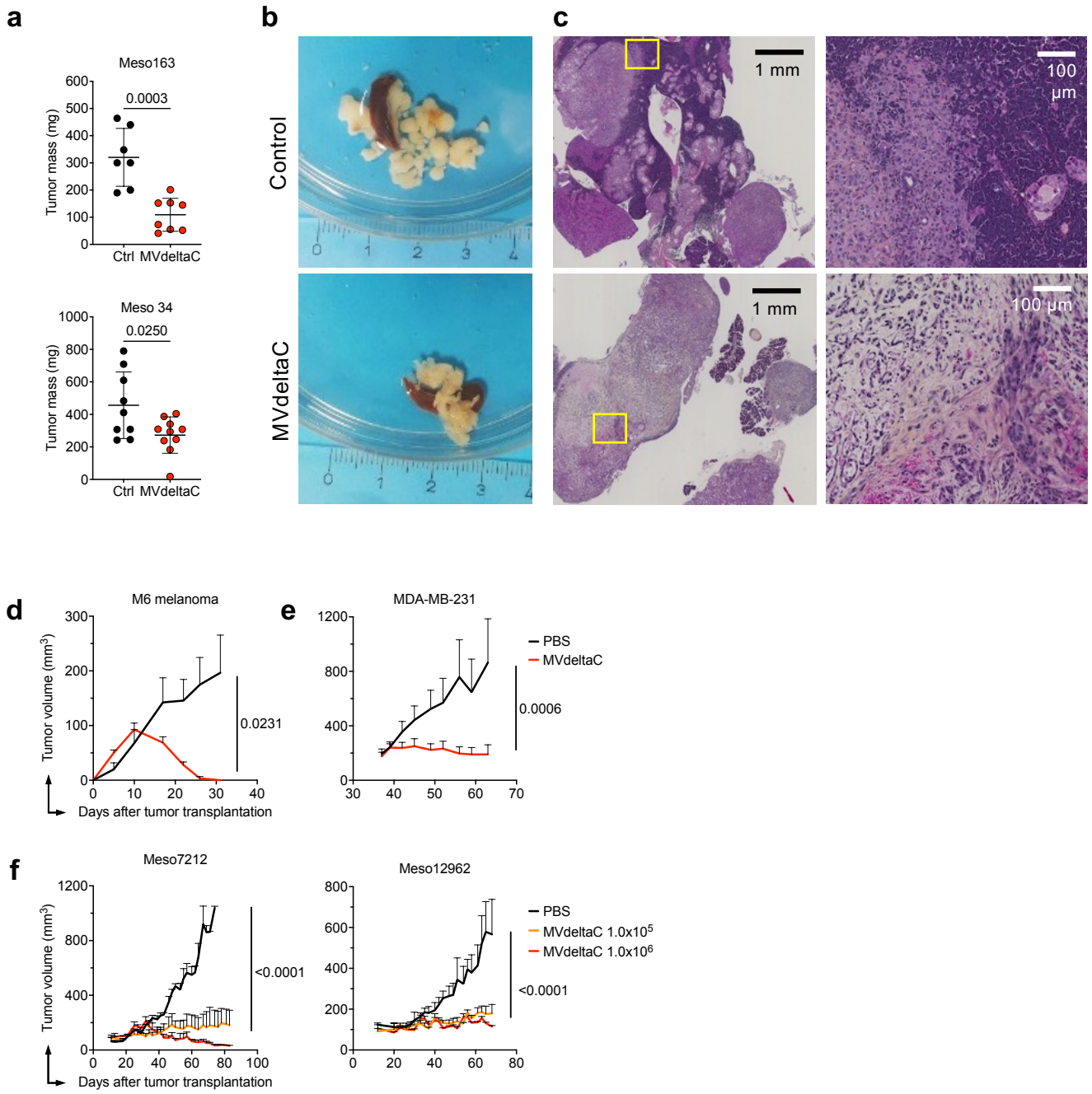

Figure 8. MVdeltaC controls human tumor growth in immunodeficient mouse models. (a) Meso 163 (upper panel) and Meso 34 (lower panel) tumor weights in NOD/SCID mice two weeks after single i.p. injection of MVdeltaC; means ± SD, n=7 - 10 mice per group; unpaired two-tailed t test. (b) Representative images of Meso 34 tumor nodules from treated and control animals. (c) Hematoxylin-phloxine-saffron staining of the peritoneum with detailed view of the tumor area (right). (d) Human M6 melanoma tumor growth in NOD:SCID mice treated with two i.t. injections of MVdeltaC on days 10 and 17; means ± SEM, n = 4 mice per group; one-tailed t test. (e) Triple-negative breast cancer MDA-MB-231 tumor growth in NMRI nu/nu mice after weekly i.t. injections of MVdeltaC. Therapy started on day 38, for a total of eight bi-weekly injections; means ± SEM, n=6 mice per group; unpaired one-tailed t test. (f) mesothelioma PDX tumor growth in NMRI nu/nu mice after weekly MVdeltaC therapy at two doses; means ± SEM, n = 3 mice per group; each group was compared to PBS group (unpaired one-tailed t test).

FIGURE S1

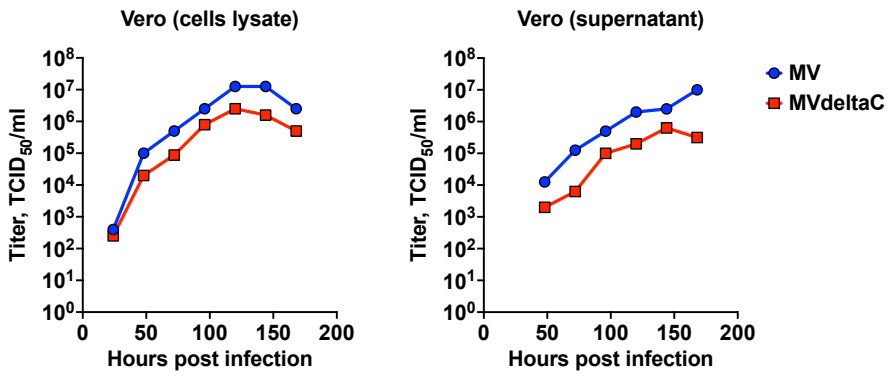

Figure S1. Growth kinetics of MV and MVdeltaC on Vero cells. Cells were infected at MOI 0.01 and incubated at 32°C. The data show reciprocal endpoint dilution titers of cell-associated (left) and cell-free (right) viruses.

FIGURE S2

Figure S2. Sequencing analysis of MVdeltaC passages. Reads coverage and proportion of intrasample single nucleotide variants (iSNVs) obtained from next-generation sequencing of MVdeltaC at passages 5 (P5) and 10 (P10). A schematic of the measles virus genome is shown below using the same scale, with the two engineered mutations preventing C protein expression highlighted. No sequence changes were detected at either of these positions in P5 or P10 samples.

FIGURE S3

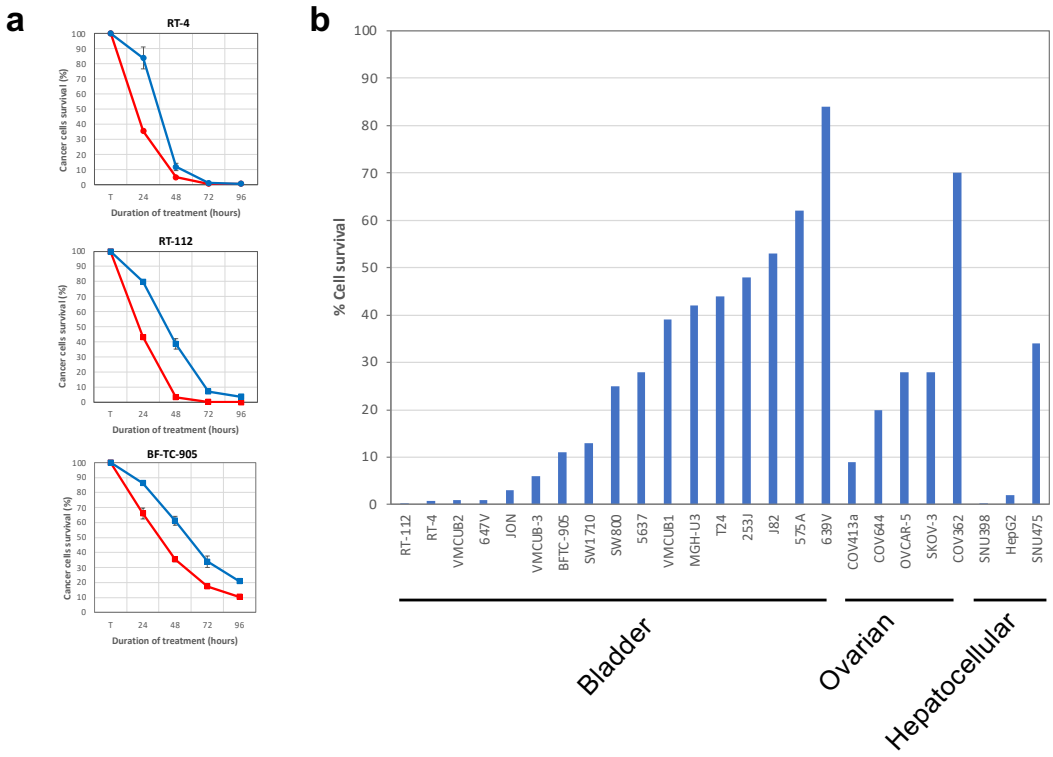

Figure S3. Infection and killing of human cancer cells by MVdeltaC. (a) Cell survival of three human bladder cancer cell lines after infection with MV (blue) or MVdeltaC (red) at MOI 5, measured by CellTiter-Glo assay; means ± SD; measurements are in triplicate; data normalized to non-infected cells. (b) MVdeltaC killing of a series of human cancer cells of bladder, ovarian or hepatocellular origin as determined by CellTiterGlo assay (cancer cells survival after 72 hours of infection at MOI 5).

FIGURE S4

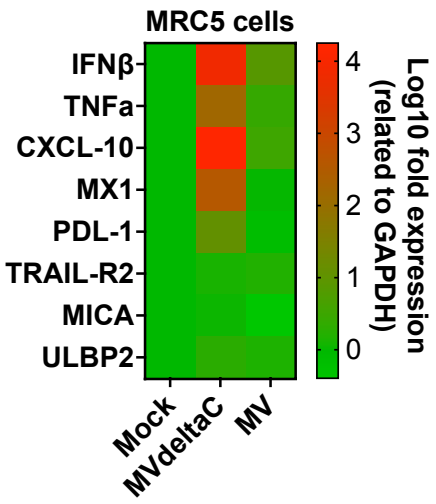

Figure S4. Gene expression analysis in infected MRC5 cells. Heatmap of differentially expressed genes in MRC5 cells after 24h incubation with MV, MVdeltaC (MOI 1) or PBS (Mock); experiment in triplicate, a gradient of colors from green to red represent log_{10} fold change values from lowest to highest, respectively.

FIGURE S5

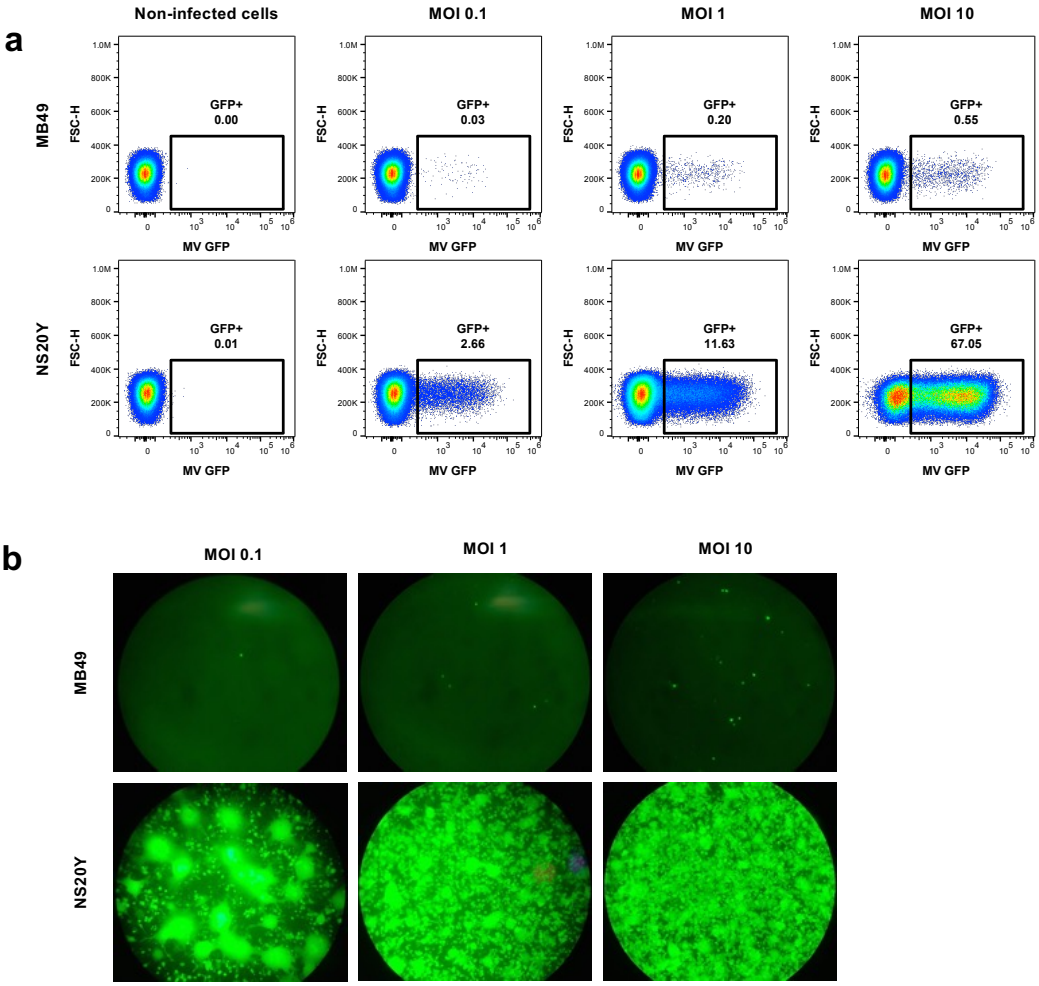

Figure S5. NS20Y cells are permissive to measles infection. Mouse neuroblastoma NS20Y cells and bladder carcinoma MB49 cells were infected with MV-eGFP at the indicated MOI and analyzed by (a) flow cytometry 24 hours post-infection, and (b) immunofluorescence microscopy 72 h hours post-infection.

FIGURE S6

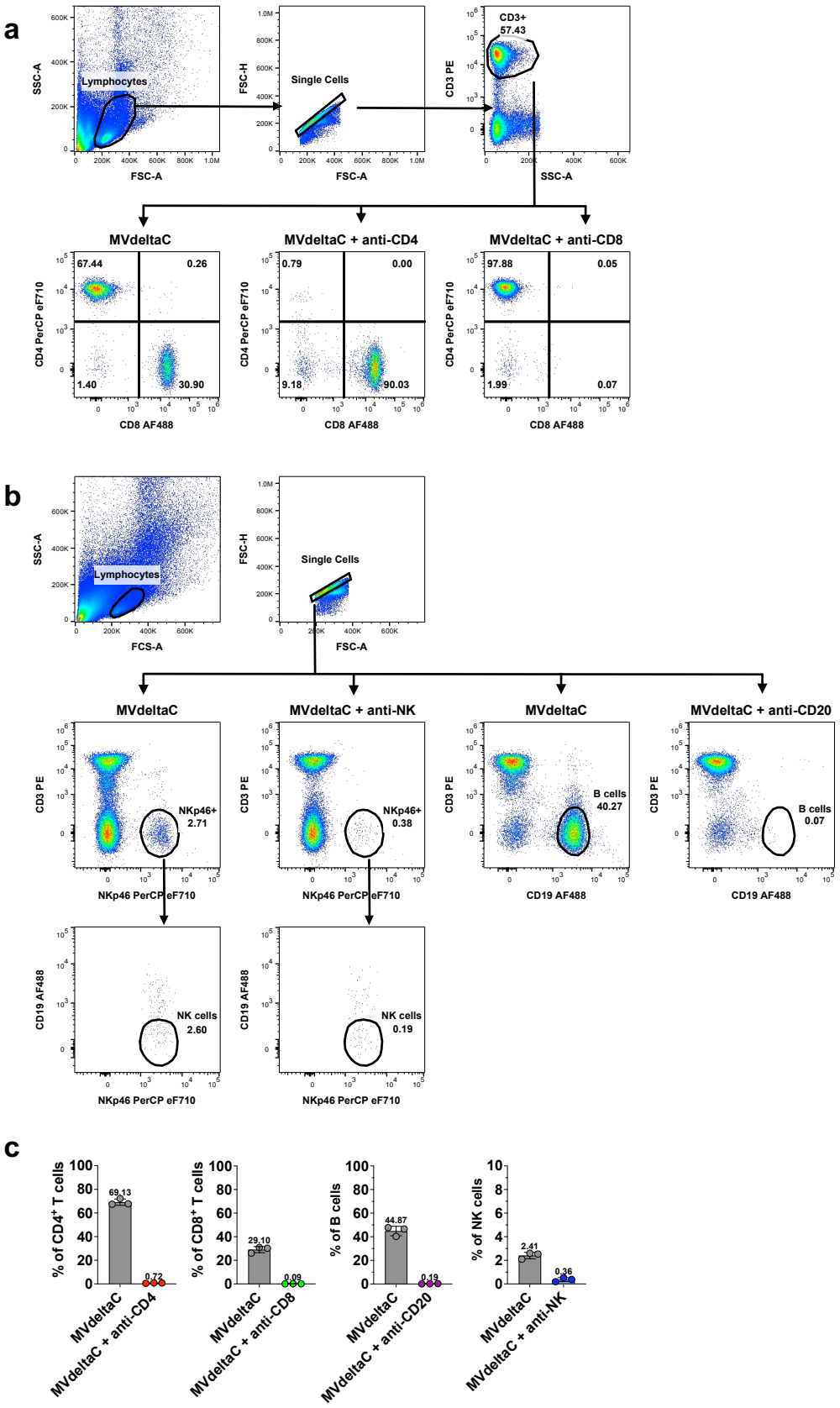

Figure S6. Flow cytometry analysis of immune cell populations in the blood of A/J mice depleted for CD4$^+$, CD8$^+$, B or NK cells. (a) Representative dot plots show the flow cytometry gating strategy to identify CD4$^+$ (CD3$^+$ CD4$^+$ CD8$^-$), CD8$^+$ (CD3$^+$ CD8$^+$ CD4$^-$) or (b) NK (CD3$^-$ NKp46$^+$ CD19$^-$) and B (CD3$^-$ CD19$^+$) cell populations in the blood of treated mice. Mice were grafted with 5x10^6 NS20Y murine tumor cells on day 0. T cell depletion was achieved by i.p. injection of anti-CD4 or anti-CD8 mAbs (200 µg in 100 µL of PBS) on days 5, 6 and 7 after NS20Y cells injection. NK or B cell depletion was performed on days 5 and 7 using 50µg of anti-asialo GM1 or 200µg of anti-CD20 antibodies, respectively. Sustained immune cell depletion was achieved by weekly antibody administrations on days 14 and 21. Tumor therapy with MVdeltaC at 2x10^{6}TCID$_{50}$ was performed on days 6, 9 and 12. Immune cell populations in the groups of A/J mice were analyzed on day 27. (c) Bar graphs show flow cytometry data for the three animals from each group, means ± SD.

FIGURE S7

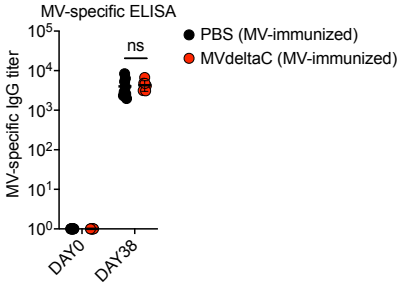

Figure S7. MV-specific IgG antibody responses in A/J mice following MV Schwarz vaccination. Mice were immunized i.p. with MV Schwarz (1×10^5 $TCID_{50}$) on day 0. Sera were collected at day 38 post-immunization and assessed for IgG antibody responses to MV antigens by ELISA. The data show the reciprocal endpoint dilution titers of MV-specific IgG antibodies in preimmune (day 0) and day 38 sera; each point represents an individual mouse; means ± SD, n= 7-9 per group; unpaired two-tailed t test; ns, not significant.

FIGURE S8

a

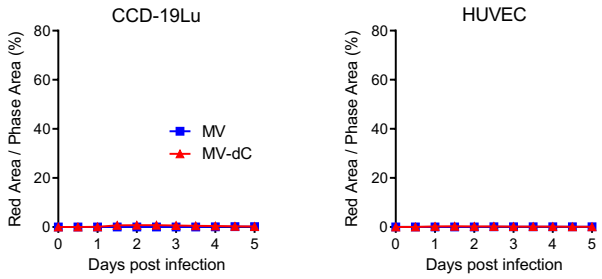

b

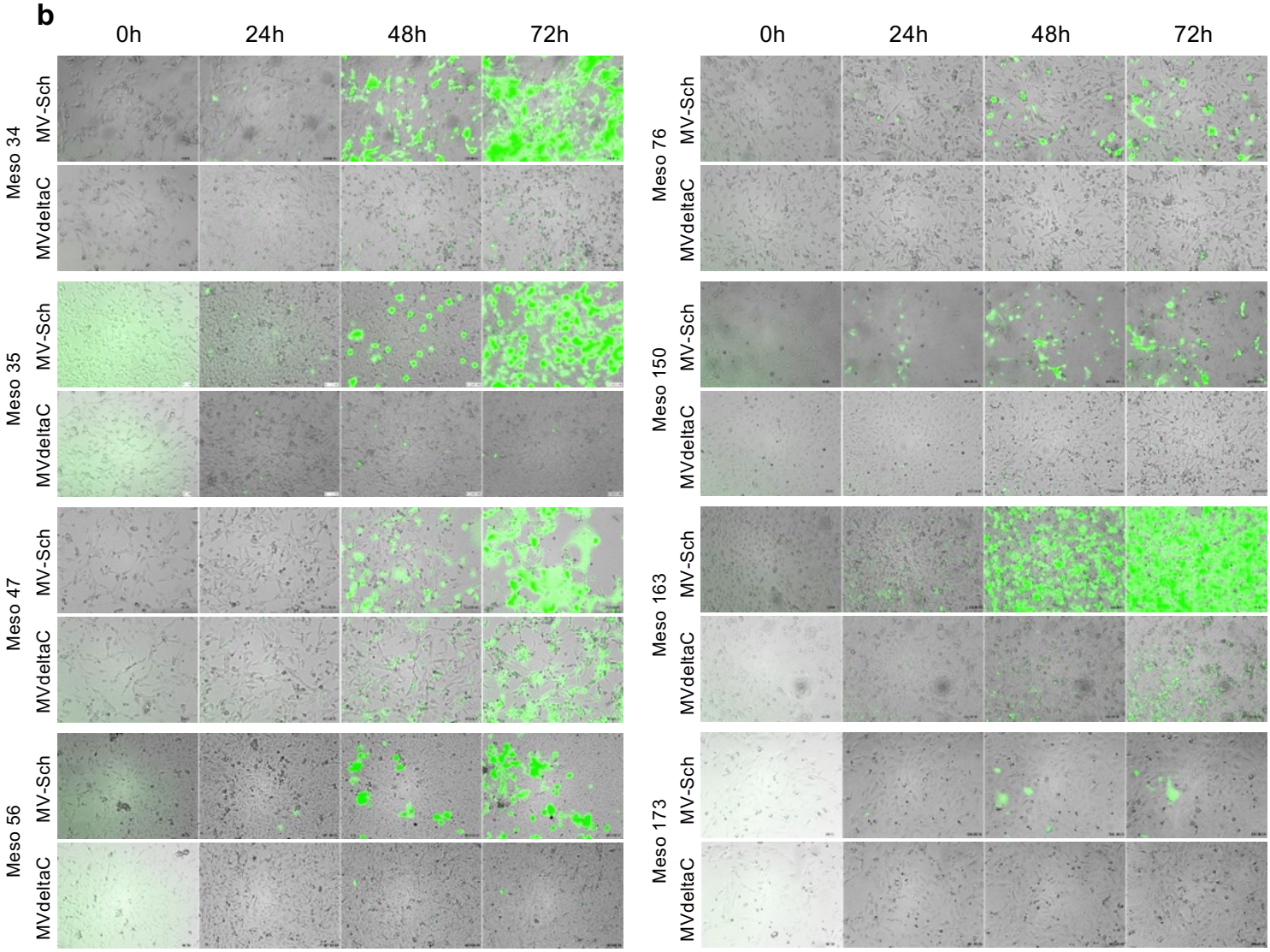

Figure S8. Infection of healthy and cancer human cells by MV or MVdeltaC. (a) Quantification of virus propagation in healthy lung fibroblasts (CCD19-Lu) or endothelial cells (HUVECs) infected with either MV-mCherry or MVdeltaC-mCherry. (b) Time-lapse microscopy analysis of mesothelioma cell lines infected with MV-eGFP or MVdeltaC-eGFP (MOI = 1).

FIGURE S9

VIDEOS MESO13

Figure S9. Infection of Meso 13 mesothelioma cells by MV or MVdeltaC.
Time-lapse microscopy analysis of mesothelioma cell lines infected with MV-eGFP (a) or MVdeltaC-eGFP (b) (MOI = 1).

FIGURE S10

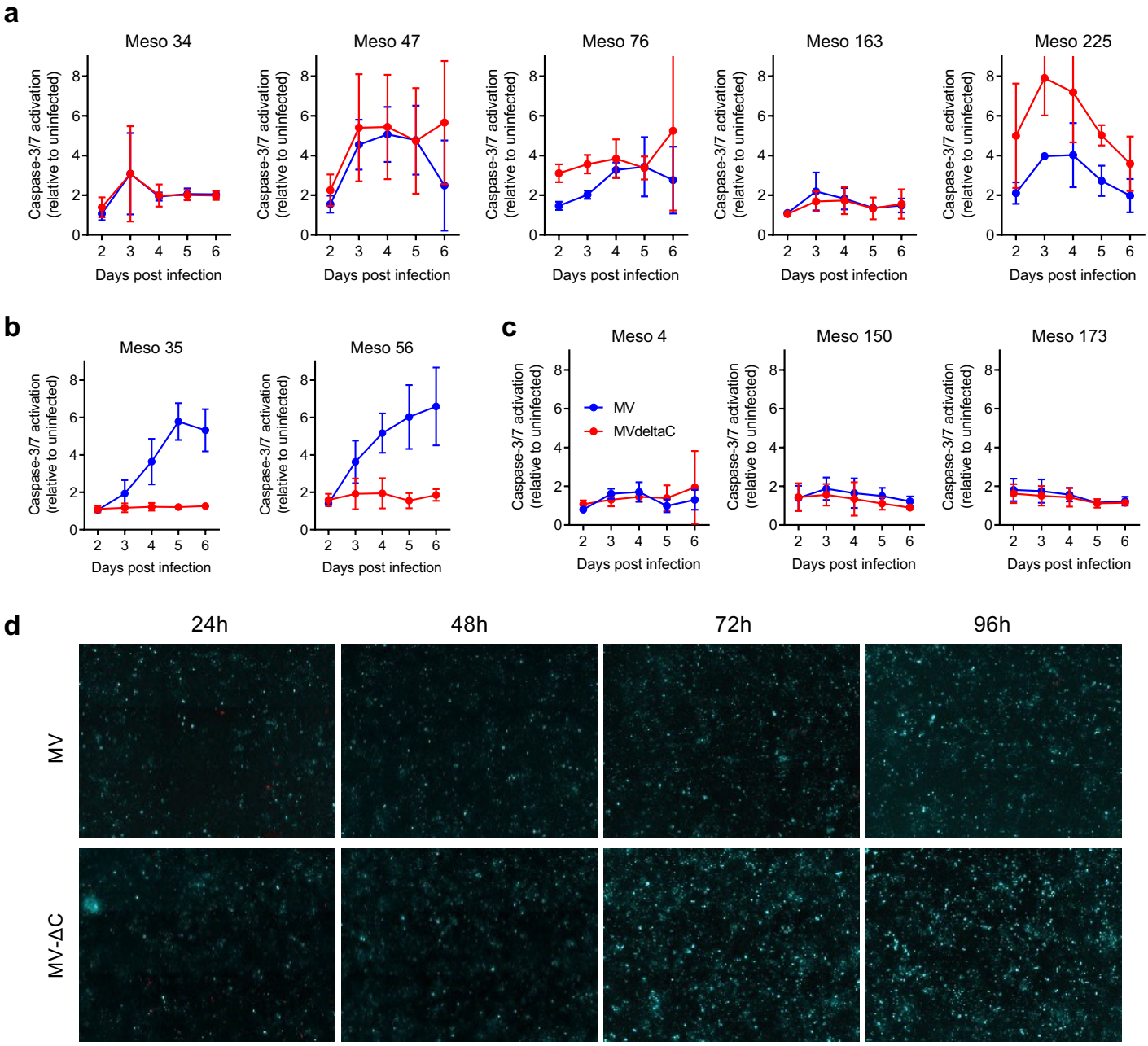

Figure S10. Activation of Caspases-3/7 in mesothelioma cells infected by MVdeltaC. (a-c) Luminescence-based quantification of caspase-3/7 activity in human mesothelioma cell lines. (a) MV-permissive, (b) MVdeltaC-resistant, and (c) MV-resistant cells. (d) Fluorescence microscopy of Meso 4 cells showing caspase-3/7 activation (cyan) after infection with MV-mCherry or MVdeltaC-mCherry (red).

FIGURE S11

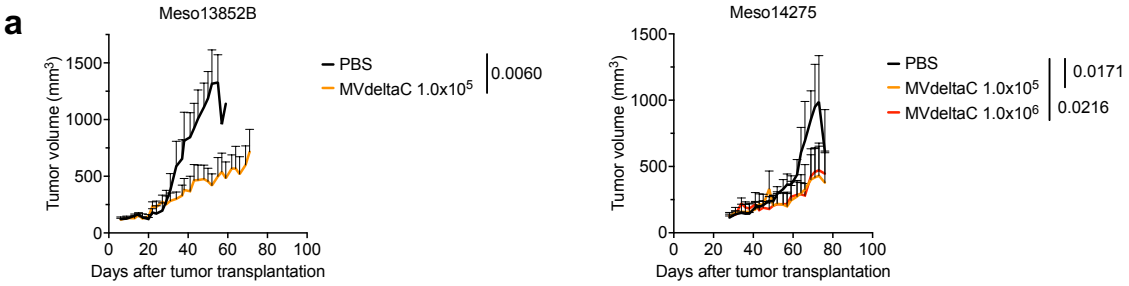

Figure S11. MVdeltaC inhibits human PDX growth in immunodeficient mice. Growth of mesothelioma PDX tumors in NMRI nu/nu mice after weekly MVdeltaC therapy at two doses; means ± SEM, n = 3 mice per group; each group was compared to PBS group (unpaired one-tailed t test).

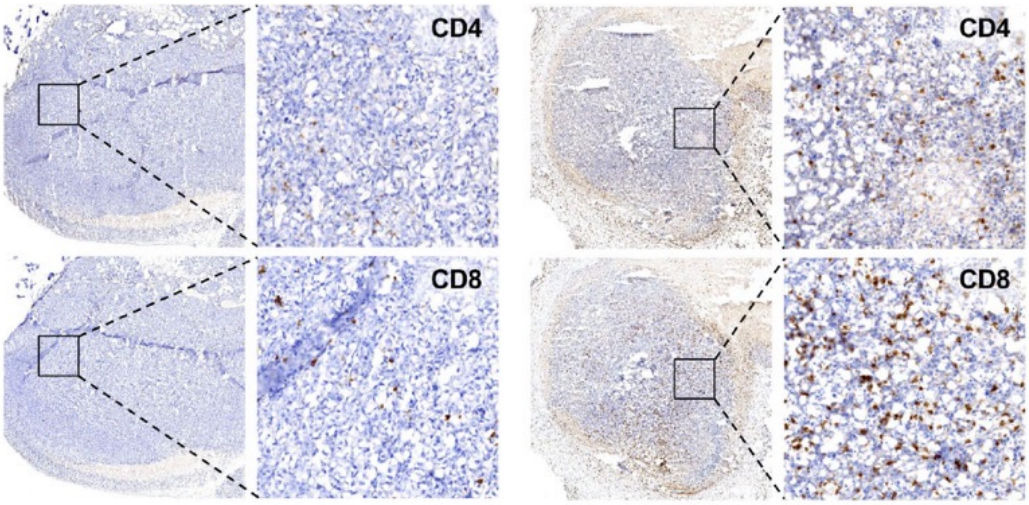

PBS

Cold Tumor

- Exclusion of CD8+ T cells and NK cells from the tumor
- Immunosuppressive immune cells in tumor (ie. Tregs)
- Poor prognosis and response to immunotherapy

MVdeltaC

Hot Tumor
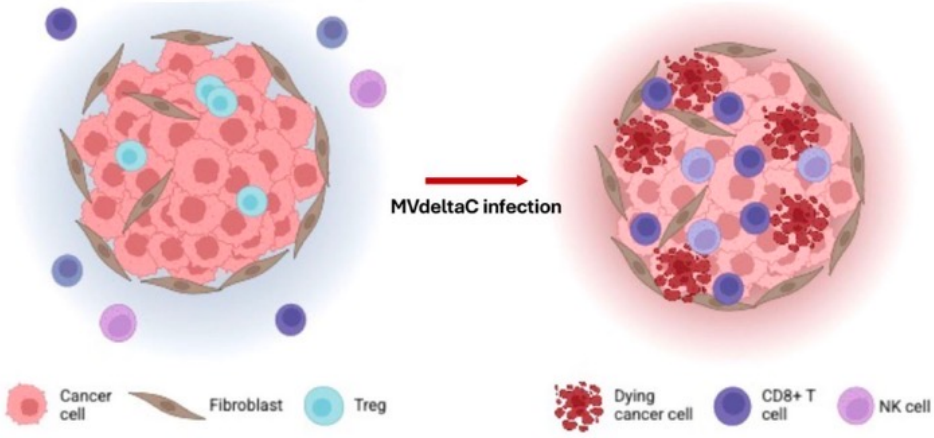
- CD8+ T cells and NK cells are present in tumor
- Suppression of immunosuppressive cell types
- Improved prognosis